Functional Bismuth- and Molybdenum-based Nanomaterials and their Humidity and Gas Sensing Properties

Dissertation

zur Erlangung der naturwissenschaftlichen Doktorwürde

(Dr. sc. nat.)

vorgelegt der Mathematisch-naturwissenschaftlichen Fakultät

der Universität Zürich

von

Min Sheng

aus V.R. China

Promotionskomitee

Prof. Dr. Greta R. Patzke

Prof. Dr. Roland K. O. Sigel

Prof. Dr. Eva Freisinger

Zürich, 2013

Table of contents

2. Room temperature synthesis and humidity sensing properties of $Bi_2O_2CO_3$ nanosheets……………….………………………………..……………...…55

3. Humidity sensing materials: Structure-activity relations among bismuth phosphates…………………………………………….………………………...…67

Acknowledgement

In the last three and a half years, I have received so much support and help from people whom I want to thank with these acknowledgements which are probably too brief to express my full gratitude.

First of all, I would like to thank Prof. Dr. Greta R. Patzke for providing me the unique opportunity to work on this interesting project. Her trust, patience and support, along with the openness for innovation and creation, inspired me to develop my ideas and imagination. I am also grateful for the skills and knowledge I have learned from her supervision as well as from the workshops supported by her.

I thank Prof. Dr. Roland K. O. Sigel and Prof. Dr. Eva Freisinger for being co-referees of this thesis.

I appreciate the friendly working atmosphere and fruitful relaxed discussions with my group members: Dr. Pierre-Emmanuel Car, Dr. René Moré, Dr. Yang Zhen, Roman Kontic, Georg Geisberger, Lubin Ni, Hongfei Liu, Fabio Evangelisti, Kim von Allmen, Roger Jacot and all our master students. Special thanks go to our former group member, Prof. Dr. Ying Zhou, for his kind support in cleanroom FIRST (Frontiers In Research: Space & Time, ETH Zurich) and for many fruitful discussions. I am especially grateful to Dr. Jorge Cors (PHASIS GmbH, University of Geneva) for his generous support with sensor construction expertise.

I am indebted to Prof. Dr. Guorong Chen and Prof. Dr. Xiaoliang Mo (Department of Materials Science, Fudan University Shanghai), including their former group members Dr. Kaibo Zheng (Department of Chemical Physics, Lund University) and Leilei Gu (Department of Electronic & Computer Engineering, Hong Kong University of Science and Technology) for the harmonious collaboration and for sharing their knowledge of sensing experiments.

I thank Dr. André Käch (Center for Microscopy and Image Analysis, University of Zurich) for his kind introduction to the electron microscopy facilities, and Dr. Frank Krumeich (Laboratory of Inorganic Chemistry, ETH Zurich) for TEM investigations and valuable information and Dr. Jörg Patscheider for XPS measurements and helpful discussions.

I would like to express my gratitude to Hanspeter Stalder for his technical support and valuable suggestions for the laboratory setups. Also I want to thank Dr. Ferdinand Wild, Heinz Spring and Manfred Jöhri for the professional knowledge concerning software

problems, devices, elemental analyses and hardware. I am grateful to Susanna Sprokkereef, Nathalie Fichter, Dr. Jae Kyoung Pak, Beatrice Spichtig, Dr. Sabine Stockhause and Ramona Erni for their administrative tasks.

Also I thank my dear friends Heiner, Martje, Zhenya, Jing, Cathleen, Franziska, Maria, Louis, Xun and many other old friends in China for being there with me and never leaving me alone by all means.

Last but not at least I would like to express my greatest gratitude to my mother and father, who live far away in Shanghai and have always been supporting my decisions since I started living in Europe. Their love and encouragement are my driving force and inspiration, which make me happy and confident in every sense. So does my husband, Fabio, whose love, understanding and support allow me to finish this challenge and to live the way I like to.

This work was supported by the Swiss National Science Foundation (SNSF Professorship PP00P2_133483/1), by the NCCR MaNEP (Materials with Novel Electronic Properties), by the University of Zurich, by the CMSZH (Graduate School of Chemical and Molecular Science Zurich) and by the Sino Swiss Science and Technology Cooperation (SSSTC, EG16-032010), which are gratefully acknowledged.

Abbreviations

AC	alternating current
AMT	ammonium metatungstate
BET	Brunauer-Emmett-Teller
C	capacitance
CB	conduction band
CNTs	carbon nanotubes
CVD	chemical vapor deposition
d	day(s)
EA	elemental analysis
EDXS	energy dispersive X-ray spectroscopy
EN	electronegativity
EPR	electron paramagnetic resonance
FIRST	Frontiers In Research: Space & Time, ETHZ (cleanroom)
HRTEM	high resolution transmission electron microscopy
LCR	Inductance (L), Capacitance (C), and Resistance (R)
h	hour(s)
HRTEM	high resolution transmission electron microscopy
HTB	hexagonal tungsten bronze
IDE	interdigital electrode
IR	image reversal
IR	infrared
LPG	liquefied petroleum gas
min	minute(s)
MW-HT	microwave-assisted hydrothermal synthesis
ppm	parts per million
QD	quantum dots
R	resistance
RH	relative humidity
RT	room temperature
SAED	selected area electron diffraction
sccm	standard cubic centimeters per minute

SEM	scanning electron microscopy
TEM	transmission electron microscopy
TMOs	transition metal oxides
UV	ultraviolet
V	volt
XPS	X-ray photoelectron spectroscopy
XRD	X-ray diffraction
WCA	water contact angle
1D	one dimensional
2D	two dimensional
3D	three dimensional

Publications

The following parts of this PhD thesis have been published:

Chapter 3

Min Sheng, Leilei Gu, Roman Kontic, Ying Zhou, Kaibo Zheng, Guorong Chen, Xiaoliang Mo and Greta R. Patzke, *"Humidity sensing properties of bismuth phosphates"*, *Sens. Actuators B* **2012**, 166, 642-649.

List of Tables

List of Figures

1. Introduction

1.1 Environmental challenges

Over the past years, public awareness of the adverse health effects of air pollution has been raised. In particular, hazardous gases in developing countries, which result mainly from industrial activities, burning fossil fuels and domestic heating, need to be controlled urgently to keep them below the designated levels. Therefore, developing simple, low cost and reliable air pollution monitoring devices is a current challenge for human health and sustainable industrial development policy. A great number of commercial gas sensors are available on the market. However, they still cannot entirely fulfill many key operational criteria. Hence, nanostructured semiconducting transition metal oxides (TMOs) might be the solution for this issue. Oxide nanomaterials have various promising applications in solar cells,[1-4] photocatalysts, [5-7] fuel cells,[8,9] humidity/gas sensors[10-13] and in other technological areas.[14-17] Since the first discovery of the change in electrical properties of ZnO thin films towards liquefied petroleum gas (LPG) by *Seiyama* in 1962,[18] the need and demand for semiconducting gas sensors has increased dramatically. A commercial boom for sensor fabrication has started in Japan in the 1970s during which gas and humidity sensors were fabricated in large-scale production for household and daily life uses.[19] Due to their unique surface properties,[20-23] which lead to interaction with the detecting gas molecules and the changes of the electrical conductivity,[24-26] semiconducting oxides have become more and more preferred for sensor applications. Semiconducting sensors are used for a large variety of environments, including the detection of hazardous gases in factory plants or mining facilities, oxygen control in combustion processes or humidity and air quality monitoring in the automobile industry.[19,27] Nowadays, not only sensor fabrication techniques are required to be economic, sustainable, efficient and reproducible, but the integration of sensor constituents into portable devices needs to be considered as well. This renders nanostructured oxide materials highly promising candidates to meet the above-mentioned requirements.

However, the complexity of sensing mechanisms requires a strategic choice of sensing materials according to their physical and chemical characteristics and the chemical targets. The surface properties of oxide materials are strongly influenced by a wide variety of parameters including chemical composition, structure, morphology, grain size, surface-area-to-volume ratio etc. There is a wide range of physical and chemical processing routes for synthesizing semiconducting oxides, including thermal evaporation methods,[28,29] sol-gel template methods,[30-32] solution-phase processes,[33-35] chemical vapor deposition,[36-38] hydrothermal methods, [39-41] etc. A wide variety of shapes and morphologies, such as nanowires,[42,43] nanotubes,[44,45] nanofibers,[46] nanobelts,[47,48] nanorods,[49,50] and nanosheets[51,52] can be accessed by tuning the synthetic conditions and types of starting materials.

Among numerous semiconducting sensors based on TMOs, ZnO and SnO_2 are the most advantageous constituents. These oxides are not only promising commercial sensing materials for sensor fabrication, but also attractive for materials scientists due to the convenient synthesis routes, various morphologies and high sensitivity.[53,54] However, after half a century their application limits have been stretched and the lack of selectivity still remains a problem.[55,56] Due to this fact, new oxide nanomaterials need to be investigated to widen this bottleneck in sensor development. This leaves space for exploring other approachable sensing materials, such as modified binary oxides and ternary oxides.

All in all, exploration of new sensing oxide nanomaterials opens up innovative technical perspectives. In addition, new oxide systems might promote better understanding of the complicated sensing mechanisms and the dependence of sensing performance on the materials properties.

1.2 Processing of inorganic hydrothermal routes

The term "hydrothermal" was first used by *Sir Roderick Murchison* (1792 – 1871), a British geologist, to describe the geological action of water at elevated temperature and pressure.[57] Generally, hydrothermal synthesis is defined as any heterogeneous reaction in the presence of water or other aqueous solvents leading to crystal growth under high temperature and pressure.[58] The critical point of water, for example, is at 374 °C and 218 atm. Above this temperature and pressure, water becomes supercritical, which means that the fluid exhibits characteristics of both a liquid and a gas with high viscosities and increased dissolving capacity for chemical compounds.[59] Supercritical fluids can dissolve and recrystallize substances, which are insoluble under standard conditions.

Due to its convenient and environmentally-friendly operation, the hydrothermal technique is considered as a forefront technology and one of the most important tools for advanced nanomaterials applied in widespread fields, such as electronic devices, catalysis, magnetic data storage, biomedicine, etc.[60] Hydrothermal processing provides not only possibilities to synthesize an almost endless variety of compositions, but gives also access to nanoparticles, fibers and thin films.[61-63] In addition, it offers opportunities to tune reaction parameters, such as temperature, additives, solvents and pH value. Furthermore, this wet chemical processing with mild reaction conditions offers access to metastable phases and nanoscale morphologies that are hardly obtained under ordinary conditions or via classic synthetic methods at high temperatures.[64,65] The approach is very well suitable for the fabrication of compounds exhibiting highly anisotropic structural features.[66]

Pressure and temperature conditions for different preparation techniques of advanced materials are illustrated in Figure 1.1. Among all the described techniques, hydrothermal processing is considered as simple, economic and environmentally benign due to its ambient conditions.[67] In addition to above mentioned advantages, hydrothermal techniques offer special conditions due to their highly controlled diffusivity in closed solvent media systems.[57]

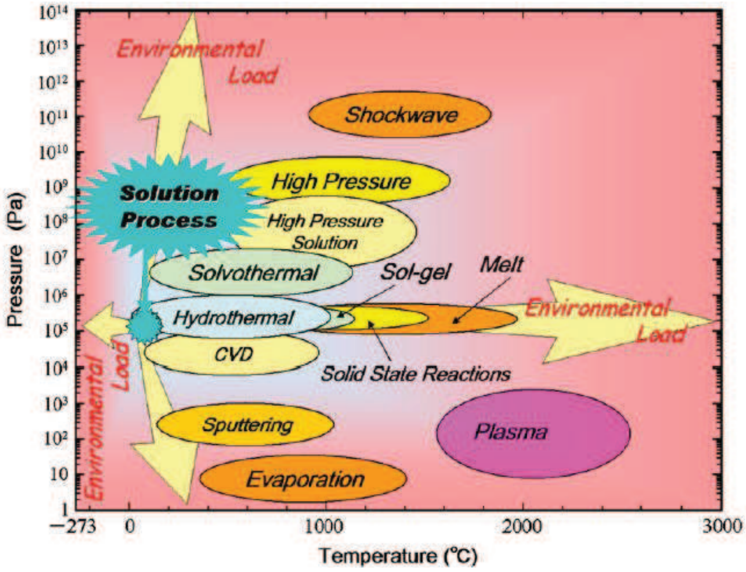

Figure 1.1. Schematic pressure-temperature map of materials processing techniques for advanced materials.[67]

Nowadays, hydrothermal techniques are not limited to crystal growth, but they have become a highly interdisciplinary subject which is used and investigated in other research branches (cf. Figure 1.2).

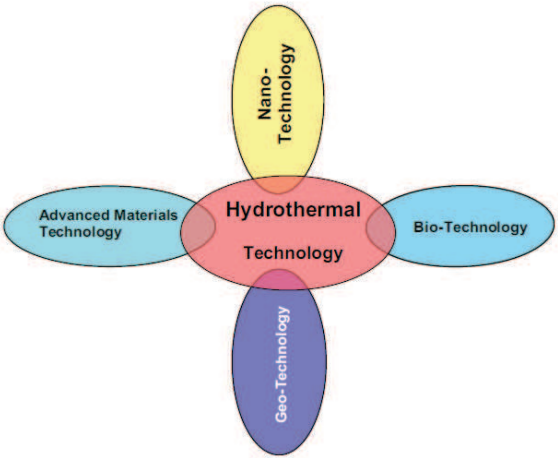

Figure 1.2. Hydrothermal technology in the 21st century. [57]

Generally, hydrothermal processing of oxide nanomaterials is a promising simple, one-pot and surfactant-free approach. Self-assembly can be achieved if the constituents have appropriate interaction energies and are directed towards each other by Coulomb, van der

Waals, and polymeric interactions.[67] This approach enables arrangement of ordered arrays of nanoparticles in structures.[68,69]

1.2.1 Conventional hydrothermal approaches

The work of *Spezia* in 1900 granted hydrothermal technology an important role in the growth of bulk crystals.[70] Since then, hydrothermal processing has been widely used as a versatile "soft chemistry" approach for inorganic material synthesis, crystal growth (bulk crystals and single crystals), phase equilibrium studies, reduction, structure stabilization, metaphase studies and so on. Especially in the last decade, over 10.000 scientific papers on nanomaterials using this technique have been published which reflects the major benefits for many aspects of nanotechnology research.[57]

Historically, hydrothermal synthesis was primarily optimized for large crystals, such as of quartz.[71] Most laboratory hydrothermal experiments are performed in multi-purpose autoclaves with Teflon inlays (Figure 1.3). In most cases, reaction pressure can be either calculated using system-related PVT diagrams for water proposed by *Kennedy*[72] or directly measured by an installed Bourdon gauge.

Figure 1.3. Autoclave and Teflon liner used for standard hydrothermal treatments.[73]

Over the past years, a broad range of nanoscale metals and metal oxides have been obtained under mild hydrothermal conditions, and their electronic, optical thermal, catalytic and sensing properties have attracted considerable attention for further applications.[74-79] In particular, a considerable number of research works on design and preparation of advanced functional metal oxides, such as TiO_2,[80-82] ZnO,[83,84] CeO_2,[85] α-Fe_2O_3,[86,87] Co_3O_4,[88] ZrO_2,[89] In_2O_3[90] etc., are of great interest in nanotechnology.

Besides the large family of hydrothermally synthesized TMOs, many other nanoparticle types have been reported as well. CdS,[91,92] PbS[93] and ZnS[94] nanoparticles have been hydrothermally processed in various reaction media and surfactants. Furthermore, carbon nanotubes (CNTs) can be prepared and obtained by this technique as an alternative to CVD methods. Hydrothermal CNT synthesis proceedings have been investigated in detail by several research groups.[95-97] Moreover, different composites and coating of various compounds on TMOs or metals can be achieved using hydrothermal methods. For example, $HNbWO_6$/Mo nanocomposites,[98] as well as a nanocomposite containing activated carbon and titania (AC:TiO_2),[99] have been synthesized under hydrothermal conditions, and both materials show promising potential as photocatalysts.

However, despite the convenience of hydrothermal approaches some drawbacks of this technique still need to be improved or be taken into account when planning a process. Often, the rather long reaction times, typically few hours or even days,[57] are not sufficiently efficient, especially for large-scale industrial production. This leads to the ongoing developments of classic hydrothermal process towards faster processing. The combination of different techniques, such as microwave-hydrothermal (cf. following section), electrochemical-hydrothermal and mechanochemical-hydrothermal, can reduce the reaction times at least 2 – 3 orders of magnitude, thus rendering chemical processes more economic and efficient. These so called “multi-energy processing” techniques give hydrothermal process a new direction with enormous potential. In addition, it helps us to better analyze and understand the “black box” character of hydrothermal systems. Further details are given in the following sections.

Studies on morphology control of nanoscale metal oxides have been ongoing for years. Control over desired morphologies with systematic strategies still remains a challenging issue. For example, various morphologies of commercially interesting ZnO nanostructures which are also interesting sensor materials have been brought forward including nanowires,[100] nanorods,[101,102] nanosheets,[103] nanobelts,[104] nanorings,[105,106] tetrapod nanowires,[84,102,107] and nanobows.[106] *Zhang*[108] et al. reported on a variety of morphological shapes, such as disk-like, flower-like and dumbbell-shaped ZnO, which were obtained via a capping template-assisted hydrothermal process. Generally, a wide variety of reaction parameters, such as temperature range, solvent, pH value, types of additives and Zn source, can direct the morphological characteristics of the ZnO final products. From this point of view, morphology-controlled synthesis approach still remains a complex task in nanomaterial processing.

All in all, hydrothermal techniques belong to the most promising routes for synthesizing functional nanomaterials. In the following, microwave-assisted hydrothermal techniques and some advanced synthesis strategies are introduced.

1.2.2 Microwave-assisted hydrothermal syntheses

Recently, microwave-assisted hydrothermal synthesis (MW-HT) has emerged as a popular synthetic technique due to its rapidity, convenience, low cost and environmental friendliness.[109,110] Compared to conventional hydrothermal treatment, which takes hours or even days to complete reactions, this time- and energy-saving method provides the possibility to synthesize novel or metastable phases by speeding up crystallization kinetics to few minutes or less.[111] Furthermore, the homogenous temperature profile throughout the sample facilitates quick reaction rates and the formation of uniform nucleation centers.[112]

Many nanoscale binary and ternary oxide semiconductors have been synthesized via microwave-assisted hydrothermal routes. This technique opens up a convenient and novel pathway for new morphologies of nanoscale target materials, which are difficult to obtain through conventional hydrothermal treatment.

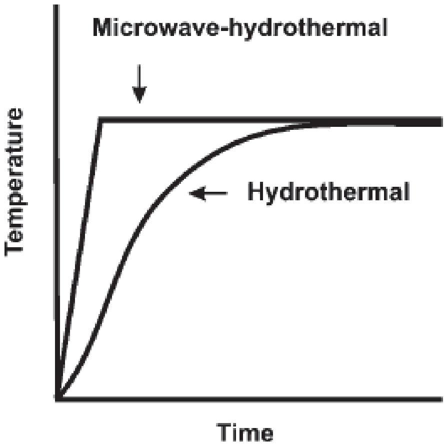

Figure 1.4. Comparison of heating processes of conventional and microwave-assisted hydrothermal processes.[64]

Table 1.1. Selected metal oxide semiconductors synthesized via microwave-assisted hydrothermal techniques (morphologies and applications).

Oxide	Morphology	Application	Ref.
CuO	Nanorods	EtOH sensor	[113]
CuO	Nanosheets	EtOH sensor	[114]
Fe_3O_4	Nanoroses	EtOH sensor	[115]
α-Fe_2O_3	Nanorings	EtOH sensor	[116]
α-Fe_2O_3	Rod-like nanostructure	Humidity sensor	[117]
Co_3O_4	Nanocubes	Xylene and EtOH sensor	[118]
WO_3	Nanorods	EtOH sensor	[119]
ZnO	Nanoflakes	NO_2 sensor	[120]
ZnO	Star-like nanostructure	Ammonia sensor	[121]
ZnO	Nanorods	EtOH sensor	[122]
ZnO	Nanorods, nanoflowers	CO, CH_4 and EtOH sensor	[123]

Although microwave-assisted techniques offer the above-mentioned advantages, their reaction pathways and mechanisms still remain widely unknown. Previous studies pointed out that, a fair number of reaction parameters, such as starting materials, concentrations, solvents, time, temperature and microwave power, can strongly influence the morphology and formation of oxides in hierarchical nanostructures.[124] Several scientists proposed hypotheses for reaction processes based on indirect observations.[116,125-127] However, all such indirect studies do not deliver enough evidence of the chemical reactions and mechanisms. Therefore, direct methods, such as *in situ* investigations, are highly required to establish a fundamental concept, which remains a challenging task.

1.2.3 Synthetic strategies

1.2.3.1 Template- and additive-directed syntheses

Templating is one of the most important strategies to control a wide range of size and shape parameters in nanoscale materials.[128] By using the framework structures of nanoporous organic or inorganic hosts, such as channels (1D),[129-131] layers (2D)[108,132] and cavities (3D),[133] the size and shape of materials can be controlled. Morphology control can especially be achieved through the interaction or incorporation of additive ions.[64,134] This strategy has, for example, been applied on W/Mo-oxides of the hexagonal structure type which is relevant for the present thesis (cf. Chapter 5),[135-138] and a series of studies showed that different shapes can be easily obtained by selecting morphology-directing alkali cations. Preceding studies on the synthesis of W/Mo-oxides of the hexagonal tungsten bronze (HTB) type with alkali chloride additives demonstrated that the alkali cations are incorporated into the wide hexagonal channels of the oxide framework structure. Furthermore, they exert a strong influence on the resulting morphologies of the nanostructured products. Starting from ammonium metatungstate (AMT) and $MoO_3{\cdot}2H_2O$, the addition of LiCl and NaCl leads to a nanorod morphology while KCl, RCl and CsCl favor a hierarchical arrangement of smaller nanorods into microspheres.[137] The thermal stability of Rb-W/Mo-HTB is much higher than that of the Li^+, Na^+ and K^+ containing analogues due to the stronger stabilizing effect of Rb^+ cations. Heat treatment at 500 °C provides further overview of the involved phase transformations.[137] Interestingly, Rb-containing W/Mo-HTB remains structurally stable while the structures of alkali-free W/Mo-HTB as well as of Li-, Na- and K-containing compounds collapse and undergo quantitative or partial transformation into a monoclinic phase. This opens up new research perspectives for the multiple roles of alkali additives as structure-directing agents and structure stabilizers.

Table 1.2. Selected examples for inorganic additive-directed hydrothermal syntheses of binary and ternary oxide nanomaterials with catalytic or sensor applications.

Oxide	Solvent/additive	Morphology	Ref.
MoO_3	Water and ionic additives	Nanorods	[129]
MoO_3	KNO_3, $Ca(NO_3)_2$, $La(NO_3)_3$	Different morphologies of MoO_3	[139]
MoO_3	Water, H_2O_2	Nanofibers (< 100 nm diameter)	[140]
MoO_3	HNO_3, $LiNO_3$	Hierarchical microspheres	[141]
SnO, SnO_2	Water (HCl/NaOH)	Nanoparticles, nanoplatelets	[142]
SnO_2	Water, $NaHCO_3$	Nanoparticles (10 – 40 nm)	[143]
W/Mo oxides	Water, inorganic Additives (alkali chlorides)	Spherical arrangements	[137]
$W_{18}O_{49}$	Na_2SO_4	Nanorods	[144]
M_xWO_3 (M = Li – Cs)	Lis_2SO_4, K_2SO_4, LiCl, NaCl KCl, RbCl, CsCl	Alkali-dependent hexagonal tungsten bronzes with different morphologies	[135]
$BiVO_4$	K_2SO_4	Nanofibers, nanospheres	[145]

1.2.3.2 Solvothermal processes

The solvothermal approach is an analogue procedure to obtain inorganic TMO nanoparticles[146] and metal nanoparticles.[147] Similar to hydrothermal treatment, it is a solution-based synthesis technique proceeding in sealed vessel systems at elevated high temperatures. Instead of water used in hydrothermal routes, organic solvents, such as trioctylamine,[148] toluene,[149] pyridine,[150] ethylenediamine[151-153] are used as liquid media for nanoparticle synthesis. Metal powders are easily oxidized to the corresponding oxides under solvothermal conditions. CeO_2 nanoparticles in the 2 nm size range have been reported by reaction of metal with 2-methoxy ethanol.[154] Some organic compounds act not only as solvent, but also as capping agent.[155] Bismuth-based materials which are also in the focus of the present thesis provide further examples: Formation of micro-scale and nanostructured sillenite $Bi_{12}TiO_{20}$ has been reported by solvothermal reactions in the presence of NaOH/KOH solution and polyethylene glycol.[156 - 158] Bi_2O_3 nanotube arrays were obtained via a solvothermal method through the reduction of bismuth oxide by ethylene glycol.[159] *Michailovski* and *Patzke* studied the formation and morphology of MoO_3 nanorods/nanofibers (cf. also Chapter 5) in acidic media by varying the concentration of alkali halide additives.[160] The multiple roles of solvent media offer a meaningful approach for tuning the properties of materials.

However, the toxicity and high costs of these solvents limit the use of solvothermal process. Solvent recycling or purification remains another challenge in terms of technical and economic aspects.

1.3 Functional oxide materials for current applications

1.3.1 Gas sensing applications

Since *Seiyama* first discovered ZnO as a new type of gas detector working via changes of electrical properties in 1962, and Taguchi established the mass production of TMO-based sensors (*Figaro Engineering Inc.*), the development of gas sensors based on TMOs has been much enhanced. Several theories for the underlying sensing mechanisms have been proposed.[161-163] Tin oxide (SnO_2) is one of the most widely investigated TMOs with multiple functions in sensing and catalysis. SnO_2 was also one of the first commercial chemical gas sensors on the market.[164] The theoretical and experimental investigation of SnO_2 sensing properties established the basic model of general TMO based sensors. A series of model studies and reviews have been dedicated to its gas sensing and surface properties.[165-174] On SnO_2, as well as on other n-type semiconducting sensors, adsorption of surface oxygen causes the changes in their conductivity and work function. This procedure takes place only at high operating temperatures (typically between 100 – 500 °C), i.e. below the diffusion temperature range of bulk ionic species.[175]

However, much efforts have been made to understand the adsorption and desorption mechanisms of gases, which result the remarkable resistance changes in TMO-based sensors. A "ionosorption model", which was based on "boundary layer theory of chemisorption", was established in the 1950s by *Hauffe*.[176,177] He pointed out that electrons can be transferred to the chemisorbed oxygen atoms due to their electron affinity. Thus, chemisorbed oxygen atoms will be turned into surface ions. *Hauffe* and *Morrison* developed this model in the 1970s to clarify the gas adsorption mechanisms on semiconducting materials.[178]

1.3.1.1 Working principles and experimental setup of sensing semiconductors

For sensing measurements, the sensor is usually deployed on a heated substrate connected with two metallic electrodes, preferably gold wires. The thermal treatment plays a very important role in generating oxygen species, which are required for target gas detection. The amount of adsorbed oxygen species increases notably after thermal treatment. The target gas, such as CO molecules, interacts with the semiconductor surface to change the density of charge carriers. As a consequence, the conductivity either increases for an n-type sensor or decreases for a p-type sensor. During the heating process, atmospheric oxygen molecules are adsorbed on the surface as $O^{-}_{2,ads}$, O^{-}_{ads} and O^{2-}_{ads} species which trap electrons from the conduction band (CB) of semiconductor.[179] The processes of oxygen adsorption, dissociation and charge transfer can be described as follows:[180,181]

physisorption $O_{2,gas} \leftrightarrow O_{2,ads}$

ionosorption $O_{2,ads} + e^{-}(CB) \leftrightarrow O^{-}_{2,ads}$

$O^{-}_{2,ads} + e^{-}(CB) \leftrightarrow 2O^{-}_{ads}$

$O^{-}_{ads} + e^{-}(CB) \leftrightarrow O^{2-}_{ads}$

$O^{2-}_{ads} \leftrightarrow O^{2-}$ (1^{st} bulk layer)

When reducing target gases, such as H_2, CO or NH_3, react with the oxygen ions, the electrons will be released and return to the CB. Other neutral oxygen species, such as $O_{2,phys}$ and lattice oxygen ions O^{2-}_{lat} are assumed not to interfere in the interaction of target gases with sensors.[175]

Serrini et al. studied the influence of thermal treatment on the change of adsorbed oxygen of SnO_2 and the sensing quality.[182] Based on comparisons of O 1s XPS spectra as shown in Figure 1.5 a before and after thermal treatment (at 375 °C), an increase of the amount of oxygen can be observed which indicates a newly generated thin layer of adsorbed oxygen species. The states of present oxygen species were analyzed by using three simulation peaks (Gaussian / Lorentzian mixed) at 530.6 eV, 531.7 eV, and 532.7 eV, which are illustrated in Figure 1.5 b. These three fitted peaks correspond to SnO_2 lattice oxygen (peak 1), chemisorbed hydroxyl (OH^{-}_{ads}) or/and physisorbed water molecule (H_2O_{phys}) (peak 2), and chemisorbed oxygen species ($O^{-}_{2,ads}$ and O^{-}_{ads}) or/and physisorbed oxygen species ($O_{2,phys}$) (peak 3), respectively.[183] Peak 2 and 3, which indicate the physisorption and chemisorption of oxygen, display a clear intensity increase after thermal treatment.

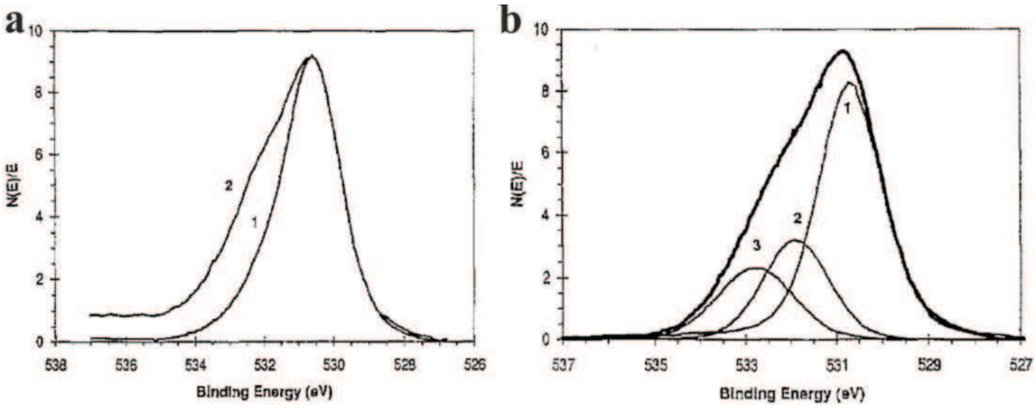

Figure 1.5. (a) O 1s XPS spectra of the first two layers of a SnO_2 surface before (1) and after (2) annealing for gas sensor preparation. The increasing area of the O 1s peak indicates the increasing amount of oxygen on the surface; (b) O 1s XPS spectrum of SnO_2 surface fitted after annealing: peak 1 represents oxygen of the SnO_2 lattice, peak 2 represents chemisorbed OH^-_{ads} or H_2O_{phys} species, and peak 3 represents chemisorbed oxygen ($O^-_{2,ads}$ and O^-_{ads}) or physisorbed $O_{2,phys}$ [182]

However, physisorbed molecular water was completely desorbed when the temperature was raised up to 150 °C, whereas the desorption of hydroxyl groups begins at 250 °C.[184] *Chang* and other groups reported on the chemisorption of oxygen species by using EPR spectra as evidence for the generation of $O^-_{2,ads}$ and O^-_{ads} species, independently.[185-187] Their results confirmed the presence of O^-_{ads} as the major component on the SnO_2 surface at temperatures up to 150 °C, whilst the $O^-_{2,ads}$ was clearly detected at RT and became distinct at 100 °C. The latter results confirmed the IR spectroscopic investigation on oxygen adsorption on SnO_2 surfaces of *Grundrizer* und *Davydov*.[188] When the temperature is raised, chemisorbed $O^-_{2,ads}$ is desorbed from the sample surface while releasing an electron to tin oxide, resulting an increase of conductivity. This process can be summarized with the following equation:

$$O^-_{2,ads} \rightarrow O_{2,ads} + e^-$$

When the temperature is further raised and reaches a certain transition value, the electrons from the CB are trapped and dissociative chemisorption takes place, which results in a decrease of conductivity. This mechanism can be described as follows:[185]

$$O_{2,ads} + 2e^- \rightarrow 2O^-_{ads}$$

$$1/2O_{2,ads} + 2e^- \rightarrow O^{2-}_{ads}$$

Thus, the O_{ads}^{-} specie is supposed to be the most important oxygen ion among the three possible pathways due to its high activity and sensitivity toward the presence of organic vapors or reducing agents.[189] A reducing gas molecule, such as CO, combines with O_{ads}^{-} and is oxidized to CO_2 whereas an electron is released into the CB of semiconductor. Thus, the electric conductivity is a measurable parameter for calibrating the concentration of the target gas. This process can be summed up as follows:[190]

$$CO_{gas} + O_{ads}^{-} \rightarrow CO_{2,gas} + e^{-}$$

$$CO_{gas} + 2O_{ads}^{-} \rightarrow CO_{2,gas} + 1/2O_2 + 2e^{-}$$

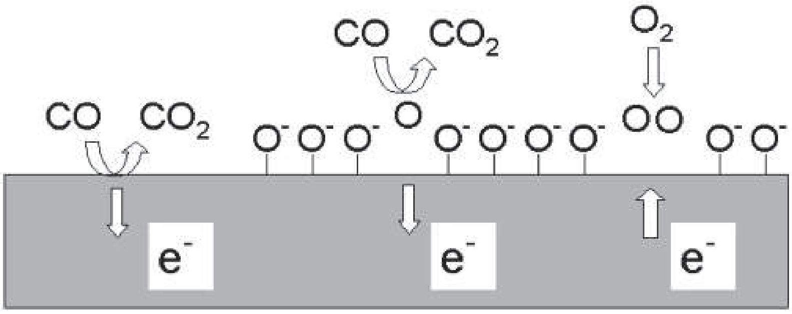

Figure 1.6. Schematic view of interaction between CO and oxygen O_{ads}^{-} of a semiconducting gas sensor (n-type): Chemisorption of oxygen from the air leads to the mobilization of electrons from the conduction band to the near-surface region. Reducing gas molecules, such as CO, interact with the surface-bound oxygen species and release electrons into the bulk, whilst the CO molecules are oxidized to CO_2.[191]

1.3.1.2 Principles of gas sensing measurements

The sensor response (sensitivity) defined as $S = R_{gas} / R_{air}$ or $S = R_{air} / R_{gas}$ describes the ability of detecting a certain concentration of a target gas. The temperature, at which the highest sensor response is achieved, is the so-called optimized operating temperature. This physical parameter is correlated to many conditions such as particle size, morphology, porosity of material and the type of target gas. A typical correlation between gas response and operating temperature of an n-type semiconductor is shown in Figure 1.7 a. The sensing measurements are performed at the best working temperature. The change of resistance or conductivity is observed over the whole gas-in and gas-out processes (Figure 1.7 b).

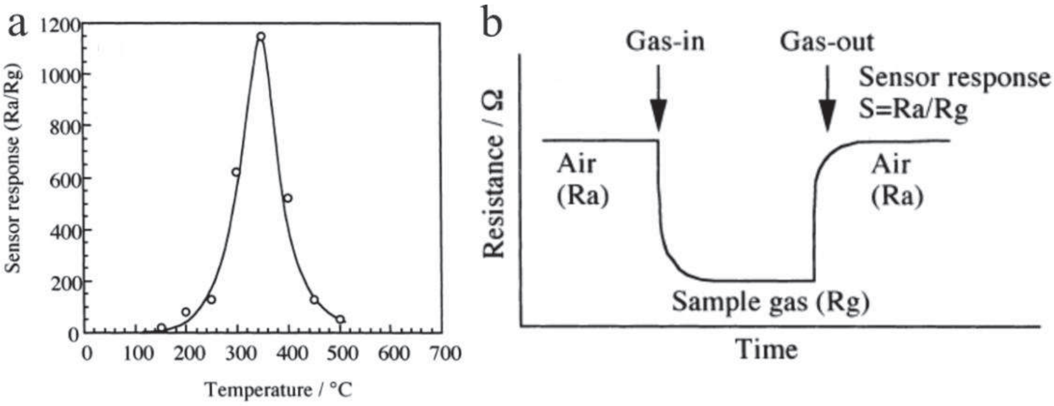

Figure. 1.7. (a) Sensor response of a n-type sensing material is investigated over a broad temperature range from 150 °C to 500 °C. The optimized operating temperature is found to be at 350 °C; (b) A dynamic response and recovery sensing curve of an n-type sensor towards a reducing gas: When the target gas molecules interact with the surface of the semiconductor, the electrons of oxygen species are released and the resistance of the sample drops, which can be expressed as sensor response. When the target gas is removed and air reacts with the sensor, a certain amount of oxygen species on the surface are regenerated and the resistance increases to the initial level.[192]

1.3.1.3 Gas sensor performance characteristics

Generally, sensing performance is influenced by three independent factors:[192]

- Receptor function, which represents the interaction ability of the oxide surface towards the target gas. It is correlated to oxygen adsorptive properties of oxides and chemical/physical characteristics of a target gas.
- Transducer function caused by ability of conversion of the electrical signal
- Special parameters of sensor construction

Theoretically, almost any metal oxide has the capability of solid-state gas sensing.[193] Nevertheless, a good gas sensor needs to fulfill many requirements, which are related to the environmental conditions and purposes. The most important performance-related characteristics of a chemical gas sensor are sensitivity, selectivity and rapid response. However, additional factors need to be considered for industrial applications, such as accuracy, stability, durability and costs. In addition, the portability and minimization of devices are more and more required for contemporary applications.

Semiconducting materials can be classified into two groups:

- n-type sensors: ZnO, SnO_2, TiO_2, In_2O_3, WO_3, CdO and MoO_3 are typical n-type sensors with electrons as major charge carrier. The conductivity increases when a reducing gas (e. g. CO) is detected, whereas the effect of oxidizing gases (e. g. NO_2) is complementary.

- p-type sensors: CuO, NiO and TeO_2 are p-type sensors with hole as major charge carrier. The conductivity decreases when a reducing gas is detected.[194]

Table 1.3. Representative n- and p-type sensing materials.

	Semiconductors	Detected gas
n-type	ZnO	Toluene[195], NH_3[196], LPG[197], H_2S[198,199], Formaldehyde[200]
	SnO_2	CO[201], NO_2[201], H_2[202], O_2[203]
	TiO_2	CO[204], H_2[205], NO_2[206], CO[207]
	In_2O_3	NH_3[208], EtOH[208,209], NO_2[209,210], H_2S[211]
	WO_3	NH_3[212,213], NO_2[214], H_2S[214]
	CdO	LPG[215], CO[216], EtOH[217]
	MoO_3	H_2[218], NO_2[218,219], H_2S[220], CO[221], NH_3[219,222], EtOH[223]
p-type	CuO	EtOH[224], CO[225], NO_2[225]
	NiO	H_2[226], NO_2[227]
	TeO_2	NH_3[228], NO_2[229], CO[230]

A large number of structural parameters, such as grain size, porosity, texture, faceting, grain network etc., influence the gas sensing performance.[231] However, developing a semiconducting material with optimal gas-sensing characteristics still remains a challenging task because improvement of one parameter may induce an adverse change in other parameters.

The surface area is another important factor for sensing performance due to the large amount of active interfacial areas. Generally, very high surface areas may reduce their stability through an increase of surface energy. Therefore, maximization of the surface area must be balanced with the need for sensing stability. From this point of view, it is obvious, that the choice of optimizing structural and morphological properties should be based on equal and simultaneous consideration of all possible consequences.

1.3.2 Humidity sensing applications

1.3.2.1 Challenges in the development of humidity sensors

Humidity is one of the most frequently measured physical properties in different application-oriented fields, because humidity sensors are widely applied as important components in industrial (paper, food, electronic) and pharmaceutical manufacturing, daily household devices, agriculture and environmental monitoring.[232 - 235] Depending on the target applications, specific humidity sensor types are put into practical use in order to meet their corresponding requirements and operation conditions. Some commonly applied devices are summarized in Table 1.4:

Table 1.4. Selected applications of humidity sensors.[236]

Application		**Operating Temperature (°C)**	**Humidity range (RH %)**
Household	Air conditioning system	5 – 40	40 – 70
	Microwave oven	5 – 100	2 – 100
Automobile	Car windows	-20 – 80	50 – 100
Medical service	Medical apparatus	10 – 30	80 – 10
	Incubator	10 – 30	50 – 100
Industry	Drier for ceramic powder	5 – 100	0 – 50
	Textile mill	10 – 30	50 – 100
Agriculture	Forcing culture	5 – 40	0 – 100
Measurement	Radio-sonde	-50 – 40	0 – 100
	Hygrometer	-5 – 100	0 – 100

Generally, an applied industry-suitable humidity sensor needs to fulfill the following requirements:

- High sensitivity over a wide range of humidity values
- Short response time
- Good reproducibility and no or slight hysteresis
- Resistance toward contaminants

- Good durability
- Simple setup structure and low cost fabrication

Many humidity sensors have been utilized in industrial fields despite their suboptimal properties. This leaves plenty of room for developing new types of humidity sensors.

1.3.2.2 Hygrometry measurements

Relative humidity RH is a frequently measured physical parameter in hygrometry. RH is a temperature-related function, which is defined as the ratio of the partial pressure of the water vapor actually present to the partial pressure of water present at saturation in air at the same temperature. RH measurements are usually expressed as a percentage with the following equation:

$$RH = \frac{p_w}{P_s} \cdot 100\%$$

where p_w represents the vapor pressure and p_s the saturation pressure, respectively.

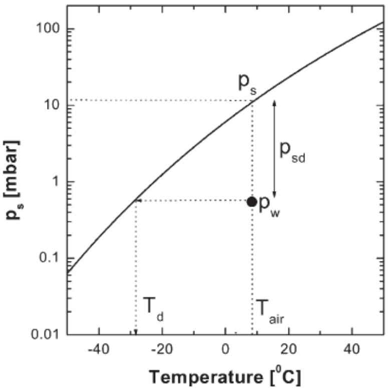

Figure 1.8. Physical relationship between water saturation pressure vs. temperature. T_d represents the dew point, below which the water vapor condenses into liquid water and p_{sd} illustrates the saturation deficit.[237]

1.3.2.3 Types of common humidity sensors

Humidity sensor types can be classified into several groups according to their measured physical parameters. Table 1.5 displays the various types with their advantages and disadvantages:

Table 1.5. Overview of advantages and disadvantages of selected humidity sensor types.

	Operation principles	Advantages	Disadvantages
Optical	Colorimetric interaction of materials	• Resistive to contaminations • Long distance measurement	• Poor sensitivity • High cost
Capacitive	Moisture-induced change	• Low cost • High sensitivity • Good stability • Excellent reproducibility • Easy construction (integrable)	• Low resistance vs. contamination
Impedance (Resistive)	Conductivity change	• Low cost • High sensitivity • Good stability • Excellent reproducibility • Easy construction (integrable)	• Low resistance vs. contamination
Piezoresistive	Electrical resistivity with applied mechanical stress	• Low cost • High sensitivity • Excellent reproducibility • High mechanical stiffness	• Sensitive to temperature change
Magnetoelastic	Change in magnetic flux	• Remote monitoring • Other measurements possible (temperature, pressure etc.) • High sensitivity	• Only applicable to ferromagnetic materials • Short life time • Limited size

It is noteworthy that among a large number of humidity sensors, those working via impedance (or resistance) and capacitance techniques are most widely applied in industry.[237] Both operating principles are based on variation of the electrical conductivity with water vapor. The electrical properties depend on the applied frequency. According to the market research, capacitive technique-related humidity sensors cover over 75 % of market share.[238,239]

Capacitive-type humidity sensors

The capacitance of a given humidity sensing material changes sensitively with the adsorption of water, and this effect is exploited in sensor fabrication. In 1973, the Finnish sensor company *Vaisala* developed the first commercial capacitive humidity sensor Humicape®, which was globally used in radio-sondes and many other humidity measurement fields.

Enlarged surface areas of dielectrics allow free diffusion of the adsorbed water molecules. Interdigital electrode (IDE) as a most preferred design (Figure 1.9 a) results a uniform field distribution. The area of the electrode and the gap spacing are two key factors for the properties of IDE.

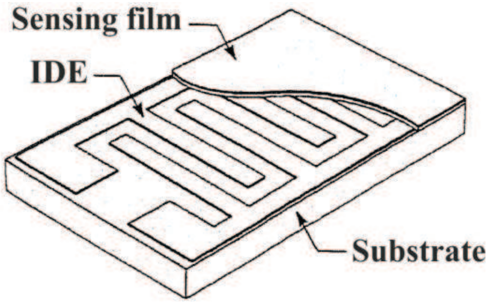

Figure 1.9. IDE construction utilized for semiconducting film sensors.[240]

The models for IDE capacitors have been established by *Jachowicz* et al.[241] in the following complex form:

$$\varepsilon_m = \varepsilon_m^{\prime} - j_m^{\prime\prime} = \varepsilon_m^{\prime} - j\frac{\sigma}{\omega}$$

where $\varepsilon_m^{\prime}$ is the real part and $\varepsilon_m^{\prime\prime}$ is the loss factor, σ is conductivity and ω is frequency of the applied electrical field.

In addition, an exponential behavior is typical of capacitive-type sensing materials.[237] This characteristic can be described by the equation:

$$\frac{C_s}{C_0} = \left(\frac{\varepsilon_w}{\varepsilon_d}\right)^n$$

where ε_d represents the permittivity of the dielectric at a dry state and n is a morphology-related factor.

As a classic example, the dependence of capacitance-humidity of "Humicape" sensor at different frequencies is illustrated in Figure 1.10 for the humidity range from 0 % to 100 %RH:

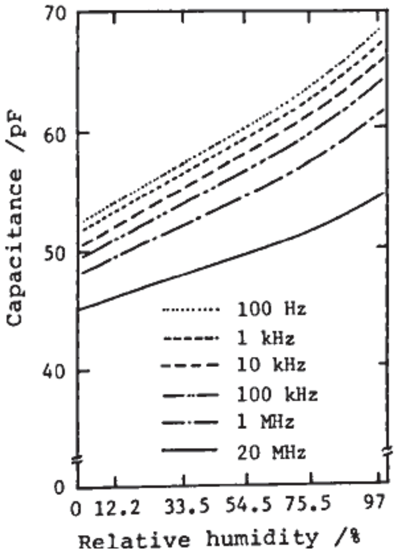

Figure 1.10. Frequency-related humidity characteristics of "Humicape" humidity sensors.[236]

Impedance-type humidity sensors

One of the first mass produced commercial humidity sensor "Dunmore" based on impedance technique was introduced to the market in the 1940s. Due to its high sensitivity, long-term stability and relatively low cost, this sensor is still widely used in alarm and control circuits for compressed and breathing air systems to date.[242]

This type of devices detects moisture by transducing air humidity into an impedance parameter as a result of water adsorption. The impedance change has a typical inverse exponential relationship to RH with respect to temperature. Most impedance sensors use a symmetrical AC excitation voltage at 100 Hz to 10 kHz, while the RH is measured by recording the current flow through the sensing material.[242] Usually, the applied voltage is kept low (1 V) to minimize self-heating effects.

It needs to be pointed out that all so-called "resistive" sensors are not purely resistive. Hence, capacitive and reactive effects are considered together with the resistance as an impedance measurement. The following Figure shows typical resistance-humidity characteristics at different operating temperatures of an impedance-based humidity sensor.

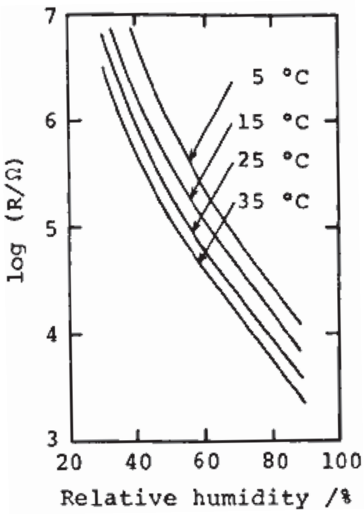

Figure 1.11. Temperature-dependent impedance sensing curves of a humidity sensor based on impedance technique.[236]

The designs of impedance-based and capacitive humidity sensors are often comparable, i.e. planar devices of IDE. Similar to the operating principle of capacitive sensors, the ionic mobility increases with the water adsorption (high-moisture atmosphere), which leads to higher ionic conductivity during the process.

1.3.2.4 Humidity sensing materials

Many different material types have been studied as humidity sensing materials. Among them, three groups of materials have mainly been applied in the last decades, namely polymers,[243-246] ceramics[247-250] and semiconducting metal oxides.[113,251,252] Compared to other two groups, metal oxides offer the advantages of low cost,[253] high stability[254,255] and long-term reliability.[256] Water adsorption increases the conductivity of an n-type semiconducting sensing material and decreases the conductivity of a p-type sensing material. Usually at room temperature, the conductivity of a semiconducting sensing material is caused by addition of electrons and protons (ionic conduction).[257] Due to the large family of semiconducting oxides and heir virtually inexhaustible modifications, many research groups have reported on the humidity sensing properties of phase pure oxides as well as of homogeneously oxide mixtures as shown in Table 1.6.

Table 1.6. Selection of binary and ternary oxides with humidity sensing properties.

	Oxide types	Materials	Ref.
Pure	Binary oxides	Manganese oxides	[258]
		ZnO	[259,260]
		SnO_2	[261]
		WO_3	[262,263]
		CuO	[264]
		In_2O_3	[265,266]
	Ternary oxides	$Na_2Ti_3O_7$	[267]
		$BaTiO_3$	[268]
		$ZnWO_4$	[269]
		Perovskite (AXO_3)	[270-273]
	Others	$Bi_{0.5}K_{0.5}TiO_3$	[274]
Mixture		ZnO-Y_2O_3	[275]
		$MgCr_2O_4$-TiO_2	[276]
		TiO_2-V_2O_5	[277]
		MgO-K_2O-Fe_2O_3	[278]
		$ZnCr_2O_4$-$LiZnVO_4$	[279,280]

1.3.2.5 Humidity sensing mechanisms

The conduction mechanism depends on the surface coverage through adsorbed water molecules. Two types of water adsorption take place during the humidity sensing process: in the beginning chemisorption occurs at low humidity value, followed by physisorption at high humidity. The chemisorption and physisorption processes on the surface of metal oxides have been studied and reported in the 1970s by several research groups.[281,282] Once the initial chemisorbed layer is formed, it is not affected by exposure to humidity due to its stable chemical bonding to the surface. Complete desorption of water molecules can only occur at higher temperature.[283, 284] These mechanisms of chemisorption and physisorption are illustrated in Figure 1.12.

The humidity sensing mechanism of a semiconductor-based sensor can be divided into two stages:

- Hydronium diffusion on hydroxyl groups dominates in a “non-Debye” process in the low humidity range (non-continuous water layer), and proton transfer takes place as well.
- In an “ion-transport” process in the high humidity range, proton hopping between neighboring water molecules mainly occurs in the continuous water-like film.

Taking aluminum oxide as an example, water molecules interact with the oxide surface in the first step. After formation of adsorption complexes (Figure 1.12 a I and a II), the partially negatively charged oxygen atom of water molecule is bonded to the cationic site and subsequently converted into a chemisorbed hydroxyl group (Figure 1.12 a III), which induces high local charge density and a strong electrostatic field. Afterwards, the physisorption of the first water molecule layer can occur on these adjacent surface hydroxyl groups (Figure 1.12 a IV) because of the high electrostatic fields in the chemisorbed layer. In this case, protons hop from site to site across the surface due to the non-continuous water layer. In a high-moisture atmosphere, the physisorption changes from monolayers to multilayers. Further water molecules are then attached to the hydroxyl group to form a water-like layer as illustrated in Figure 1.12 b. A water molecule is attached to a proton to form a hydronium ion, which releases a proton to the neighboring water molecule. The next water molecule accepts the proton while releasing another proton to the neighboring water molecule. This proton transfer between the hydronium ions is known as the *Grotthus* mechanism and also represents the conduction processes taking place in liquid water.[248] The concentration of protons increases with increasing humidity values, thereby the transfer of proton is accelerated through the water-like network,[281] which results in the hopping of protons from one water molecule to another and a sharp impedance decrease.

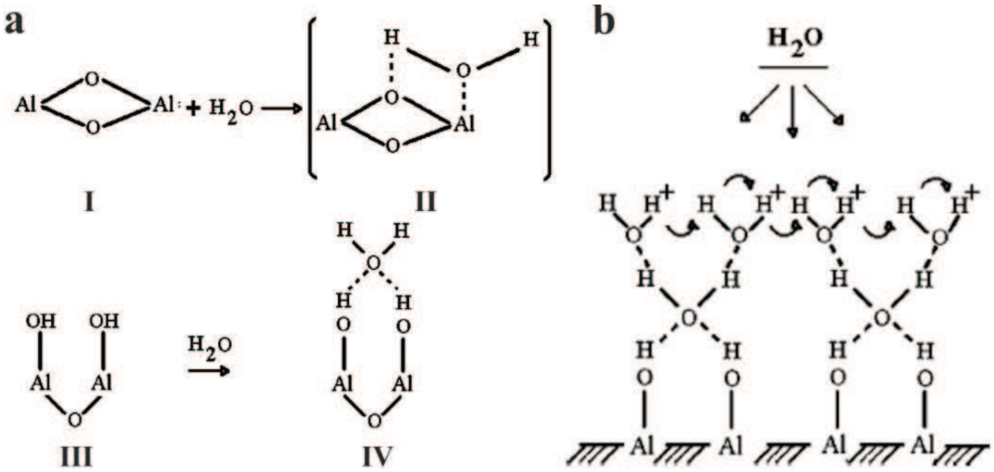

Figure 1.12. (a) Schematic illustration of the interaction of a water molecule with an alumina surface; (b) schematic representation of adsorbed water molecules forming layers on the surface.[285]

Moreover, the response and recovery times are important parameters to describe the sensing properties. The response/recovery time is defined as the time required for the sensor output to reach 90 % of its saturation value in the adsorption or desorption process.

1.4 Experimental setups and liftoff techniques

1.4.1 Humidity sensing setup

Humidity sensing measurements were performed on a WAYNE KERR 4300 LCR Meter (Chapter 2) and on a TH 2617 LCR analyzer (Chapter 3). Humidity environments with corresponding RH levels are simulated using saturated solutions of different salts as humidity generation sources. The sensor is put in a closed glass vessel with RH levels of 11%, 33 %, 55 %, 75 %, 85 % and 95 %, which are created with LiCl, $MgCl_2$, $Mg(NO_3)_2$, NaCl, KCl and KNO_3, respectively. All measurements were carried out at ca. 28 °C. The applied AC voltage in Chapter 2 and 3 was kept constant 1 V and the frequency was varied from 100 Hz to 100 kHz.

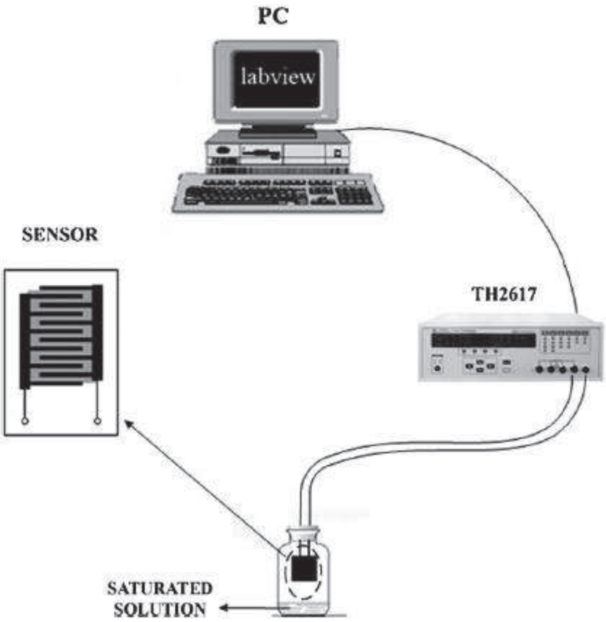

Figure 1.13. Schematic representation of the sensing measurement setup and of the constructed humidity sensors.[286]

1.4.2 Gas sensing setup

Gas sensing measurements are performed in a house-made test chamber made of steel. The gas sensor is mounted on an electric heating system, which maintains the operating temperature and is directly regulated by an external heating controller. The temperature for sensor tests can be increased up to 400 °C, which is in the range of typical sensor operating temperatures (100 – 400 °C). The nominal and actual temperatures are recorded in real time. Mass flowmeters are connected to the dry synthetic air as carrier gas and the target gas. The computer-assisted gas calibration system is programmed for exposing the sensor to arbitrary concentrations (up to 100 ppm) of target gases. An LCR meter records the resistance change of gas sensor with a recording rate of 1 data point per second on the computer. The total flow rate is kept constant at 500 sccm (standard cubic centimeters per minute). A schematic view is presented in the following Figure 1.14.

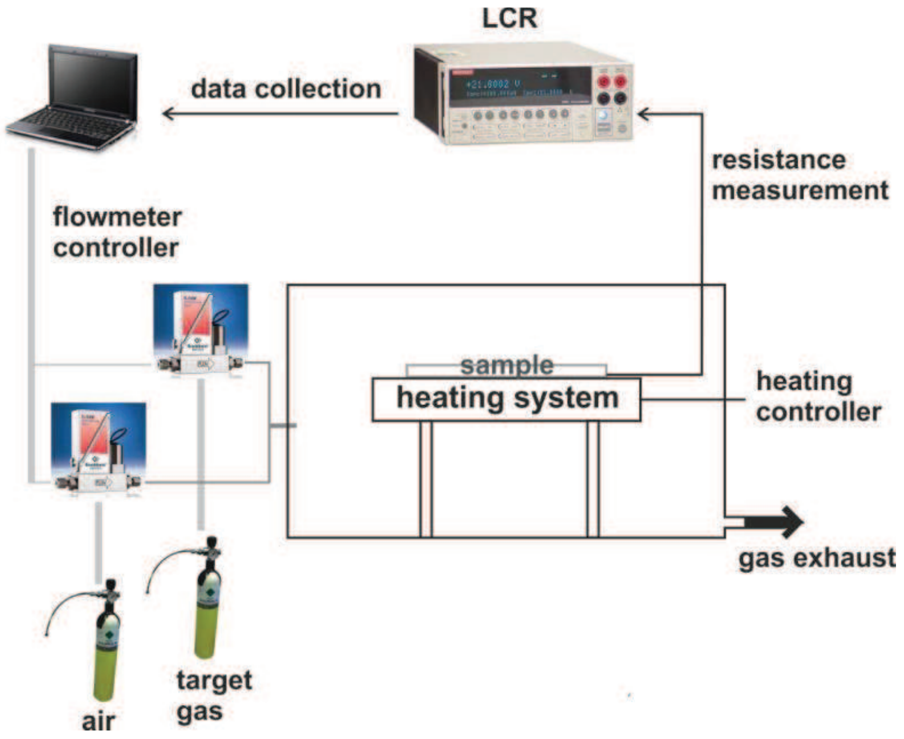

Figure 1.14. Schematic representation of gas sensor test system and laboratory setup.

1.4.3 Sensor fabrication techniques

In principle, impedance- and capacitive-type sensors are based on dielectric changes of thin sensing films upon water vapor adsorption. The common constructions of capacitive sensors are schematically summarized in Figure 1.15.

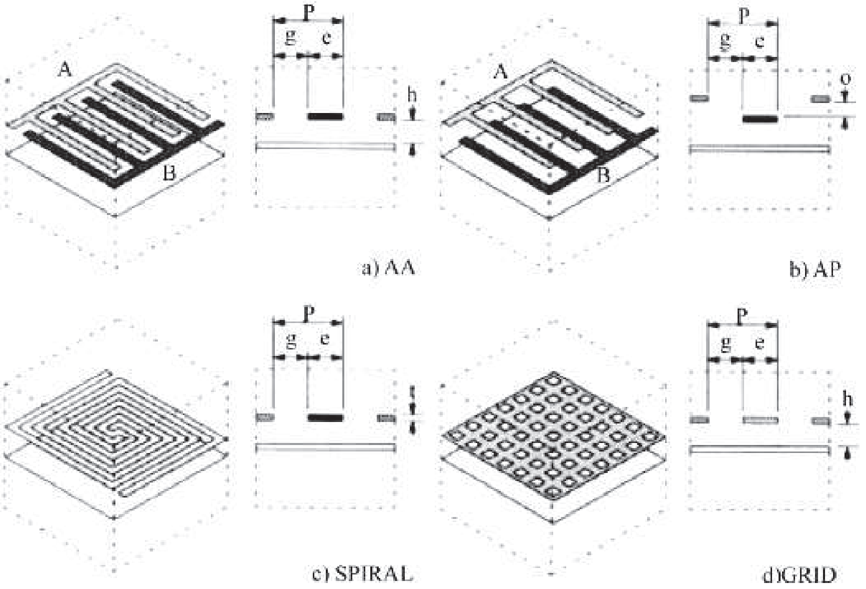

Figure 1.15. Schematic views of different constructions of capacitive sensors.[237]

In this work, two different sensor fabrication methods are applied. For gas sensing measurements, an IDE with a small finger distance (25 µm) is fabricated by means of photolithography technique carried out in clean room facilities of FIRST (Frontiers In Research: Space & Time, ETHZ). For humidity sensing measurements, the IDE is fabricated by evaporating a bilayer metal film (titanium and gold) to enable resistance measurements of the sensing material. Both types of electrode are constructed on a cleaned quartz glass as substrate and schematic views are displayed in the following.

1.4.3.1 Electrode fabrication techniques

All IDE applied for gas sensing measurements were fabricated by photolithography techniques in clean room facilities. This technique enables fabrication of different kinds of electrodes, and it is a convenient way for transferring geometric patterns on a mask to the surface of a silicon wafer with a light-sensitive material by selective exposure. After miscellaneous chemical and photochemical treatments, a required pattern on the substrate (mostly silicon wafer) protected by photoresist can be created. A typical photolithography process consists of the following steps:

- Cleaning process
- Spin coating photoresist
- Exposure and development
- Evaporation of metal layer
- Removal of residual photoresist

First, the substrate must be cleaned by wet chemical treatments in order to remove organic and inorganic contaminants on the surface. This is a key step for sensor fabrication because a contaminated surface can result in poor adherence of photoresist and metal layer. Usually, silicon wafers are sonicated in acetone and then in ethanol at room temperature for few minutes. After the cleaning process, the substrate is treated on a heating plate to remove the organic solvents and then fixed on a vacuum chuck of the spinner. The spinning speed is specific to the kind of photoresist and results in a desirable thickness of the resist film. A uniformly thin photoresist layer is formed by dropping a certain amount of photoresist on the substrate and then being spun rapidly. The wafer is covered with photoresist and pre-heated to drive off excess photoresist solvent. After the pretreatment process, the photoresist can be exposed to intense UV light and the pattern of the photomask can be either equally or inversely transferred on the substrate. The photoresists are light-sensitive polymers with tunable physical and chemical properties (i.e. they can either selectively be etched or retained) upon exposure to UV light. Depending on their photosensitive properties, they can transfer the copied or inverse pattern of the photomask. Basically, photoresists are classified into two groups: positive and negative photoresists.

- A positive photoresist is a type of polymer which changes its chemical structure after UV light exposure. The exposed part becomes soluble and can be washed away by the specific photoresist developer. The unexposed part of the photoresist remains on the substrate and contains an exact copy of the photomask pattern.

- In a complementary manner, the negative photoresist type undergoes polymerization after exposure to UV light. The polymerized part becomes insoluble and developer-resistant, whereas the unexposed part is removable by the photoresist developer. An inverse pattern remains on the substrate after using a negative photoresist.

A post-exposure treatment process follows directly after the exposure process. After development, the required pattern is transferred on the substrate which is exactly covered or inversely covered by photoresist (depending on the type of photoresist used). At this point, the exposed position on the substrate can be evaporated by different metal layers. Afterwards, the photoresist is no longer required and must be removed from the substrate by resist removal. The evaporated metal layer of electrode pattern adheres to substrate and can be applied for the further measurements.

A schematic illusion of lift-off-techniques for sensor fabrication is presented in Figure 1.16. The different effects of positive and negative photoresist are demonstrated in the latter steps.

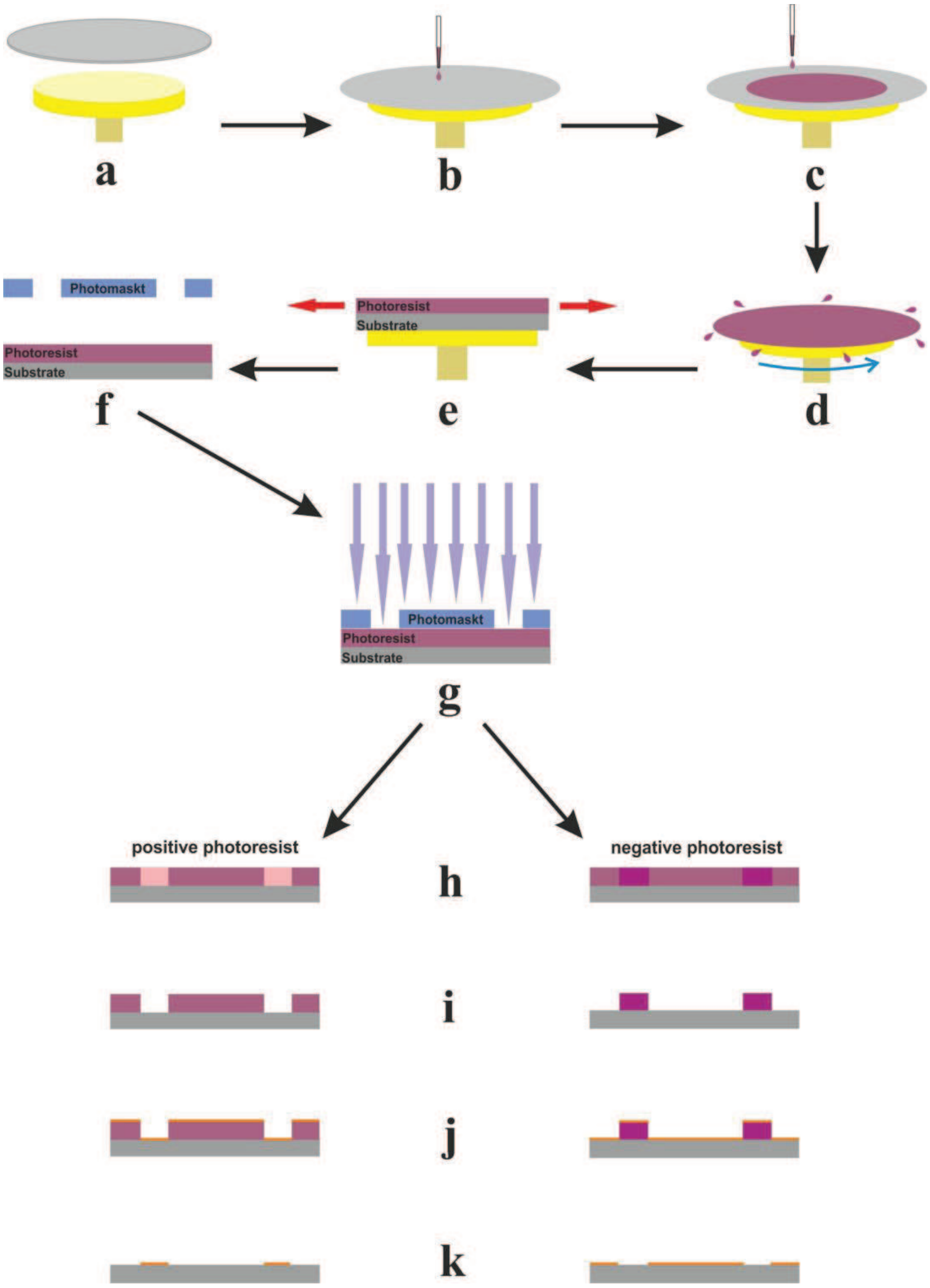

Figure 1.16. Schematic view of photolithography process of a positive (left) and a negative (right) photoresist: (a) preparation of the substrate (cleaning process); (b) position of substrate on the vacuum chuck; (c) deposition of photoresist as sacrificial stencil layer; (d) spin coating; (e) formation of a uniform thin photoresist layer; (f) photomask alignment; (g) exposure; (h) exposed areas become soluble (for positive photoresist) or insoluble (for negative photoresist); (i) development; (j) evaporation of metal layers; (k) stripping.

In this work, the special photoresist AZ 5214E was applied for lift-off-techniques. This positive photoresist is capable of image reversal (IR) mode in a negative pattern of the mask, which results in a unique undercut and a higher resolution for evaporated or sputtered films. After exposure to UV light, the exposed areas are selectively cross-linked by a reversal heat treatment process. This results in inactivity of the exposed areas of photoresist, which is not removable in the development process. A flood exposure (without photomask) converts unexposed areas into soluble ones, which results in a negative image mode. The soluble part of the photoresist can be removed by using the developer AZ 726. The exposed areas on the substrate with a desired electrode pattern are evaporated by a bilayer Ti-Au-film (thickness of Ti-film: 10 nm and of Au-film: 200 nm). Afterwards, the remaining inert photoresist can be removed by a photoresist removal. The entire lift-off process is shown in the following Figure 1.17.

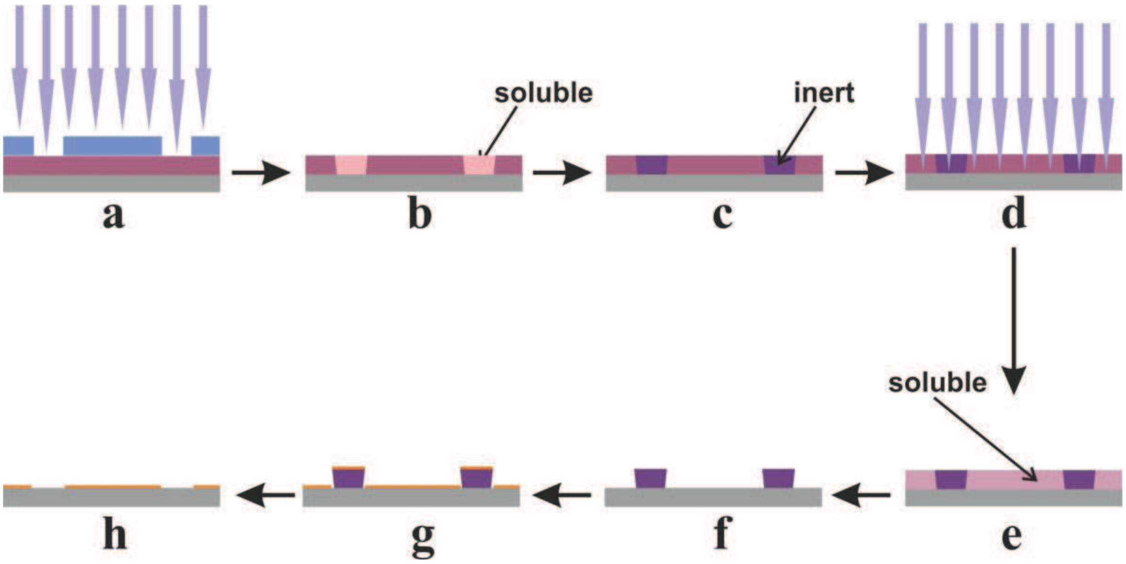

Figure 1.17. Schema of a photolithography process using AZ 5214E in the image reversal mode: (a) exposure; (b) exposed areas become soluble; (c) reversal bake; (d) flood exposure (without photomask); (e) unexposed areas become soluble; (f) development; (g) evaporation of metal layers; (h) stripping.

An IDE is applied for all gas sensing measurements. Microscope slides (MENZEL-GLÄSER) with ultrahigh resistance were chosen as electrode substrates. The schema of electrode patterning is illustrated in Figure 1.18.

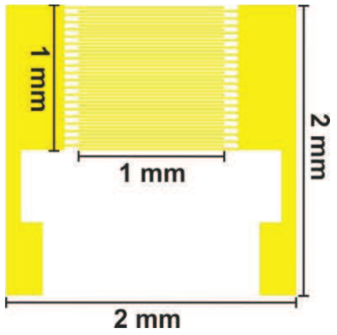

Figure 1.18. Pattern of applied IDE for gas sensing measurements: The glass is cut as a 2 mm x 2 mm substrate and the electrode pattern is fabricated on the surface. The distance of electrode fingers is set as 25 µm.

For all humidity sensing measurements in this work, a different IDE with a finger distance of 200 µm is applied. The electrode was fabricated by evaporating a bilayer metal film (thickness of Ti-film: 10 nm and of Au-film: 200 nm) on a glass substrate. Due to the large finger distance, lift-off-techniques are not required. A required pattern was fixed on a clean glass substrate and then the desirable metal layers were evaporated. The electrode pattern is illustrated as follows:

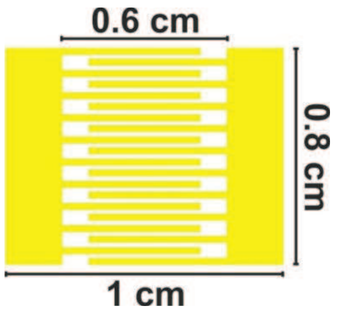

Figure 1.19. Electrode pattern with a finger distance of 200 µm for humidity sensing measurements.

1.4.3.2 Sensor fabrication

For the fabrication of gas sensors, the give as-synthesized nanoscale oxide product is mixed with DI water in ultrasonic bath to form a dispersion which was then put on the electrode to create a uniformly distributed thin film with a thickness of about 10 µm. The distribution of the sensing material on the electrode can be controlled with SEM measurements shown in Figure 1.20.

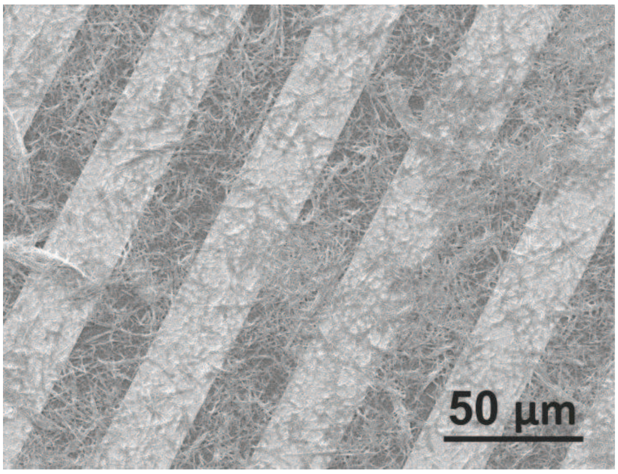

Figure 1.20. Representative nanobelt-shaped oxide sample on the fabricated IDE (bright: gold film, dark: substrate)

Humidity sensors were prepared according to "*Doctor Blade*" method.[287] 200 mg as-synthesized powders are mixed with 0.2 mL terpineol with 5 wt% ethylcellulose and 0.04 mL acetylacetone to form a thick paste. After grinding, the paste is coated onto the evaporated electrode. Then the film is sintered in air at 150 °C for 10 min, 350 °C for 10 min and 500 °C for 30 min to remove the organic additives, respectively. After cooling down to the room temperature, a uniformly distributed film with a thickness of about 10 µm is obtained.

1.5 Goals and strategy of this PhD thesis

1.5.1 Goals

First, we access binary and ternary micro- and nanoscale oxides with interesting sensing properties via convenient and novel "one-pot" hydrothermal routes. Along the lines of our previous research,[126,137,285,288] we focus on improving the surface performance of materials by tuning with shape-directing additives or coating with nanoparticles to enhance the sensing performance. Furthermore, we aim to understand the dependence of sensing behavior on the structural and surface properties of functional TMOs.

1.5.2 Target compounds of the present thesis

The target compounds for this thesis were chosen along the lines of our previous work on molybdenum-containing[20,125,129,135,137,138,160,287] oxides and bismuth-containing[6,7,20,126,127,130,145,287,288] materials as promising candidates for new sensor materials.

Starting from commercial Bi_2O_3 as bismuth source, $Bi_2O_2CO_3$ nanosheets were synthesized via a convenient one-pot protocol at room temperature. Their layered structure consisting of alternating $Bi_2O_2^{2+}$ and CO_3^{2-} layers, which is similar to *Aurivillius* type Bi_2MO_6 (M = W, Mo), may account for their promising humidity sensing characteristics (Chapter 2). Sillenite- and mozanite-type bismuth phosphates were obtained via a hydrothermal approach using various bismuth and phosphate precursors. The crystal structures of bismuth-containing oxides lead to the formation of surface areas with different chemical properties, thus giving rise to distinct humidity sensing behaviors (Chapter 3). Whereas monazite-type $BiPO_4$ contains a stoichiometric amount of PO_4^{3-} groups, sillenite-type bismuth phosphate incorporates lower amounts of phosphate anions into its channels with Bi/P ratios between 13:1 and 16:1. This renders both compounds drastically different with respect to their structural characteristics and polarity. In the following, we explore the consequence of these different structural motifs on the humidity sensing properties.

As outlined in preceding studies, orthorhombic MoO_3 is a very versatile sensing material for a variety of test gases.[289-291] However, the improvement of MoO_3 sensor fibers through combination with quantum dots of a different oxide semiconductor remains to be fully explored. Based on hydrothermal synthesis routes to α-MoO_3 rods and SnO_2 quantum dots, we thus implemented their coating into MoO_3/SnO_2 heterojunctions. The enhanced hydrogen gas sensing properties of the resulting MoO_3/SnO_2 heterostructure nanocomposites were newly investigated (Chapter 4).

Whereas orthorhombic molybdenum oxide has attracted considerable research interest for gas sensor construction, its metastable hexagonal modification has been far less investigated as a sensor material. As pure hexagonal molybdate remains difficult to access, because its large channels are mostly stabilized through incorporation of cations (preferably alkali and ammonium cations),[292] we opted for sensing investigations on hexagonal alkali molybdate. Here we started from $KMo_5O_{15}OH{\cdot}2H_2O$ as the structural prototype with K^+ as stabilizer in the hexagonal tunnels.[293] We then utilized the multiple role of potassium cations for tuning the structure, morphology and particle size of hexagonal molybdenum oxides (h-K-MoO_3). Their ammonia sensing properties with promising response and high selectivity are discussed in Chapter 5.

1.5.3 Overall research strategy

The research strategy of this thesis is summarized in Figure 1.21. Based on our previous work on TMO-based sensors, the property requirements and the choice of starting materials are clearly defined. This enables us to start with a rational strategic pathway toward the final goals (step 1). Different physical properties of TMOs, such as chemical composition, crystal structure, morphology, surface-to-volume ratio, band gap, oxygen vacancies, hydrophilic surface etc., influence their sensing behaviors and their applications. This requires a flexible synthetic approach, which provides a variety of parameters to modify the abovementioned criteria. For this work, hydrothermal routes are the method of choice for synthesizing the target materials (step 2). Next, the analyses of as-synthesized materials are performed and the corresponding properties are studied (step 3). In the following, the humidity and gas sensing activities of the obtained and characterized materials are investigated. Relationships between sensing characteristics, mechanisms and materials properties are studied and discussed to better understand the complex structure-synthesis-activity relationships within these systems (step 4). Finally, an additive-assisted hydrothermal approach to Mo-based sensor is developed by tuning the concentrations of shape-directing additives to improve the sensing activities. Coating of as-synthesized Mo-based oxide materials with nanoparticles obtained via hydrothermal routes is another alternative strategy to enhance their sensing performance (step 5).

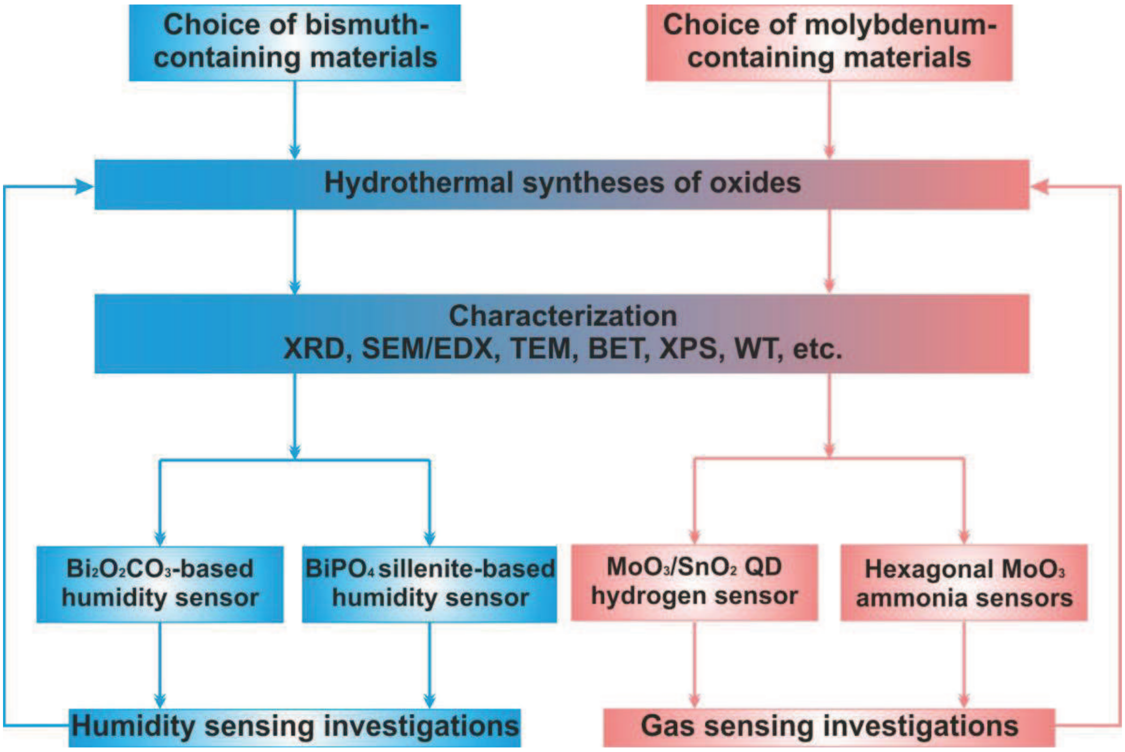

Figure 1.21. Flowchart of research strategies of the present thesis.

References

---

[1] F. Falaras, T. Stergiopoulos, D. S. Tsoukleris, *Small* **2008**, *4*, 770-776.
[2] Y. Luo, D. Li, Q. Meng, *Adv. Mater.* **2009**, *21*, 4647-4651.
[3] M. Law, L. E. Greene, J. C. Johnson, R. Saykally, P. D. Yang, *Nature Mater.* **2005**, *4*, 455-459.
[4] J. Qian, P. Liu, Y. Xiao, Y. Jiang, Y. Cao, X. Ai, H. Yang, *Adv. Mater.* **2009**, *21*, 3663.
[5] G. R. Meseck, R. Kontic, G. R. Patzke, S. Seeger, *Adv. Funct. Mater.* **2012**, *22*, 4433-4438.
[6] D. Ressnig, R. Kontic, G. R. Patzke, *Mater. Chem. Phys.* **2012**, *135*, 457-466.
[7] R. Kontic, G. R. Patzke, *J. Solid State Chem.* **2012**, *189*, 38-48.
[8] D. J. L. Brett, A. Atkinson, N. P. Brandon, S. J. Skinner, *Chem. Soc. Rev.* **2008**, *37*, 1568-1578.
[9] S. C. Singhal and K. Kendall, *High-Temperature Solid Oxide Fuel Cells: Fundamentals, Design and Applications*, Elsevier Science, Oxford, UK, **2003**.
[10] Y. L. Wang, X. C. Jiang, Y. N. Xia, *J. Am. Chem. Soc.* **2003**, *125*, 16176-16177.
[11] O. K. Varghese, C. A. Grimes, *J. Nanosci. Nanotechnol.* **2003**, *3*, 277-293.
[12] N. Barsan, M. Schweizer-Berberich, W. Gopel, *Fresenius J. Anal. Chem.* **1999**, *365*, 287-304.
[13] M. Sheng, L. Gu, R. Kontic, Y. Zhou, K. Zheng, G. Chen, X. Mo, G. R. Patzke, *Sens. Actuators B* **2012**, *166*, 642-649.
[14] A. S. Arico, P. Bruce, B. Scrosati, J. M. Tarascon, W. Van Schalkwijk, *Nature Mater.* **2005**, *4*, 366-377.
[15] Z. Chen, Y. Qin, D. Weng, Q. Xiao, Y. Peng, X. Wang, H. Li, F. Wei, Y. Lu, *Adv. Funct. Mater.* **2009**, *19*, 3420-3426.
[16] S. W. Li, R. Funahashi, I. Matsubara, K. Ueno, S. Sodeoka, H. Yamada, *Chem. Mater.* **2000**, *12*, 2424-2427.
[17] W. Kobayashi, S. Hebert, D. Pelloquin, O. Perez, A. Maignan, *Phys. Rev. B* **2007**, *76*.
[18] T. Seiyama, A. Kato, K. Fujiishi, M. Nagatani, *Anal. Chem.* **1962**, *34*, 1502-1504.
[19] N. Yamazoe, *Sens. Actuators B* **2005**, *108*, 2-14.
[20] G. R. Patzke, F. Krumeich, R. Nesper, *Angew. Chem. Int. Ed.* **2002**, *41*, 2446-2461.
[21] G. Shen, P. C. Chen, K. Ryu, C. Zhou, *J. Mater. Chem.* **2009**, *19*, 828-839.
[22] K. S. Shankar, A. K. Raychaudhuri, *Mater. Sci. Eng. C* **2005**, *25*, 738-751.
[23] N. A. Chernova, M. Roppolo, A. C. Dillon, M. S. Whittingham, *J. Mater. Chem.* **2009**, *19*, 2526-2552.
[24] M. J. Fuller, M. E. Warwick, *J. Catal.* **1973**, *29*, 441-450.
[25] P. A. Sermon, V. A. Self, E. P. S. Barrett, *J. Mol. Catal.* **1991**, *65*, 377-384.

[26] D. Manno, G. Micocci, A. Serra, A. Tepore, *J. Appl. Phys.* **1998**, *83*, 3541-3546.

[27] J. R. Stetter, W. R. Penrose, S. Yao, *J. Electrochem. Soc.* **2003**, *150*, S11-S16.

[28] P. D. Yang, H. Q. Yan, S. Mao, R. Russo, J. Johnson, R. Saykally, N. Morris, J. Pham, R. R. He, H. J. Choi, *Adv. Funct. Mater.* **2002**, *12*, 323-331.

[29] Y. W. Wang, L. D. Zhang, G. Z. Wang, X. S. Peng, Z. Q. Chu, C. H. Liang, *J. Cryst. Growth* **2002**, *234*, 171-175.

[30] F. Krumeich, H. J. Muhr, M. Niederberger, F. Bieri, B. Schnyder, R. Nesper, *J. Am. Chem. Soc.* **1999**, *121*, 8324-8331.

[31] B. C. Satishkumar, A. Govindaraj, E. M. Vogl, L. Basumallick, C. N. R. Rao, *J. Mater. Res.* **1997**, *12*, 604-606.

[32] Y. Ono, K. Nakashima, M. Sano, J. Hojo, S. Shinkai, *J. Mater. Chem.* **2001**, *11*, 2412-2419.

[33] G. H. Du, Q. Chen, R. C. Che, Z. Y. Yuan, L. M. Peng, *Appl. Phys. Lett.* **2001**, *79*, 3702-3704.

[34] L. Z. Wang, S. Tomura, F. Ohashi, M. Maeda, M. Suzuki, K. Inukai, *J. Mater. Chem.* **2001**, *11*, 1465-1468.

[35] A. Dobley, K. Ngala, S. F. Yang, P. Y. Zavalij, M. S. Whittingham, *Chem. Mater.* **2001**, *13*, 4382-4386.

[36] Y. B. Li, Y. Bando, T. Sato, *Chem. Phys. Lett.* **2002**, *359*, 141-145.

[37] C. K. Xu, G. D. Xu, Y. K. Liu, G. H. Wang, *Solid State Commun.* **2002**, *122*, 175-179.

[38] L. Guo, J. X. Cheng, X. Y. Li, Y. J. Yan, S. H. Yang, C. L. Yang, J. N. Wang, W. K. Ge, *Mater. Sci. Eng. C* **2001**, *16*, 123-127.

[39] X. Wang, Y. D. Li, *J. Am. Chem. Soc.* **2002**, *124*, 2880-2881.

[40] S. Somiya, R. Roy, *Bull. Mat. Sci.* **2000**, *23*, 453-460.

[41] S. H. Feng, R. R. Xu, *Acc. Chem. Res.* **2001**, *34*, 239-247.

[42] Y. D. Yin, G. T. Zhang, Y. N. Xia, *Adv. Funct. Mater.* **2002**, *12*, 293-298.

[43] C. C. Tang, Y. Bando, T. Sato, *J. Phys. Chem. B* **2002**, *106*, 7449-7452.

[44] Z. R. Dai, J. L. Gole, J. D. Stout, Z. L. Wang, *J. Phys. Chem. B* **2002**, *106*, 1274-1279.

[45] Z. L. Wang, R. P. P. Gao, J. L. Gole, J. D. Stout, *Adv. Mater.* **2000**, *12*, 1938-1940.

[46] C. H. Liang, G. W. Meng, Y. Lei, F. Phillipp, L. D. Zhang, *Adv. Mater.* **2001**, *13*, 1330-1333.

[47] M. S. Arnold, P. Avouris, Z. W. Pan, Z. L. Wang, *J. Phys. Chem. B* **2003**, *107*, 659-663.

[48] P. X. Gao, Y. Ding, W. J. Mai, W. L. Hughes, C. S. Lao, Z. L. Wang, *Science* **2005**, *309*, 1700-1704.

[49] L. Vayssieres, *Adv. Mater.* **2003**, *15*, 464-466.

[50] J. J. Wu, S. C. Liu, *Adv. Mater.* **2002**, *14*, 215-218.

[51] N. Sakai, K. Fukuda, Y. Omomo, Y. Ebina, K. Takada, T. Sasaki, *J. Phys. Chem. C* **2008**, *112*, 5197-5202.

[52] Y. Wu, B. Q. Xu, *Chin. Sci. Bull.* **2005**, *50*, 2153-2156.

[53] U. Ozgur, D. Hofstetter, H. Morkoc, *Proc. IEEE* **2010**, *98*, 1255-1268.

[54] E. Comini, *Anal. Chim. Acta* **2006**, *568*, 28-40.

[55] Y. Z. Lv, L. Guo, H. B. Xu, X. F. Chu, *Phys. E* **2007**, *36*, 102-105.

[56] G. Li, S. Kawi, *Sens. Actuators B* **1999**, *59*, 1-8.

[57] K. Byrappa, T. Adschiri, *Prog. Cryst. Growth Charact. Mater.* **2007**, *53*, 117-166.

[58] H. Hayashi, Y. Hakuta, *Materials* **2010**, *3*, 3794-3817.

[59] B. L. Cushing, V. L. Kolesnichenko, C. J. O'Connor, *Chem. Rev.* **2004**, *104*, 3893-3946.

[60] K. W. Hutchenson, N. R. Foster, *Innovations in Supercritical Fluids: Science and Technology, Vol. 608* (Eds.: K. W. Hutchenson, N. R. Foster), **1995**, pp. 1-31.

[61] H. Ksibi, P. Subra, *Adv. Powder Technol.* **1996**, *7*, 21-28.

[62] K. Chhor, J. F. Bocquet, C. Pommier, *Mater. Chem. Phys.* **1995**, *40*, 63-68.

[63] R. A. Laudise, D. W. Johnson, *J. Non-Cryst. Solids* **1986**, *79*, 155-164.

[64] G. R. Patzke, Y. Zhou, R. Kontic, F. Conrad, *Angew. Chem. Int. Ed.* **2011**, *50*, 826-859.

[65] M. Figlarz, *Soft Chemistry Routes to New Materials*, **1994**.

[66] J. Rouxel, *Adv. Synth. React. Solids* **1994**, 2, 27.

[67] M. Yoshimura, W. L. Suchanek, K. Byrappa, *MRS Bull.* **2000**, *25*, 17-25.

[68] R. P. Andres, J. D. Bielefeld, J. I. Henderson, D. B. Janes, V. R. Kolagunta, C. P. Kubiak, W. J. Mahoney, R. G. Osifchin, *Science* **1996**, *273*, 1690-1693.

[69] C. T. Kresge, M. E. Leonowicz, W. J. Roth, J. C. Vartuli, J. S. Beck, *Nature* **1992**, *359*, 710-712.

[70] G. Spezia, *Atti Accad. Sci. Torino* **1900**, *35*, 95.

[71] R. A. Laudise, *Chem. Eng. News* **1987**, *65*, 30-43.

[72] G. C. Kennedy, *American J. Sci.* **1950**, *248*, 540-564.

[73] K. Byrappa, *Kirk-Othmer Encyclopedia of Chemical Technology*, John Wiley and Sons, London, **2005**.

[74] S. Forster, M. Antonietti, *Adv. Mater.* **1998**, *10*, 195-217.

[75] Y. C. Zhu, H. G. Zheng, Y. A. Li, L. S. Gao, Z. P. Yang, Y. T. Qian, *Mater. Res. Bull.* **2003**, *38*, 1829-1834.

[76] V. F. Puntes, K. M. Krishnan, A. P. Alivisatos, *Science* **2001**, *291*, 2115-2117.

[77] Q. Xie, Z. Dai, W. W. Huang, J. B. Liang, C. L. Jiang, Y. T. Qian, *Nanotechnol.* **2005**, *16*, 2958-2962.

[78] W. Liu, W. Zhong, X. L. Wu, N. J. Tang, Y. W. Du, *J. Cryst. Growth* **2005**, *284*, 446-452.

[79] Z. P. Liu, S. Li, Y. Yang, S. Peng, Z. K. Hu, Y. T. Qian, *Adv. Mater.* **2003**, *15*, 1946-1948.

[80] K. Byrappa, K. M. L. Rai, M. Yoshimura, *Environ. Technology* **2000**, *21*, 1085-1090.

[81] S. Pavasupree, Y. Suzuki, S. Yoshikawa, R. Kawahata, *J. Solid State Chem.* **2005**, *178*, 3110-3116.

[82] H. M. Cheng, J. M. Ma, Z. G. Zhao, L. M. Qi, *Chem. Mater.* **1995**, *7*, 663-671.

[83] M. H. Huang, S. Mao, H. Feick, H. Q. Yan, Y. Y. Wu, H. Kind, E. Weber, R. Russo, P. D. Yang, *Science* **2001**, *292*, 1897-1899.

[84] V. A. L. Roy, A. B. Djurisic, W. K. Chan, J. Gao, H. F. Lui, C. Surya, *Appl. Phys. Lett.* **2003**, *83*, 141-143.

[85] C. W. Sun, H. Li, H. R. Zhang, Z. X. Wang, L. Q. Chen, *Nanotechnol.* **2005**, *16*, 1454-1463.

[86] Z. H. Jing, S. H. Wu, *Mater. Lett.* **2004**, *58*, 3637-3640.

[87] Y. H. Zheng, Y. Cheng, Y. S. Wang, F. Bao, *J. Cryst. Growth* **2005**, *284*, 221-225.

[88] M. M. Rahman, J.-Z. Wang, X.-L. Deng, Y. Li, H.-K. Liu, *Electrochim. Acta* **2009**, *55*, 504-510.

[89] X. L. Jiao, D. R. Chen, L. H. Xiao, *J. Cryst. Growth* **2003**, *258*, 158-162.

[90] J. Yang, C. Lin, Z. Wang, J. Lin, *Inorg. Chem.* **2006**, *45*, 8973-8979.

[91] Y. P. Sun, H. W. Rollins, *Chem. Phys. Lett.* **1998**, *288*, 585-588.

[92] Y. P. Sun, R. Guduru, F. Lin, T. Whiteside, *Ind. Eng. Chem. Res.* **2000**, *39*, 4663-4669.

[93] J. L. Zhang, B. X. Han, J. C. Liu, X. G. Zhang, Z. M. Liu, J. He, *Chem. Commun.* **2001**, 2724-2725.

[94] J. X. Yao, G. L. Zhao, D. Wang, G. R. Han, *Mater. Lett.* **2005**, *59*, 3652-3655.

[95] S. S. Swamy, J. M. Calderon-Moreno, M. Yoshimura, *J. Mater. Res.* **2002**, *17*, 734-737.

[96] D. C. Lee, F. V. Mikulec, B. A. Korgel, *J. Am. Chem. Soc.* **2004**, *126*, 4951-4957.

[97] J. Y. Chang, A. Ghule, J. J. Chang, S. H. Tzing, Y. C. Ling, *Chem. Phys. Lett.* **2002**, *363*, 583-590.

[98] J. H. Wu, S. Yin, Y. Lin, J. M. Lin, M. L. Huang, T. Sato, *J. Mater. Sci.* **2001**, *36*, 3055-3059.

[99] K. Byrappa, M. H. Sunitha, A. K. Subramani, S. Ananda, K. M. L. Rai, B. Basavalingu, M. Yoshimura, *J. Mater. Sci.* **2006**, *41*, 1369-1375.

[100] Y. Ding, P. X. Gao, Z. L. Wang, *J. Am. Chem. Soc.* **2004**, *126*, 2066-2072.

[101] D. Li, Y. H. Leung, A. B. Djurisic, Z. T. Liu, M. H. Xie, S. L. Shi, S. J. Xu, W. K. Chan, *Appl. Phys. Lett.* **2004**, *85*, 1601-1603.

[102] W. D. Yu, X. M. Li, X. D. Gao, *Appl. Phys. Lett.* **2004**, *84*, 2658-2660.

[103] J. H. Park, H. J. Choi, Y. J. Choi, S. H. Sohn, J. G. Park, *J. Mater. Chem.* **2004**, *14*, 35-36.

[104] Z. W. Pan, Z. R. Dai, Z. L. Wang, *Science* **2001**, *291*, 1947-1949.

[105] X. Y. Kong, Y. Ding, R. Yang, Z. L. Wang, *Science* **2004**, *303*, 1348-1351.

[106] W. L. Hughes, Z. L. Wang, *J. Am. Chem. Soc.* **2004**, *126*, 6703-6709.

[107] D. Ehrentraut, H. Sato, Y. Kagamitani, H. Sato, A. Yoshikawa, T. Fukuda, *Prog. Cryst. Growth Charact. Mater.* **2006**, *52*, 280-335.

[108] H. Zhang, D. R. Yang, D. S. Li, X. Y. Ma, S. Z. Li, D. L. Que, *Cryst. Growth Des.* **2005**, *5*, 547-550.

[109] A. P. de Moura, R. C. Lima, M. L. Moreira, D. P. Volanti, J. W. M. Espinosa, M. O. Orlandi, P. S. Pizani, J. A. Varela, E. Longo, *Solid State Ionics* **2010**, *181*, 775-780.

[110] V. Polshettiwar, M. N. Nadagouda, R. S. Varma, *Aust. J. Chem.* **2009**, *62*, 16-26.

[111] S. Komarneni, H. Katsuki, *Pure Appl. Chem.* **2002**, *74*, 1537-1543.

[112] Z. Chen, D. Li, G. Xiao, Y. He, Y. J. Xu, *J. Solid State Chem.* **2012**, *186*, 247-254.

[113] C. Yang, X. T. Su, F. Xiao, J. K. Jian, J. D. Wang, *Sens. Actuators B* **2011**, *158*, 299-303.

[114] X. H. Jia, H. Q. Fan, W. W. Yang, *J. Dispersion Sci. Technol.* **2010**, *31*, 866.

[115] Z. H. Ai, K. J. Deng, Q. F. Wan, L. Z. Zhang, S. Lee, *J. Phys. Chem. C* **2010**, *114*, 6237-6242.

[116] X. L. Hu, J. C. Yu, J. M. Gong, Q. Li, G. S. Li, *Adv. Mater.* **2007**, *19*, 2324-2329.

[117] R. G. Deshmukh, S. S. Badadhe, I. S. Mulla, *Mater. Res. Bull.* **2009**, *44*, 1179-1182.

[118] C. Sun, X. T. Su, F. Xiao, C. E. Niu, J. D. Wang, *Sens. Actuators B* **2011**, *157*, 681-685.

[119] Y. N. Li, X. T. Su, J. K. Jian, J. D. Wang, *Ceram. Int.* **2010**, *36*, 1917.

[120] M. Chen, Z. H. Wang, D. M. Han, F. B. Gu, G. S. Guo, *J. Phys. Chem. C* **2011**, *115*, 12763.

[121] T. Krishnakumar, R. Jayaprakash, D. S. Raj, N. Pinna, V. N. Singh, A. R. Phani, G. Neri, *J. Nanopart. Res.* **2011**, *13*, 3327.

[122] P. Rai, H. M. Song, Y. S. Kim, M. K. Song, P. R. Oh, J. M. Yoon, Y. T. Yu, *Mater. Lett.* **2012**, *68*, 90-93.

[123] N. F. Hamedani, A. R. Mahjoub, A. A. Khodadadi, Y. Mortazavi, *Sens. Actuators B* **2011**, *156*, 737-742.

[124] P. Zhu, J. Zhang, Z. Wu, Z. Zhang, *Cryst. Growth Des.* **2008**, *8*, 3148-3153.

[125] Y. Zhou, N. Pienack, W. Bensch, G. R. Patzke, *Small* **2009**, *5*, 1978-1983.

[126] Y. Zhou, J.-D. Grunwaldt, F. Krumeich, K. Zheng, G. Chen, J. Stoetzel, R. Frahm, G. R. Patzke, *Small* **2010**, *6*, 1173-1179.

[127] Y. Zhou, E. Antonova, W. Bensch, G. R. Patzke, *Nanoscale* **2010**, *2*, 2412-2417.

[128] E. Matijevic, *Chemical Processing of Advanced Materials*, (Eds.: L. L. Hench, J. K. West), John Wiley & Sons, New York, **1992**, p. 513.

[129] G. R. Patzke, A. Michailovski, F. Krumeich, R. Nesper, J. D. Grunwaldt, A. Baiker, *Chem. Mater.* **2004**, *16*, 1126-1134.

[130] Y. Zhou, G. R. Patzke, *CrystEngComm* **2012**, *14*, 1161-1163.

[131] Y. P. Fang, A. W. Xu, R. Q. Song, H. X. Zhang, L. P. You, J. C. Yu, H. Q. Liu, *J. Am. Chem. Soc.* **2003**, *125*, 16025-16034.

[132] L. M. Liz Marzan, *J. Mater. Chem.* **2006**, *16*, 3891-3892.

[133] J. Liu, A. Kim, L. Q. Wang, B. J. Palmer, Y. L. Chen, P. Bruinsma, B. C. Bunker, G. J. Exarhos, G. L. Graff, P. C. Rieke, G. E. Fryxell, J. W. Virden, B. J. Tarasevich, L. A. Chick, *Adv. Colloid Interface Sci.* **1996**, *69*, 131-180.

[134] G. A. Ozin, *Adv. Mater.* **1992**, *4*, 612-649.

[135] A. Michailovski, G. R. Patzke, *Z. Anorg. Allg. Chem.* **2007**, *633*, 54-62.

[136] A. Michailovski, R. Kiebach, W. Bensch, J.-D. Grunwaldt, A. Baiker, S. Komarneni, G. R. Patzke, *Chem. Mater.* **2007**, *19*, 185-197.

[137] Y. Zhou, K. Zheng, J.-D. Grunwaldt, T. Fox, L. Gu, X. Mo, G. Chen, G. R. Patzke, *J. Phys. Chem. C* **2011**, *115*, 1134-1142.

[138] R. Kiebach, N. Pienack, W. Bensch, J.-D. Grunwaldt, A. Michailovski, A. Baiker, T. Fox, Y. Zhou, G. R. Patzke, *Chem. Mater.* **2008**, *20*, 3022-3033.

[139] T. A. Xia, Q. Li, X. D. Liu, J. A. Meng, X. Q. Cao, *J. Phys. Chem. B* **2006**, *110*, 2006-2012.

[140] C. V. Krishnan, J. Chen, C. Burger, B. Chu, *J. Phys. Chem. B* **2006**, *110*, 20182-20188.

[141] L. Fang, Y. Y. Shu, A. Q. Wang, T. Zhang, *J. Cryst. Growth* **2008**, *310*, 4593-4600.

[142] H. Uchiyama, H. Ohgi, H. Imai, *Cryst. Growth Des.* **2006**, *6*, 2186-2190.

[143] D. Grigoriev, R. Miller, D. Shchukin, H. Moehwald, *Small* **2007**, *3*, 665-671.

[144] X. W. Lou, H. C. Zeng, *Inorg. Chem.* **2003**, *42*, 6169-6171.

[145] Y. Zhou, K. Vuille, A. Heel, G. R. Patzke, *Z. Anorg. Allg. Chem.* **2009**, *635*, 1848-1855.

[146] T. J. Trentler, T. E. Denler, J. F. Bertone, A. Agrawal, V. L. Colvin, *J. Am. Chem. Soc.* **1999**, *121*, 1613-1614.

[147] M. Green, P. O'Brien, *Chem. Commun.* **2000**, 183-184.

[148] J. Rockenberger, E. C. Scher, A. P. Alivisatos, *J. Am. Chem. Soc.* **1999**, *121*, 11595-11596.

[149] S. Thimmaiah, M. Rajamathi, N. Singh, P. Bera, F. Meldrum, N. Chandrasekhar, R. Seshadri, *J. Mater. Chem.* **2001**, *11*, 3215-3221.

[150] Y. D. Li, Y. Ding, Y. T. Qian, Y. Zhang, L. Yang, *Inorg. Chem.* **1998**, *37*, 2844-2845.

[151] J. H. Zhan, X. G. Yang, W. X. Zhang, D. W. Wang, Y. Xie, Y. T. Qian, *J. Mater. Res.* **2000**, *15*, 629-632.

[152] W. Z. Wang, P. Yan, F. Y. Liu, Y. Xie, Y. Geng, Y. T. Qian, *J. Mater. Chem.* **1998**, *8*, 2321-2322.

[153] J. P. Xiao, Y. Xie, Y. J. Xiong, R. Tang, Y. T. Qian, *J. Mater. Chem.* **2001**, *11*, 1417-1420.

[154] M. Inoue, M. Kimura, T. Inui, *Chem. Commun.* **1999**, 957-958.

[155] C. B. Murray, D. J. Norris, M. G. Bawendi, *J. Am. Chem. Soc.* **1993**, *115*, 8706-8715.

[156] K. Sardar, R. I. Walton, *J. Solid State Chem.* **2012**, *189*, 32-37.

[157] L. Xie, J. Ma, P. Wu, H. Tian, Z. Zhao, J. Zhou, Y. Hu, Y. Wang, J. Tao, X. Zhu, *Mater. Res. Bull.* **2007**, *42*, 389.

[158] X. Zhu, J. Zhang, F. Chen, *Chemosphere* **2010**, *78*, 1350.

[159] X. Y. Liu, J. H. Zeng, S. Y. Zhang, R. B. Zheng, X. M. Liu, Y. T. Qian, *Chem. Phys. Lett.* **2003**, *374*, 348.

[160] A. Michailovski, F. Krumeich, G. R. Patzke, *Helv. Chim. Acta* **2004**, *87*, 1029.

[161] P. T. Moseley, B. C. Totfield, *Solid state gas sensors*, Adam Hilger, Philadelphia, **1987**. pp.71-123.

[162] M. J. Madou, S. R. Morrison, *Chemical Sensing with Solid State Devices*, Academic Press, San Diego, **1989**.

[163] G. Sberveglieri, *Gas Sensors*, Dordrecht, **1992**.

[164] N. Taguchi, U.S. Patent. 3,631,436, **1971**.

[165] K. Ihokura, J. Watson, *Stannic Oxide Gas Sensors, Principles and Applications*, CRC, Boca Raton, **1994**.

[166] N. Barsan, U. Weimar, *J. Electroceram.* **2001**, *7*, 143-167.

[167] N. Barsan, U. Weimar, *J. Phys: Condens. Matter* **2003**, *15*, R813-R839.

[168] A. Gurlo, N Barsan, U. Weimar, *Gas sensors based on semiconducting metal oxides, in Metal Oxides: Chemistry and Applications*, (Eds.: J. L. G. Fierro) CRC Press, Boca Raton, **2006**, 683-738.

[169] S. Ahlers, G. Muller, T. Doll, *Sens. Actuators B* **2005**, *107*, 587-599.

[170] C. O. Park, S. A. Akbar, *J. Mater. Sci.* **2003**, *38*, 4611-4637.

[171] G. Eranna, B. C. Joshi, D. P. Runthala, R. P. Gupta, *Crit. Rev. Solid State Mat. Sci.* **2004**, *29*, 111-188.

[172] G. Korotcenkov, *Sens. Actuators B* **2005**, *107*, 209-232.

[173] M. E. Franke, T. J. Koplin, U. Simon, *Small* **2006**, *2*, 36-50.

[174] M. Batzill, U. Diebold, *Prog. Surface Sci.* **2005**, *79*, 47-154.

[175] A. Gurlo, *ChemPhysChem* **2006**, *7*, 2041-2052.

[176] K. Hauffe, *Adv. Catal.* **1955**, *7*, 213-257.

[177] K. Hauffe, *Angew. Chem. Int. Ed.* **1955**, *67*, 189-207.

[178] K. Hauffe, S. R. Morrison, *Eine Einführung in die Probleme der Adsorption*, de Gruyter Berlin, **1973**.

[179] A. Gurlo, R. Riedel, *Angew. Chem. Int. Ed.* **2007**, *46*, 3826-3848.

[180] M. J. Madou, S. R. Morrison, *Chemical Sensing with Solid State Devices*, Academic Press, San Diego, **1989**.

[181] S. R. Morrison, *The Chemical Physics of Surfaces*, New York, **1977**.

[182] P. Serrini, V. Briois, M. C. Horrillo, A. Traverse, L. Manes, *Thin Solid Films* **1997**, *304*, 113-122.

[183] D. Briggs, M. P. Seah, *Practical Surface Analysis. Auger and X-ray Photoelectron Spectroscopy*, Wiley Chichester, **1990**. 501.

[184] N. Yamazoe, J. Fuchigami, M. Kishikawa, T. Seiyama, *Surface Sci.* **1979**, *86*, 335-344.

[185] S. C. Chang, *J. Vac. Sci. Technol.* **1980**, *17*, 366-369.

[186] F. Morazzoni, C. Canevali, N. Chiodini, C. Mari, R. Ruffo, R. Scotti, L. Armelao, E. Tondello, L. E. Depero, E. Bontempi, *Chem. Mater.* **2001**, *13*, 4355-4361.

[187] L. Armelao, D. Barreca, E. Bontempi, C. Canevali, L. E. Depero, C. M. Mari, R. Ruff, R. Scotti, E. Tondello, F. Morazzoni, *Appl. Magn. Reson.* **2002**, *22*, 89-100.

[188] T. A. Gundrizer, A. A. Davydov, *React. Kinet. Catal. Lett.* **1975**, *3*, 63-70.

[189] M. J. Madou, S. R. Morrison, *Chemical Sensing with Solid State Devices*, Academic Press, San Diego, **1989**.

[190] G. Jimenez-Cadena, J. Riu, F. X. Rius, *Anal.* **2007**, *132*, 1083-1099.

[191] A. Kolmakov, M. Moskovits, *Ann. Rev. Mater. Res.* **2004**, *34*, 151-180.

[192] N. Yamazoe, G. Sakai, K. Shimanoe, *Catal. Surv. Asia* **2003**, *7*, 63-75.

[193] G. Korotcenkov, *Mater. Sci. Eng. B: Solid State Mater. Adv. Technol.* **2007**, *139*, 1-23.

[194] M. M. Arafat, B. Dinan, S. A. Akbar, A. S. M. A. Haseeb, *Sensors* **2012**, *12*,7207-7258.

[195] L. Wang, Z. Lou, T. Fei, T. Zhang, *J. Mater. Chem.* **2011**, *21*, 19331-19336.

[196] G. S. Devi, V. B. Subrahmanyam, S. C. Gadkari, S. K. Gupta, *Anal. Chim. Acta* **2006**, *568*, 41-46.

[197] C. S. Prajapati, S. N. Pandey, P. P. Sahay, *J. Phys B: Condens. Matter* **2011**, *406*, 2684-2688.

[198] P. S. Shewale, A. V. Moholkar, J. H. Kim, M. D. Uplane, *J. Alloys Compd.* **2012**, *541*, 244-249.

[199] Y. Cao, X. L. Hu, D. W. Wang, Y. F. Sun, P. Sun, J. Zheng, J. Ma, G. Y. Lu, *Mater. Lett.* **2012**, *69*, 45-47.

[200] N. Han, X. F. Wu, L. Y. Chai, H. D. Liu, Y. F. Chen, *Sens. Actuators B* **2010**, *150*, 230-238.

[201] E. Comini, G. Faglia, G. Sberveglieri, Z. W. Pan, Z. L. Wang, *Appl. Phys. Lett.* **2002**, *81*, 1869-1871.

[202] V. A. Chaudhary, I. S. Mulla, K. Vijayamohanan, *Sens. Actuators B* **1999**, *55*, 154-160.

[203] Z. N. Tang, G. P. Jiang, P. C. H. Chan, J. K. O. Sin, S. S. Lau, *Sens. Actuators B* **1997**, *43*, 161-164.

[204] Y. Komem, G. Ankonina, A. Rothschild, J. S. Im, U. J. Chung, *Phys. Scr.* **2007**, *T129*, 157-159.

[205] G. K. Mor, O. K. Varghese, M. Paulose, K. G. Ong, C. A. Grimes, *Thin Solid Films* **2006**, *496*, 42-48.

[206] A. Serra, E. Filippo, A. Buccolieri, M. Di Giulio, D. Manno, *Sens. Actuators B* **2009**, *140*, 563-567.

[207] N. O. Savage, S. A. Akbar, P. K. Dutta, *Sens. Actuators B* **2001**, *72*, 239-248.

[208] K. K. Makhija, A. Ray, R. M. Patel, U. B. Trivedi, H. N. Kapse, *Bull. Mat. Sci.* **2005**, *28*, 9-17.

[209] S. Bianchi, E. Comini, M. Ferroni, G. Faglia, A. Vomiero, G. Sberveglieri, *Sens. Actuators B* **2006**, *118*, 204-207.

[210] Z. Chen, D. Li, G. Xiao, Y. He, Y.-J. Xu, *J. Solid State Chem.* **2012**, *186*, 247-254.

[211] C. B. Xu, A. S. Teja, *J. Supercrit. Fluids* **2006**, *39*, 135-141.

[212] I. M. Szilagyi, L. Wang, P. I. Gouma, C. Balaszsi, J. Madarasz, G. Pokol, *Mater. Res. Bull.* **2009**, *44*, 505-508.

[213] G. Wang, Y. Ji, X. Huang, X. Yang, P.-I. Gouma, M. Dudley, *J. Phys. Chem. B* **2006**, *110*, 23777-23782.

[214] A. Ponzoni, E. Comini, G. Sberveglieri, J. Zhou, S. Z. Deng, N. S. Xu, Y. Ding, Z. L. Wang, *Appl. Phys. Lett.* **2006**, *88*.

[215] R. B. Waghulade, P. P. Patil, R. Pasricha, *Talanta* **2007**, *72*, 594-599.

[216] D. S. Raj, T. Krishnakumar, R. Jayaprakash, T. Prakash, G. Leonardi, G. Neri, *Sens. Actuators B* **2012**, *171*, 853-859.

[217] A. S. Kamble, R. C. Pawar, J. Y. Patil, S. S. Suryavanshi, P. S. Patil, *J. Alloys Compd.* **2011**, *509*, 1035-1039.

[218] M. B. Rahmani, S. H. Keshmiri, J. Yu, A. Z. Sadek, L. Al-Mashat, A. Moafi, K. Latham, Y. X. Li, W. Wlodarski, K. Kalantar-zadeh, *Sens. Actuators B* **2010**, *145*, 13-19.

[219] A. M. Taurino, A. Forleo, L. Francioso, P. Siciliano, M. Stalder, R. Nesper, *Appl. Phys. Lett.* **2006**, *88*.

[220] W. S. Kim, H. C. Kim, S. H. Hong, *J. Nanopart. Res.* **2010**, *12*, 1889-1896.

[221] E. Comini, L. Yubao, Y. Brando, G. Sberveglieri, *Chem. Phys. Lett.* **2005**, *407*, 368-371.

[222] A. K. Prasad, P. I. Gouma, D. J. Kubinski, J. H. Visser, R. E. Soltis, P. J. Schmitz, *Thin Solid Films* **2003**, *436*, 46-51.

[223] D. Chen, M. Liu, L. Yin, T. Li, Z. Yang, X. Li, B. Fan, H. Wang, R. Zhang, Z. Li, H. Xu, H. Lu, D. Yang, J. Sun, L. Gao, *J. Mater. Chem.* **2011**, *21*, 9332-9342.

[224] A. Labidi, A. Bejaoui, H. Ouali, F. C. Akkari, A. Hajjaji, M. Gaidi, M. Kanzari, B. Bessais, M. Maaref, *Appl. Surf. Sci.* **2011**, *257*, 9941-9945.
[225] A. Dutta, D. Das, M. L. Grilli, E. Di Bartolomeo, E. Traversa, D. Chakravorty, *J. Sol-Gel Sci. Technol.* **2003**, *26*, 1085-1089.
[226] A. M. Soleimanpour, S. V. Khare, A. H. Jayatissa, *ACS Appl. Mater. Interfaces* **2012**, *4*, 4651-4657.
[227] P. Wu, J. H. Sun, Y. Y. Huang, G. F. Cu, D. G. Tong, *Mater. Lett.* **2012**, *82*, 191-194.
[228] T. Siciliano, M. Di Giulio, M. Tepore, E. Filippo, G. Micocci, A. Tepore, *Sens. Actuators B* **2009**, *138*, 550-555.
[229] D. Tsiulyanu, A. Tsiulyanu, H. D. Liess, I. Eisele, *Thin Solid Films* **2005**, *485*, 252-256.
[230] D. Tsiulyanu, S. Marian, H. D. Liess, *Sens. Actuators B* **2002**, *85*, 232-238.
[231] G. Korotcenkov, *Mater. Sci. Eng.* **2008**, *61*, 1-39.
[232] P. M. Faia, C. S. Furtado, A. J. Ferreira, *Sens. Actuators B* **2004**, *101*, 183-190.
[233] P. G. Su, C. Y. Chen, *Sens. Actuators B* **2008**, *129*, 380-385.
[234] Y. Zhang, X. J. Zheng, T. Zhang, L. J. Gong, S. H. Dai, Y. Q. Chen, *Sens. Actuators B* **2010**, *147*, 180-184.
[235] X. Zhang, S. A. McGill, P. Xiong, *J. Am. Chem. Soc.* **2007**, *129*, 14470-14474.
[236] N. Yamazoe, Y. Shimizu, *Sens. Actuators* **1986**, *10*, 379-398.
[237] Z. M. Rittersma, *Sens. Actuators B* **2002**, *96*, 196-210.
[238] G. Scholz, *Techn. Mess.* **1992**, *59*, 88-109.
[239] J.P. Lafarie, *Relative humidity measurement: a review of state-of-the-art sensors, in: Proceedings of the Conference on Humidity and Moisture*, Washington DC, **1985**. pp. 875-889.
[240] B. M. Kulwicki, *J. Am. Ceram. Soc.* **1991**, *74*, 697-708.
[241] R. S. Jachowicz, S. D. Senturia, *Sens. Actuators* **1981**, *2*, 171-186.
[242] D. Roveti, K. Soleyn, *Meas. Control* **1999**, 105-110.
[243] Q. Y. Tang, Y. C. Chan, K. L. Zhang, *Sens. Actuators B* **2011**, *152*, 99-106.
[244] Y. Li, M. J. Yang, *Sens. Actuators B* **2002**, *85*, 73-78.
[245] X. Lv, L. J. Hong, Y. Li, M. J. Yang, *J. Appl. Polym. Sci.* **2009**, *112*, 1287-1293.
[246] Y. Li, M. J. Yang, G. Casalbore-Miceli, N. Camaioni, *Synth. Met.* **2002**, *128*, 293-298.
[247] V. K. Khanna, R. K. Nahar, *J. Phys: D: Appl. Phys.* **1986**, *19*, L141-L145.
[248] E. Traversa, *Sens. Actuators B* **1995**, *23*, 135-156.
[249] R. M. Oliveira, M. C. A. Nono, C. Kuranaga, M. Wada, *Advanced Powder Technology V*, *Vol. 530-531* (Eds.: L. Salgado, F. A. Filho), Trans Tech Publications Ltd, Stafa-Zurich, **2006**, pp. 414-419.
[250] H. Y. He, X. Liu, *J. Ceram. Process. Res.* **2010**, *11*, 154-157.
[251] R. Sundaram, K. S. Nagaraja, *Sens. Actuators B* **2004**, *101*, 353-360.

[252] Q. C. Liang, H. L. Xu, J. X. Zhao, S. Gao, *Sens. Actuators B* **2012**, *165*, 76-81.

[253] J. M. Tulliani, V. Naglieri, C. Baroni, *Humidity Sensors Based on Nanocrystalline Iron Oxides*, **2009**.

[254] C. Y. Lee, G. B. Lee, *Sensor Lett.* **2005**, *3*, 1-15.

[255] F. Hernandez-Ramirez, S. Barth, A. Tarancon, O. Casals, E. Pellicer, J. Rodriguez, A. Romano-Rodriguez, J. R. Morante, S. Mathur, *Nanotechnol.* **2007**, *18*.

[256] Y. F. Qiu, S. H. Yang, *Adv. Funct. Mater.* **2007**, *17*, 1345-1352.

[257] Z. Chen, C. Lu, *Sens. Lett.* **2005**, *3*, 274-295.

[258] C. N. Xu, K. Miyazaki, T. Watanabe, *Sens. Actuators B* **1998**, *46*, 87-96.

[259] Y. Zhang, W. Fu, H. Yang, M. Li, Y. Li, W. Zhao, P. Sun, M. Yuan, D. Ma, B. Liu, G. Zou, *Sens. Actuators B* **2008**, *135*, 317-321.

[260] Z. Zhou, C. Zhan, Y. Wang, Y. Su, Z. Yang, Y. Zhang, *Mater. Lett.* **2011**, *65*, 832-835.

[261] M. Parthibavarman, V. Hariharan, C. Sekar, *Mater. Sci. Eng. C: Mater Biol. Appl.* **2011**, *31*, 840-844.

[262] Y. F. Dong, L. Y. Li, W. F. Jiang, H. Y. Wang, X. J. Li, *Phys. E* **2009**, *41*, 711-714.

[263] S. Pokhrel, K. S. Nagaraja, *Trans. Indian Inst. Met.* **2003**, *56*, 351-355.

[264] H. T. Hsueh, T. J. Hsueh, S. J. Chang, F. Y. Hung, T. Y. Tsai, W. Y. Weng, C. L. Hsu, B. T. Dai, *Sens. Actuators B* **2011**, *156*, 906-911.

[265] J. Kleperis, M. Kundzins, G. Vitins, V. Eglitis, G. Vaivars, A. Lusis, *Sens. Actuators B* **1995**, *28*, 135-138.

[266] X. W. Liu, R. Wang, T. Zhang, Y. A. He, J. C. Tu, X. T. Li, *Sens. Actuators B* **2010**, *150*, 442-448.

[267] Y. Zhang, W. Fu, H. Yang, M. Li, Y. Li, W. Zhao, P. Sun, M. Yuan, D. Ma, B. Liu, G. Zou, *Sens. Actuators B* **2008**, *135*, 317-321.

[268] Y. He, T. Zhang, W. Zheng, R. Wang, X. W. Liu, Y. Xia, J. W. Zhao, *Sens. Actuators B* **2010**, *146*, 98-102.

[269] L. You, Y. Cao, Y. F. Sun, P. Sun, T. Zhang, Y. Du, G. Y. Lu, *Sens. Actuators B* **2012**, *161*, 799-804.

[270] Z. Wang, L. Shi, F. Wu, S. Yuan, Y. Zhao, M. Zhang, *Sens. Actuators B* **2011**, *158*, 89-96.

[271] W. S. Wang, A. V. Virkar, *Sens. Actuators B* **2004**, *98*, 282-290.

[272] R. Sundaram, E. S. Raj, K. S. Nagaraja, *Sens. Actuators B* **2004**, *99*, 350-354.

[273] M. Zhang, C. G. Hu, H. Liu, Y. F. Xiong, Z. W. Zhang, *Sens. Actuators B* **2009**, *136*, 128-132.

[274] Y. Zhang, X. J. Zheng, T. Zhang, L. J. Gong, S. H. Dai, Y. Q. Chen, *Sens. Actuators B* **2010**, *147*, 180-184.

[275] A. Raj, C. M. Magdalane, K. S. Nagaraja, *Phys. Status Solidi A* **2002**, *191*, 230-234.

[276] T. Nitta, Z. Terada, S. Hayakawa, *J. Am. Ceram. Soc.* **1980**, *63*, 295-300.

[277] K. Katazama and T. Akiba, *Rutil humidity sensor, Proc. Int. Meet. On Chemical Sensors*, Proc. Int. Meet. On Chemical Sensors, Kodansha, **1983**. 433-438.

[278] T. Suzuki and N. Matsui, *Properties of humidity sensitive oxides with alkali additive, Proc. Int. Meet. On Chemical Sensors*, Kodansha, **1983**. 381-386.

[279] Y. Yokomizo, S. Uno, M. Harata, H. Hiraki, K. Yuki, *Sens. Actuators* **1983**, *4*, 599-606.

[280] S. Uno, M Harata, H. Hiraki, K. Sakuma and Y. Yokomizo, *$ZnCr_2O_4$-$LiZnVO_4$ ceramic humidity sensor, Proc. Int. Meet. On Chemical sensors,* Kodansha, **1983**. 375-380.

[281] McCaffer.E, Zettlemo.Ac, *Discuss. Faraday Soc.* **1971**, 239.

[282] M. Nagao, T. Morimoto, *J. Phys. Chem.* **1969**, *73*, 3809.

[283] M. Egashira, S. Kawasumi, S. Kagawa, T. Seiyama, *Bull. Chem. Soc. Jpn.* **1978**, *51*, 3144-3149.

[284] M. Egashira, M. Nakashima, S. Kawasumi, T. Seiyama, *J. Phys. Chem.* **1981**, *85*, 4125-4130.

[285] O. K. Varghese, C. A. Grimes, *J. Nanosci. Nanotechnol.* **2003**, *3*, 277-293.

[286] L. Gu, K. Zheng, Y. Zhou, J. Li, X. Mo, G. R. Patzke, G. Chen, *Sens. Actuators B* **2011**, *159*, 1-7.

[287] M. Kaelin, D. Rudmann, A. N. Tiwari, *Sol. Energy* **2004**, 77, 749-756.

[288] K. Zheng, Y. Zhou, L. Gu, X. Mo, G. R. Patzke, G. Chen, *Sens. Actuators B* **2010**, *148*, 240-246.

[289] D. Chen, M. Liu, L. Yin, T. Li, Z. Yang, X. Li, B. Fan, H. Wang, R. Zhang, Z. Li, H. Xu, H. Lu, D. Yang, J. Sun, L. Gao, *J. Mater. Chem.* **2011**, *21*, 9332.

[290] A. K. Prasad, D. J. Kubinski, P. I. Gouma, *Sens. Actuators B* **2003**, *93*, 25.

[291] X. Chu, S. Liang, W. Sun, W. Zhang, T. Chen, Q. Zhang, *Sens. Actuators B* **2010**, *148*, 399.

[292] H. J. Lunk, H. Hartl, M. A. Hartl, M. J. G. Fait, I. G. Shenderovich, M. Feist, T. A. Frisk, L. L. Daemen, D. Mauder, R. Eckelt, A. A. Gurinov, *Inorg. Chem.* **2010**, *49*, 9400.

[293] B. Krebs, I. Paulat-Boschen, *Acta Cryst.* **1976**, B32, 1697–1704.

Part I

Bismuth-based Materials for Humidity Sensing Applications

2. Room temperature synthesis and humidity sensing properties of $Bi_2O_2CO_3$ nanosheets

2.1 Introduction

Humidity is a very important environmental parameter to monitor and control due to its key role in industrial processes and daily life.[1,2] A wide range of sensing materials, such as polymers,[3] ceramics,[4] hybrid polymer/inorganic systems[5] and metal oxide semiconductors[6] have been investigated as humidity sensors. Among these materials, metal oxide semiconductors are highly promising candidates for humidity sensing applications. They can be easily obtained through environmentally friendly synthesis routes and low-cost starting materials.[7-10] Furthermore, the large family of oxides offers almost endless compositions, morphologies and structural properties.[11,12] The outstanding water adsorption and desorption abilities of oxide surfaces give rise to their potential as sensing materials in various applied areas.[13] The working principle of humidity sensors is based on detecting changes in electrical properties, such as capacitance and resistance, under different relative humidity conditions. Recently, we have reported that ternary bismuth-containing oxides such as *Aurivillius* type Bi_2MO_6 (M = W, Mo)[14] and sillenite-type cubic bismuth phosphate[15] exhibit promising humidity sensing performance over a broad relative humidity range (11 – 95 % RH) with high sensitivity, quick response/recovery time and linear response with relative humidity. Furthermore, one-dimensional $Bi_6S_2O_{15}$ nanowires has been investigated as novel humidity sensor with high performance.[16] This renders other types of bismuth-containing oxides interesting candidates for humidity sensing applications.

Sillenite-type type $Bi_2O_2CO_3$, which consists of alternate $Bi_2O_2^{2+}$ and CO_3^{2-} layers with the plane of the CO_3^{2-} group orthogonal to the plane of the $Bi_2O_2^{2+}$ layer, is of interest due to its structural relationship with the *Aurivillius*-type oxides.[17] Recently, $Bi_2O_2CO_3$ nanotube arrays with antibacterial properties have been reported as useful for healthcare purposes, and they were synthesized via a reflux process.[18] Other research groups have reported on the photocatalytic activity of $Bi_2O_2CO_3$ with various morphologies, including hierarchical flower-like microstructures,[19-22] microspheres,[21] nanosheets,[23] and plate-like morphologies[21,24] by means of different synthesis techniques. However, these conventional syntheses require either organic templates as structure directing agents or further additives as carbon sources.[22,23,25]

Therefore, we developed an environmental-friendly and convenient synthesis approach towards $Bi_2O_2CO_3$.

$Bi_2O_2CO_3$ nanosheets were obtained with an elegant approach starting from commercial Bi_2O_3 at room temperature under atmospheric pressure. Instead of introducing additives, atmospheric CO_2 was used as natural carbon source. Furthermore, we investigated the humidity sensing performance of $Bi_2O_2CO_3$ nanosheets by studying capacitance and impedance changes under different relative humidity conditions. The sensing performance demonstrated high sensitivity, fast response/recovery time and reliable reproducibility of this novel type of humidity sensing material.

Note, that the humidity sensing measurements of $Bi_2O_2CO_3$ nanosheets were designed and performed by the author of this thesis. The synthesis and detailed characterization experiments were executed by collaborators from State Key Laboratory of Oil and Gas Reservoir and Exploitation of Southwest Petroleum University Chengdu China (cf. thesis survey page 56), followed by joint evaluation.

2.2 Experimental section

2.2.1 Synthesis of $Bi_2O_2CO_3$ nanosheets

In a typical synthesis procedure, 200 mg of Bi_2O_3 powders (Aldrich Chemical Co.) were dispersed in 100 mL deionized water and stirred magnetically for 24 h. During the stirring process, the yellow color of Bi_2O_3 precursors changed to white gradually, indicating Bi_2O_3 converted to other phase. After that, the resulting white powders was collected after filtration, washed with distilled water and dried in air.

2.2.2 Analytical characterization

X-ray diffraction (XRD) analysis was conducted on a PANalytical X'pert diffractometer operated at 40 kV and 40 mA. Scanning electron microscopy (SEM) images were obtained using FEI Quanta 450 microscope. Transmission electron microscopy (TEM) and high-resolution transmission electron microscopy (HRTEM) was performed on a Tecnai F 30 ST (FEG, 300 kV, SuperTwin lens). In the scanning TEM (STEM) mode, the electron beam was placed in a selected area and an elemental analysis by EDXS (EDAX detector) was performed there.

2.2.3 Humidity sensor fabrication and measurements

For the fabrication of humidity sensor, 5 mg of $Bi_2O_2CO_3$ was added in 1 mL deionized water to form a paste, which was then coated on a quartz substrate with Au interdigital electrodes (finger distances set to 200 μm). The characteristic curves of humidity sensitivity were measured with a WANYE KERR 4300 LCR analyzer with an applied AC voltage 1 V and frequency 150 Hz, respectively. A rate of 3 s per data was applied to record the resistance and capacitance change. Humidity environments were achieved by using saturated aqueous solutions of different salts (LiCl, $MgCl_2$, $Mg(NO_3)_2$, NaCl, KCl and KNO_3) in a closed glass vessel, corresponding to relative humidity (RH) values of 11 %, 33 %, 55 %, 75 %, 85 % and 95 %. All measurements were carried out at ca. 28 °C. The frequency dependencies of the complex impedance were performed under different RH conditions in the frequency range 0.1 Hz to 1 MHz using an Autolab PGSTAT 302N electrochemical system.

2.3 Results and discussion

2.3.1 Structure and morphology of $Bi_2O_2CO_3$

The XRD pattern of the product prepared in a typical procedure is shown in Figure 2.1. The calculated unit cells of the sample were $\alpha = b = 3.860$ (3) Å, $c = 13.68$ (1) Å, which agree well the data of tetragonal $Bi_2O_2CO_3$ from JCPDS card No. 41-1488. No diffraction peaks of Bi_2O_3 were detected. Nevertheless, several very weak diffraction peaks from $(BiO)_4CO_3(OH)_2$ (JCPDS card No. 38-0579) were also observed, which was probably due to the low CO_2 pressure under oxygen atmosphere.[17] Moreover, the diffraction intensity ratio of the (110) peak to the (013) peak of the obtained $Bi_2O_2CO_3$ is 0.49, which is higher than that of the standard pattern in JCPDS card No. 41-1488 (0.386), indicating the preferred oriented growth along the (110) plane.[19]

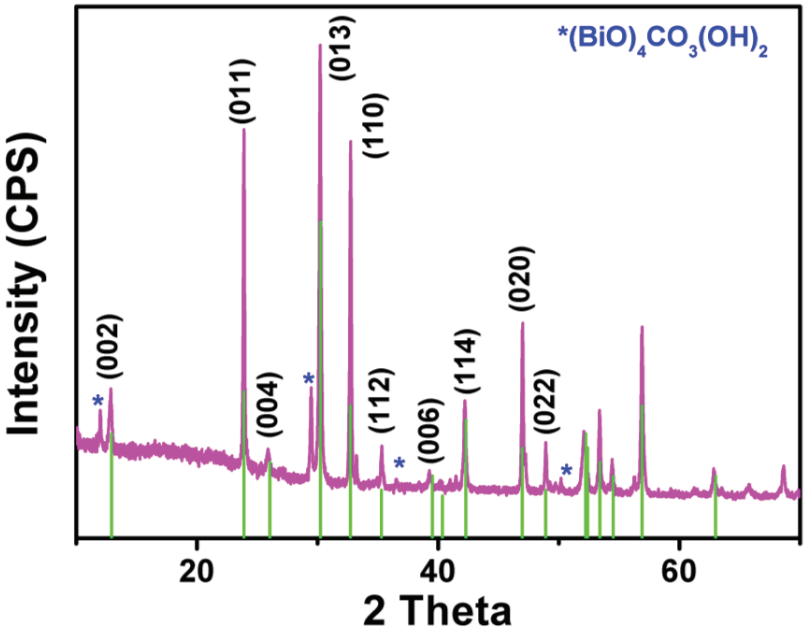

Figure 2.1. XRD patters of the product treated at typical reaction condition. The reference pattern of tetragonal $Bi_2O_2CO_3$ (JCPDS No.41-1488) is shown at the bottom.

Figure 2.2 a and b show the SEM images of the obtained $Bi_2O_2CO_3$. The synthesized $Bi_2O_2CO_3$ are composed of square-like nanosheets, and no other morphologies are observed. In general, the layered structure motif of $Bi_2O_2CO_3$ is a favorable prerequisite for anisotropic growth into 2D morphologies.[26] A more detailed insight into the microstructure of $Bi_2O_2CO_3$ was obtained by TEM investigations. TEM images (Figure 2.2 c) revealed that the particles exhibit square-like nanosheet morphology which agrees well with the SEM images. Moreover, the nanosheets are very thin and relatively transparent to the electron beam. HRTEM images (Figure 2.2 d) showed that the lattice spacing of the nanosheet is 0.270 nm, thus matching well with the spacing of the (110) crystal plane of $Bi_2O_2CO_3$. This indicates that the nanosheets grew long the (110) direction and were exposed with (001) facets. Nevertheless, some granular particles were observed on the surface of $Bi_2O_2CO_3$ nanosheets, pointing to melting of $Bi_2O_2CO_3$ during electron beam irradiation which is often observed for BiO_x-type compounds.[27] EDXS analysis of the nanosheets (cf. Figure 2.3) demonstrated that Bi, C and O are the main components (the Cu peak arises from the supporting Cu grid). No other impurity peaks were detected.

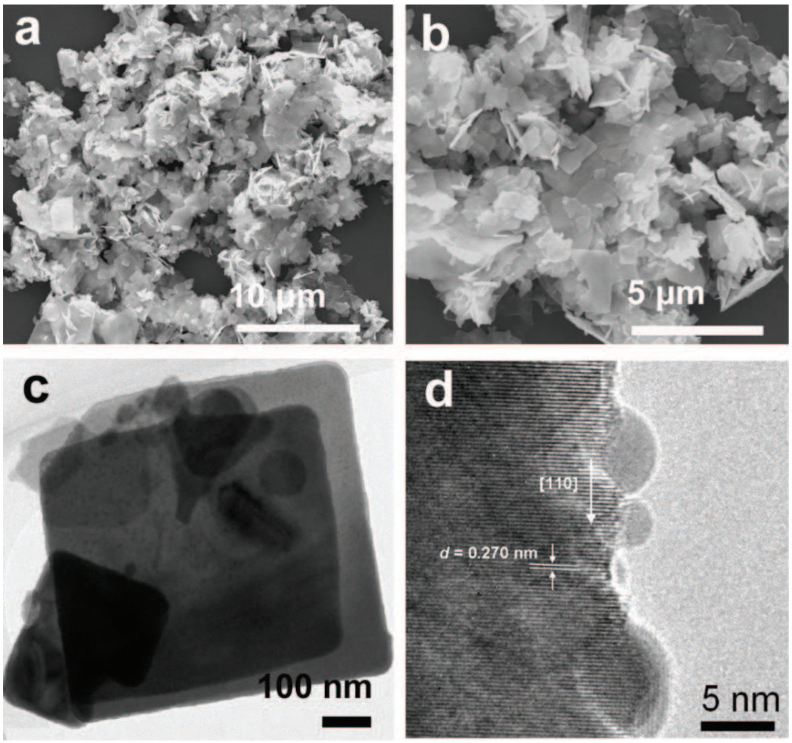

Figure 2.2. (a) and (b) Representative SEM images of $Bi_2O_2CO_3$ at different magnifications; (c) TEM image of $Bi_2O_2CO_3$ particles; (d) HRTEM image of $Bi_2O_2CO_3$ particles.

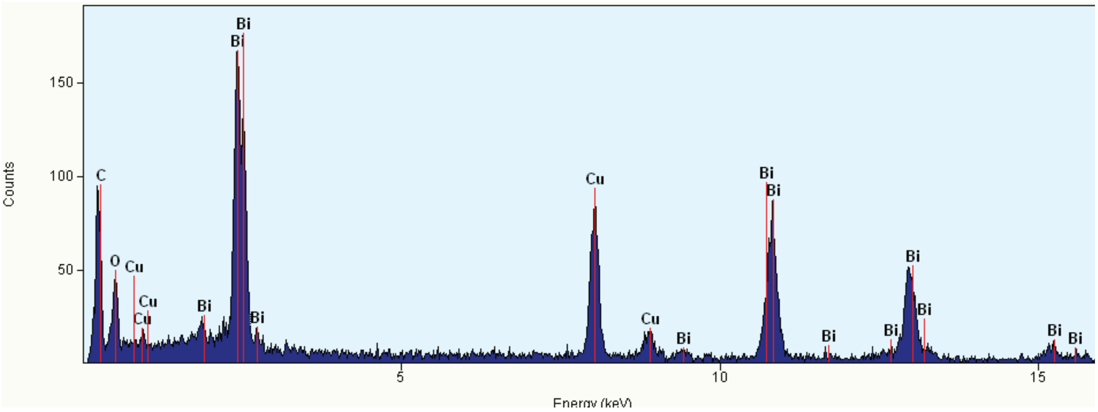

Figure 2.3. EDX spectrum of $Bi_2O_2CO_3$ nanosheets (Cu signals are due to the TEM grids).

2.3.2 Humidity-dependent impedance and capacitance

In general, the characteristics of humidity sensors are strongly related to the applied frequency and AC voltage. According to our previous optimized results,[14,15] the operational AC voltage and frequency in our current work were kept constant at 1 V and 150 Hz, respectively. Figure 2.4 shows the humidity hysteresis characteristics of the fabricated sensors. The impedance changes from about 10^6 kΩ to 10^2 kΩ when the RH increases from 11 % to 95 %, indicating a high sensitivity (over four orders of magnitude). The $Bi_2O_2CO_3$ sensor exhibits a very narrow impedance hysteresis loop with only slight deviations around 85 %, which is better than our previously reported Bi_2WO_6, Bi_2MoO_6 and $BiPO_4$ humidity sensors.[14,15] Moreover, the impedance vs. RH plots can be clearly divided into two different regions of linear response at low RH (11 – 55 %) and high RH (75 – 95 %). This result indicates that two different sensing mechanisms may occur at low and high RH, which will be discussed in the following section (cf. Section 2.3.3). On the other hand, the capacitance of the sensor depends on the permittivity of materials so that the capacitance increases after water adsorption. The capacitance vs. RH plots (cf. Figure 2.5 b) showed that the sensitivity of the sensor is 3 orders of magnitude (10 pF to 10^3 pF) with the RH varying from 11 to 95 %, which is lower than that of humidity-dependent impedance. In addition, the adsorption/desorption behavior based on capacitance measurements is almost consistent in the range from 11 % to 95 % RH, indicting little humidity hysteresis.

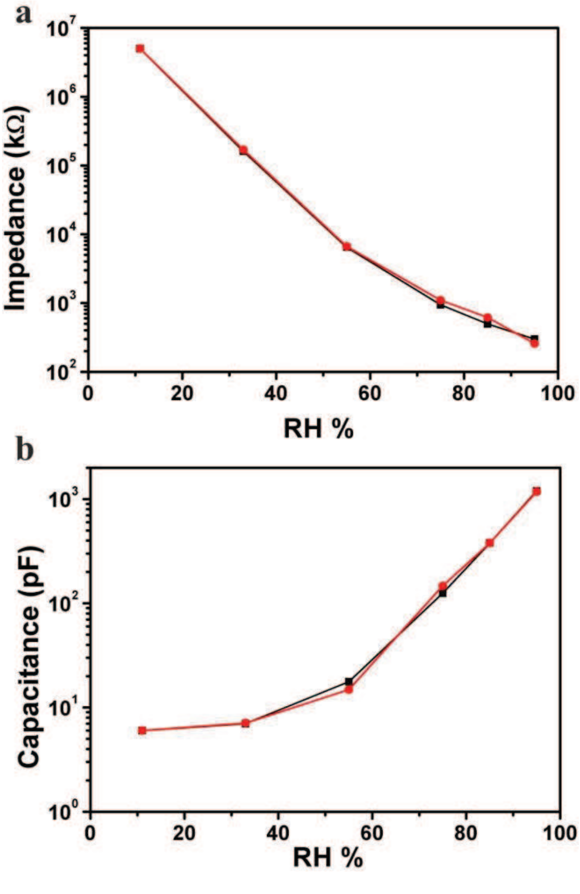

Figure 2.4. Humidity hysteresis characteristic of $Bi_2O_2CO_3$ humidity sensor: (a) humidity-dependent impedance; (b) humidity-dependent capacitance

In order to investigate the time-dependent humidity sensing properties, impedance and capacitance were measured for several response and recovery cycles at selected steps as shown in Figure 2.5. Each cycle was measured over 20 min in a constant humidity environment.

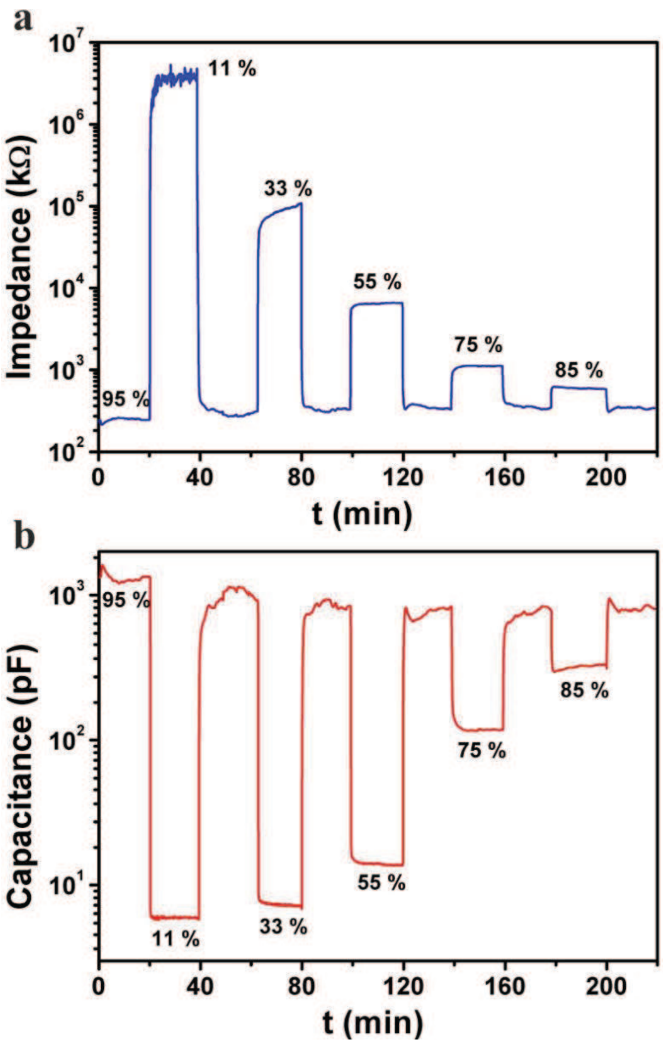

Figure 2.5. Time-dependent (a) impedance and (b) capacitance of $Bi_2O_2CO_3$ sensor at various RH

The response and recovery time is an important parameter for investigating the humidity performance, which is defined as the time required for sample conductance variation to reach 90 % of the equilibrium and return to 10 % above the original conductance. As shown in Figure 2.5 a and b the response time of the process with RH from 95 % to 11 % was about 20 s by impedance measurement and 9 s by capacitance measurement, whereas the recovery time with RH from 11 % to 95 % was about 300 s by impedance measurement and 220 s by capacitance measurement, respectively. Both measurements display a fast response and recovery behavior with stable performance of our sensor. Moreover, the recovery time for both the impedance and capacitance measurements is much longer than the response time, which is similar to the observed time scale for $BiPO_4$ humidity sensors.[15] This result points to rapid water desorption, followed by a slower adsorption process. Figure 2.6 revealed that the highest and lowest resistance and capacitance varied only slightly over 4 cycles with RH from 95 % to 11 %, thereby outlining the good reproducibility of the sensor.

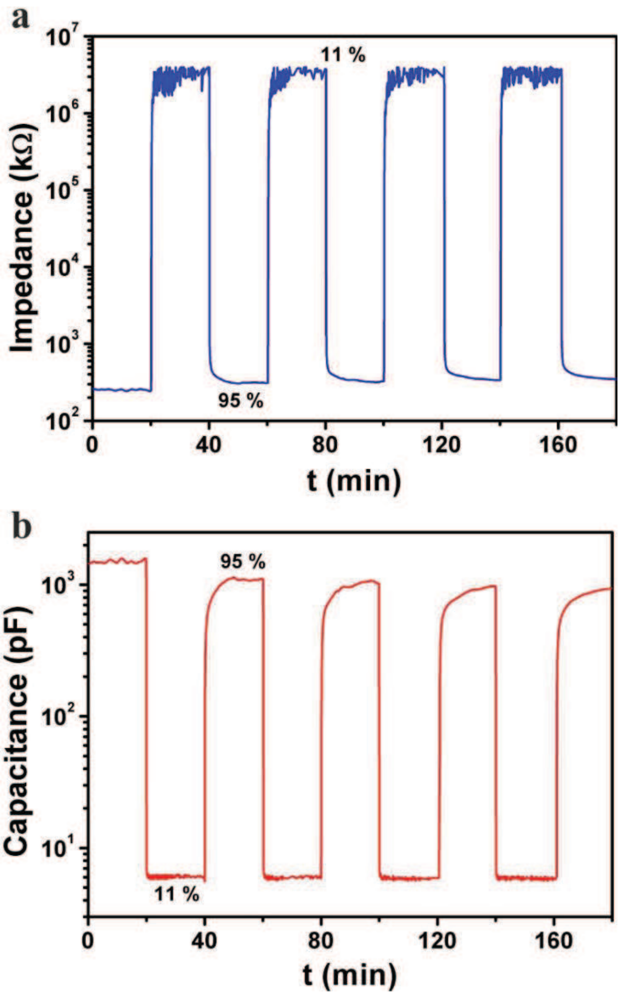

Figure 2.6. Characteristic response and recovery curves for 4 cycles with RH from 95 % to 11 % (a) impedance vs. time; (b) capacitance vs. time.

2.3.3 Complex impedance of $Bi_2O_2CO_3$ sensor

The frequency dependencies of the complex impedance are presented in Figure 2.7. A semicircle at high frequency was observed with RH from 33 % to 95 %. Moreover, the semi-diameter of these curves decreased with RH increasing, and a linear tail appeared when RH is higher than 75 % at low frequency. These observations reveal that the humidity sensing process of $Bi_2O_2CO_3$ sensors include two different stages. Two equivalent circuit models are used to fit the experimental data as shown in Figure 2.7, (a) for RH from 33 – 55 % and (b) for RH from 75 – 95 %. R and C represent the resistance and surface capacitance of $Bi_2O_2CO_3$ film, respectively, while Z_w is the Warburg impedance in the equivalent circuit. The semi-diameter (its value equal to R) change with different RH indicated that intrinsic resistance of $Bi_2O_2CO_3$ film was not fixed because of water adsorption or desorption. It is well known that water molecule adsorption occurs upon exposure of oxides to humid air. By a dissociative process, hydroxyl ions and protons are formed at the available sites of oxide surface and change the oxide resistance through a hopping conduction mechanism by proton transfer between adjacent sites (such as of water molecules or hydroxyl ions).[28] The conductivity variations of $Bi_2O_2CO_3$ films revealed its operation via a similar hopping mechanism. In addition, the variations in Z_w (representing some diffusion process of reactants) with RH increasing up to 75 % indicated that a different conduction process occurred at high RH. With high humidity, a capillary condensation may take place in the pores formed by nanosheets with smaller radius than the Kelvin critical radius on the film surface. The condensed water can supply a liquid layer for electrolyte generation, which finally leads to electrolytic conduction.[29] Based on the above results, the $Bi_2O_2CO_3$ sensors exhibit a hopping conduction mechanism for RH values from 11 % to 75 %, and an additional electrolytic conduction process enhances the conductivity at higher RH.

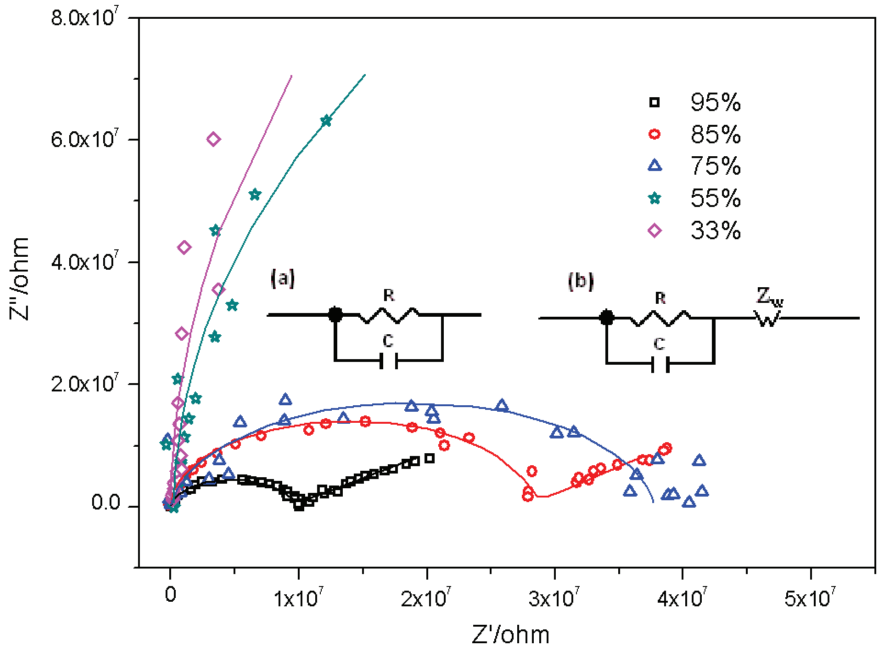

Figure 2.7. Complex impedance plots of $Bi_2O_2CO_3$ sensor (inset: two equivalent circuit models used for fitting the experimental data: (a) for RH from 33 – 55 %; (b) for RH from 75 – 95 %.)

2.4 Conclusions

In summary, $Bi_2O_2CO_3$ nanosheets were obtained via a convenient and facile approach at room temperature, and their humidity sensing properties were investigated. Sensing tests revealed high sensitivities with impedance changes of over 4 orders and capacitance changes of 3 orders of magnitude in the RH range from 11% to 95%. In addition to the good humidity sensing behavior, $Bi_2O_2CO_3$ nanosheet sensors excelled through narrow humidity hysteresis, quick response/recovery time and good reproducibility at high RH values, which indicates their promising reliability for technical purposes. Two different sensing mechanisms were identified by using complex impedance measurements. A hopping conduction mechanism occurs from 11 % to 75 % RH, and an additional conduction process enhances the conductivity at higher RH. The results point to new potential applications of $Bi_2O_2CO_3$ nanosheets for environmental monitoring and humidity control.

References

[1] A. Tsigara, G. Mountrichas, K. Gatsouli, A. Nichelatti, S. Pispas, N. Madamopoulos, N. A. Vainos, H. L. Du, F. Roubani-Kalantzopoulou, *Sens. Actuators B* **2007**, *120*, 481-486.

[2] Z. Wang, C. L. Chang, X. Zhao, W. Qian, X. Zhang, Z. Xie, B. H. Hwang, C. Hu, J. Shen, R. Hui, *J. Power Sour.* **2009**, *190*, 351-355.

[3] Y. Sakai, Y. Sadaoka, M. Matsuguchi, *Sens. Actuators B* **1996**, *35*, 85-90.

[4] E. Traversa, *Sens. Actuators B* **1995**, *23*, 135-156.

[5] P. G. Su, C. L. Uen, *Talanta* **2005**, *66*, 1247-1253.

[6] S. P. Yawale, S. S. Yawale, A. T. Lamdhade, *Sens. Actuators A* **2007**, *135*, 388-393.

[7] D. Chen, L. Li, L. Guo, *Nanotechnol.* **2011**, *22*.

[8] M. L. Wan, Y. Jia, F. Fang, S. S. Zhou, P. Y. Wu, D. Y. Peng, *Thin Solid Films* **2012**, *525*, 35-39.

[9] K. D. Bhatte, D. N. Sawant, R. A. Watile, B. M. Bhanage, *Mater. Lett.* **2012**, *69*, 66-68.

[10] Y. Zhou, G. R. Patzke, *Chimia* **2010**, *64*, 252-258.

[11] G. R. Patzke, Y. Zhou, R. Kontic, F. Conrad, *Angew. Chem. Int. Ed.* **2011**, *50*, 826-859.

[12] G. R. Patzke, F. Krumeich, R. Nesper, *Angew. Chem. Int. Ed.* **2002**, *41*, 2446-2461.

[13] Y. Qiu, S. Yang, *Adv. Funct. Mater.* **2007**, *17*, 1345-1352.

[14] K. B. Zheng, Y. Zhou, L. Gu, X. Mo, G. R. Patzke, G. Chen, *Sens. Actuators B* **2010**, *148*, 240-246.

[15] M. Sheng, L. Gu, R. Kontic, Y. Zhou, K. B. Zheng, G. Chen, X. Mo, G. R. Patzke, *Sens. Actuators B* **2012**, *166*, 642-649.

[16] Y. Zhou, J.-D. Grunwaldt, F. Krumeich, K. B. Zheng, G. Chen, J. Stoetzel, R. Frahm, G. R. Patzke, *Small* **2010**, *6*, 1173-1179.

[17] P. Taylor, S. Sunder, V. J. Lopata, *Can. J. Chem.* **1984**, *62*, 2863.

[18] R. Chen, M. H. So, J. Yang, F. Deng, C. M. Che, H. Z. Sun, *Chem. Commun.* **2006**, 2265-2267.

[19] H. Cheng, B. Huang, K. Yang, Z. Wang, X. Qin, X. Zhang, Y. Dai, *ChemPhysChem.* **2010**, *11*, 2167-2173.

[20] P. Madhusudan, J. Zhang, B. Cheng, G. Liu, *CrystEngComm* **2013**, *15*, 231-240.

[21] Y. Zheng, F. Duan, M. Chen, Y. Xie, *J. Mol. Catal. A* **2010**, *317*, 34-40.

[22] L. Chen, R. Huang, S.-F. Yin, S.-L. Luo, C.-T. Au, *Chem. Eng. J.* **2012**, *193*, 123-130.

[23] Y. Liu, Z. Wang, B. Huang, K. Yang, X. Zhang, X. Qin, Y. Dai, *Appl. Surf. Sci.* **2010**, *257*, 172-175.

[24] T. Zhao, J. Zai, M. Xu, Q. Zou, Y. Su, K. Wang, X. Qian, *CrystEngComm* **2011**, *13*, 4010-4017.

[25] L. Chen, S. F. Yin, S. L. Luo, R. Huang, Q. Zhang, T. Hong, P. C. T. Au, *Ind. Eng. Chem. Res.* **2012**, *51*, 6760-6768.

[26] C. Wu, Y. Xie, *Chem. Commun.* **2009**, 5943-5957.
[27] T. Yang, D. Xia, *J. Cryst. Growth* **2009**, *311*, 4505-4509.
[28] J. H. Anderson, G. A. Parks, *J. Phys. Chem.* **1968**, *72*, 3662-3664.
[29] B. M. Kulwicki, *J. Phys. Chem. Solids* **1984**, *45*, 1015-1031.

3. Humidity sensing materials: Structure-activity relations among bismuth phosphates

3.1 Introduction

Humidity sensors are important devices for humidity control in environmental, industrial and daily life applications.[1,2] Over the past decades, different material types have been investigated as sensing materials for humidity monitoring. The humidity sensing materials can be roughly grouped into three main categories: polymers, semiconductors and ceramics.[3-6] Among them, oxide materials are the preferred candidates as humidity sensors for a variety of reasons. The large family of oxide provides almost endless chemical compositions accompanied by various morphological and surface properties. Recently, ZnO,[7-11] SnO_2,[12-14] CuO,[15-17] WO_3,[18,19] and TiO_2-ZrO_2[20-22] have been in the main focus of humidity sensor research. Furthermore, alkali chloride-doped oxides, such as LiCl-doped TiO_2,[23] silica MCM-41[24] and ZnO[25] have also been reported as potential humidity sensors. However, their issue of instability at high relative humidity still remains to be solved.[4] Spinel and perovskite oxides are interesting candidates as humidity oxides due to their large compound families with flexible compositions.[26-28] However, their humidity detection at elevated temperature limits the application options.[5]

In our previous work, bismuth-containing oxides, such as bismuth vanadates, tungstates and molybdates were identified as application-oriented photocatalysts.[29-32] Moreover, bismuth ternary oxides in various structures emerge as new candidates for humidity sensing applications.[33,34] *Aurivillius* type Bi_2MO_6 (M = Mo, W) nanosheets and $Bi_6S_2O_{15}$ nanowires exhibit quick response/recovery and good reproducibility at room temperature over a wide range of humidity values. This renders the large family of bismuth oxide-related compounds a promising target for the development of novel humidity sensor types. Along these lines, the investigation and exploration of further bismuth-containing humidity sensors is pursued in the following.

The sillenite family offers a variety of compounds which have the general formula $Bi_{12}(Bi_{4/5-nx}M^{n+}_{5x})O_{19.2+nx}$ (M = M^{2+}, M^{3+}, M^{4+} and M^{5+} (only V, As and P)) in common.[35] Their unique physical properties, such as high strength of piezoeffect, electro-optical activity and high photosensitivity, give rise to a wide application potential.[36] The structure and fundamental properties of sillenite oxides have attracted research interest since decades. *Betsch* et al.

reported on vibrational spectra of sillenite-structured bismuth oxides.[37] *Valant* et al. investigated processing and dielectric properties of the sillenite compounds $Bi_{12}MO_{20}$ (M = Si, Ge, Ti, Pb, Mn, $B_{1/2}P_{1/2}$).[38] In addition to structural and electrical properties, the photocatalytic and some sensing applications were studied by several research groups.[39-44] To the best of our knowledge, only γ-Bi_2O_3 from the sillenite family has been investigated on films as smoke sensors at an elevated operating temperature of $\geq$720 °C, whereas normal bismuth oxides and their combinations with other oxides have been rather studied as NO sensors and CO sensors.[45-47] This leaves us room for exploration of further application potentials of sillenite-type bismuth oxide derivatives.

Cubic bismuth phosphate has been synthesized from the Bi_2O_3-P_2O_5 binary system with varying Bi:P ratios from 13:1 to 16:1. Increasing Bi:P ratios lead to increase of the cubic lattice parameter.[48] Another access to cubic bismuth phosphate was reported by *Zhereb* et al. via the Bi_2O_3-$BiPO_4$ system.[49] Both solid state synthesis systems approach variable Bi:P ratios, i.e. Bi:P = 13:1 – 16:1, in a sillenite-type tunnel structure of a Bi/O-framework with PO_4^{3-} tetrahedra incorporated into the channels.[50]

Some modifications of bismuth phosphate or Bi-compounds doped with molybdenum have been investigated as catalysts with high selectivity for various organic transformations.[51-54] Among the three types of bismuth phosphate, monazite-type monoclinic $BiPO_4$ with Bi-linked PO_4^{3-} tetrahedra is the most stable form, which is well known as low-temperature monoclinic $BiPO_4$ (LTMBIP).[55] This modification can undergo a transformation into high-temperature monoclinic $BiPO_4$ (HTMBIP) under certain conditions.[56] The syntheses of a new type of hexagonal $BiPO_4$ nanorods was reported via electrochemical and sonochemical techniques by *Yang* et al. and *Geng* et al.[57,58]

In this work, we synthesized bismuth phosphates of the sillenite- and monazite-types via convenient hydrothermal routes. Both materials were analytically characterized with respect to structure, morphology, thermal stability and hydrophilicity. In the following, their humidity sensing properties are compared concerning capacitance change, response behavior and response/recovery time. The sensing performances point to cubic sillenite-type bismuth phosphate as a promising candidate for humidity sensing applications.

3.2 Experimental section

3.2.1 Syntheses

3.2.1.1 Synthesis of bismuth phosphates at different pH values

500 mg Bi_2O_3 and 700 mg K_3PO_4 were dispersed in 10 mL DI water by stirring in a 15 mL Teflon liner. pH values of 3 – 12 were adjusted by titrating with 10 % HCl. The mixture was subsequently transferred into a stainless steel autoclave and maintained under constant magnetic stirring at 120 °C for 24 h, followed by cooling to room temperature. All products were collected by centrifugation, repeatedly washed with water and air-dried at 80 °C.[59]

3.2.1.2 Time-dependent synthesis of cubic bismuth phosphates

500 mg Bi_2O_3 and 700 mg K_3PO_4 were dispersed in 10 mL DI water by stirring in a 15 mL Teflon liner without additional treatments. The mixture was subsequently transferred into a stainless steel autoclave and maintained under constant magnetic stirring at 120 °C for 0 min, 15 min, 40 min, 50 min, 1 h and 3 h, respectively. All intermediate products were obtained by centrifugation and washed with DI water, followed by drying in air at 80 °C.

3.2.1.3 Time-dependent synthesis of monoclinic bismuth phosphate

97 mg (0.2 mmol) $Bi(NO_3)_3 \cdot 5H_2O$ and 26.3 mg (0.2 mmol) $(NH_4)_2HPO_4$ were mixed with 10 mL DI water and stirred in a 15 mL Teflon liner at room temperature until a homogeneous mixture was obtained. The Teflon liner was transferred into a stainless steel autoclave and heated at 220 °C. Products were collected after 0 min, 30 min, 1 h, 2 h and 3 h. They were centrifuged and washed with DI water, followed by drying in air at 80 °C.

3.2.2 Analytical characterization

Products were characterized by powder X-ray diffraction (XRD) on a STOES TADI P diffractometer in transmission mode (flat sample holders, Ge monochromator and Cu $K_{\alpha 1}$ radiation) operated at 40 kV and 40 mA. Scanning electron microscopy (SEM) analyses were conducted on a LEO 1530 (FEG) microscope (2 keV) with samples dispersed in ethanol and subsequently deposited on a silicon wafer. Brunauer-Emmett-Teller (BET) surface area measurements were performed on a Quantachrome Quadrasorb SI in N_2-adsorption mode.

Samples were degassed at 150 °C for > 3 h *in vacuo* prior to nitrogen adsorption measurements. High resolution transmission electron microscopy (HRTEM) was performed on a Tecnai F 30 ST (FEG, 300 kV, SuperTwin lens). Wettability measurements on static contact angle were performed with the Contact Angle System "KrüssDSA 100" and included DSA-1 software. Static contact angles were determined by the sessile drop method.

3.2.3 Humidity sensor fabrication and sensing measurements

Humidity sensors were prepared as described in our previous work on bismuth tungstate and molybdate sensors.[33] Au interdigital electrodes were fabricated on a quartz substrate with finger distances set to 200 µm. 200 mg of bismuth phosphate and 0.2 mL terpinol with 5 wt% ethylcellulose were mixed with 0.04 mL acetylacetone into a homogeneous paste that was transferred onto the electrode using the "*Doctor Blade*" method.[59] The electrode was annealed in air for 10 min at 150 °C and the organic compounds were removed through heating for 10 min at 350 °C, followed by 30 min at 500 °C. A film with a thickness of 10 µm was obtained after cooling to room temperature.

Humidity sensing measurements were performed on a TH 2617 LCR analyzer (Changzhou, China). The applied AC voltage was 1 V and the frequency was varied from 100 Hz to 100 kHz. Humidity environments were simulated by using supersaturated aqueous solutions of different salts ($LiCl$, $MgCl_2$, $Mg(NO_3)_2$, $NaCl$, KCl and KNO_3) in a closed glass vessel, corresponding to relative humidity values of 11 %, 33 %, 55 %, 75 %, 85 % and 95 %, according to standard protocols.[60,61] All measurements were carried out at ca. 28 °C.

3.3 Results and discussion

3.3.1 Structure and morphology of cubic bismuth phosphate samples

Powder X-ray diffraction (PXRD) patterns of as-synthesized bismuth-containing products obtained at initial pH-values from 3 – 12 are shown in Figure 3.1. The reaction was performed for 24 h and the temperature was kept constant at 120 °C. Monoclinic Bi_2O_3 (JCPDS No.41-1449) can be clearly identified as main component with several unidentified weak peaks, when the pH value was below 8. When the pH value was increased to 11, monoclinic Bi_2O_3 can still be observed, but an additional strong peak appeared. The resulting phase pure cubic bismuth phosphate was obtained instead of mixed phases with an initial pH value of 12. The diffraction peaks of the final product agree well with literature data for cubic $Bi_{12}P_{0.86}O_{20.14}$ (PDF 44-0199, S.G. *I23*, a = 10.1761(4) Å).

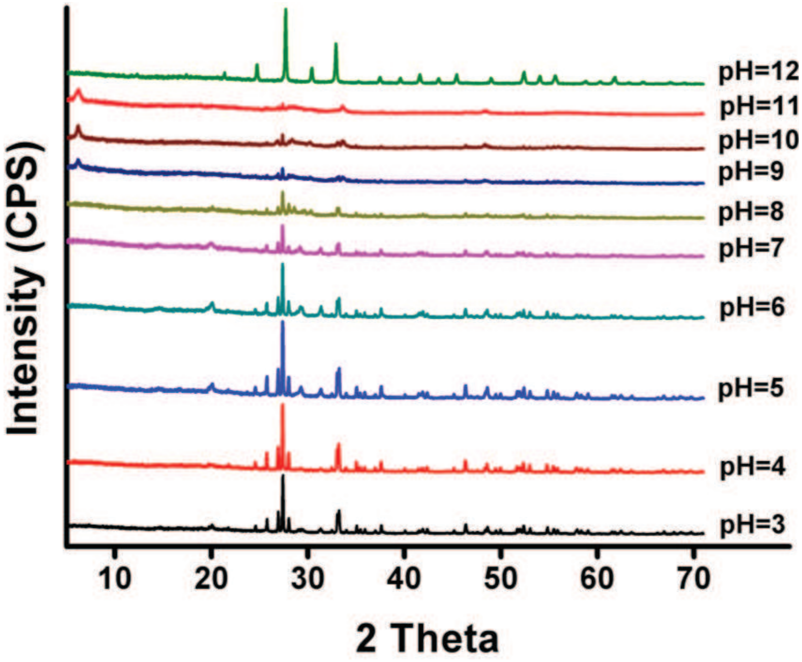

Figure 3.1. PXRD patterns of samples obtained at different pH values (3 to 12).

Based on the preliminary tests, the optimal pH value for the synthesis of cubic bismuth phosphate was fixed at 12. Structural properties of the intermediate products were investigated after different reaction times. PXRD patterns as shown in Figure 3.2 demonstrated that no phase transformation of monoclinic Bi_2O_3 occurred in the first 50 min. Cubic bismuth phosphate as final product was observed after 1 h and maintained under the given hydrothermal conditions.

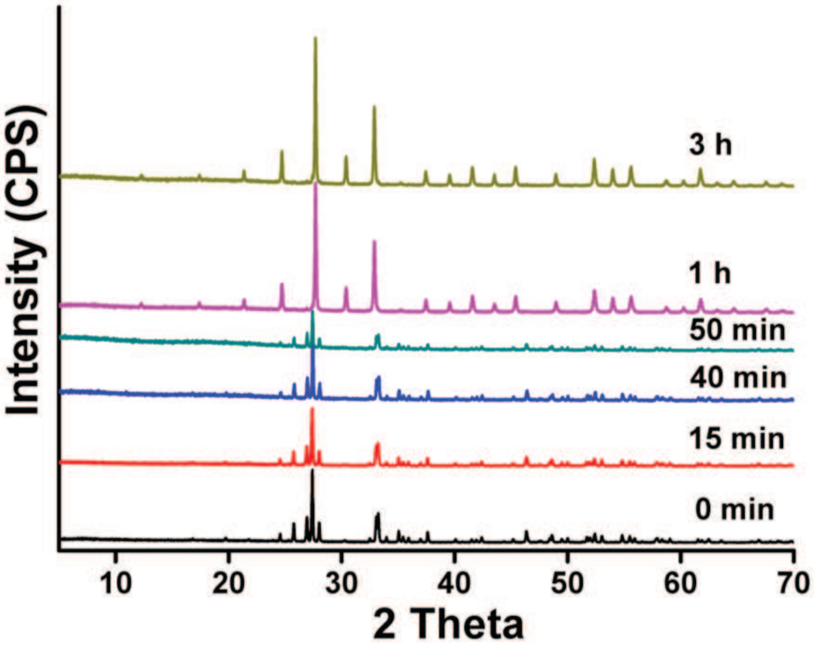

Figure 3.2. Time-dependent PXRD patterns of cubic bismuth phosphate formation after 0 min, 15 min, 40 min, 50 min, 1 h and 3 h, respectively.

Furthermore, SEM images illustrate the morphological properties of the as-synthesized intermediate bismuth-containing oxides (Figure 3.3). The morphology of commercial Bi_2O_3 powder was observed during the first 15 min with a particle size of ca. 40 µm. After 40 min, the particle shapes of the bulk powder became angular and smaller. The final cube-shaped morphology with particle sizes around 3 – 9 µm was obtained after 1 h and maintained in the further hydrothermal treatment (PDF 080-0209, S.G. $P2_1/n$, a = 6.4882(8) Å, b = 6.9516(1) Å, c = 6.7621(1) Å, β = 103.736(1)°).

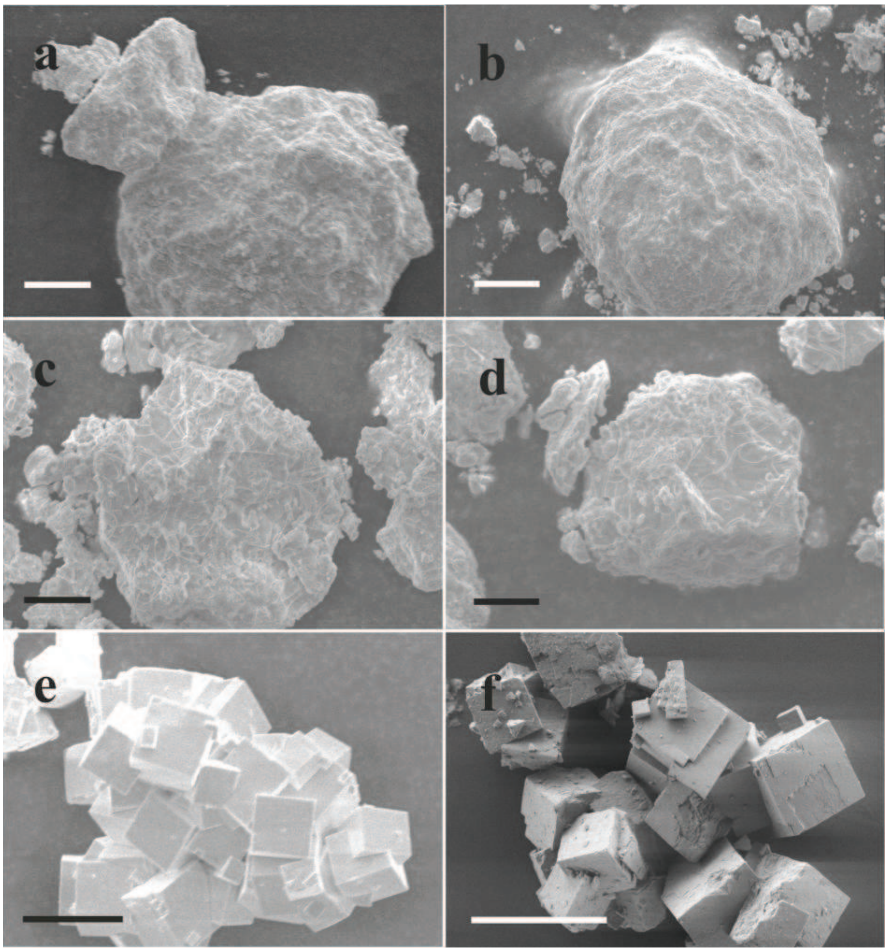

Figure 3.3. SEM images of (a) Bi_2O_3 precursor; (b) intermediate product after 15 min; (c) intermediate product after 40 min; (d) intermediate product after 50 min; e) formation of cube-shaped bismuth phosphate after 1 h and (f) final morphology of cube-shaped bismuth phosphate after 3 h (scale bar = 10 µm).

Structure and morphology development of monoclinic bismuth phosphate were studied with related strategies. Figure 3.4 illustrates the formation process during the first 3 h for selected reaction times. Interestingly, the diffraction peaks of a metastable hexagonal phase of $BiPO_4$ were observed during the initial 30 min. Next, hexagonal $BiPO_4$ was transformed into a phase mixture of monoclinic $BiPO_4$ and unknown intermediate products. The final product monoclinic $BiPO_4$ was obtained after 2 h of hydrothermal treatment. All diffraction peaks agree well with ICSD data of $BiPO_4$ (PDF 15-0767).

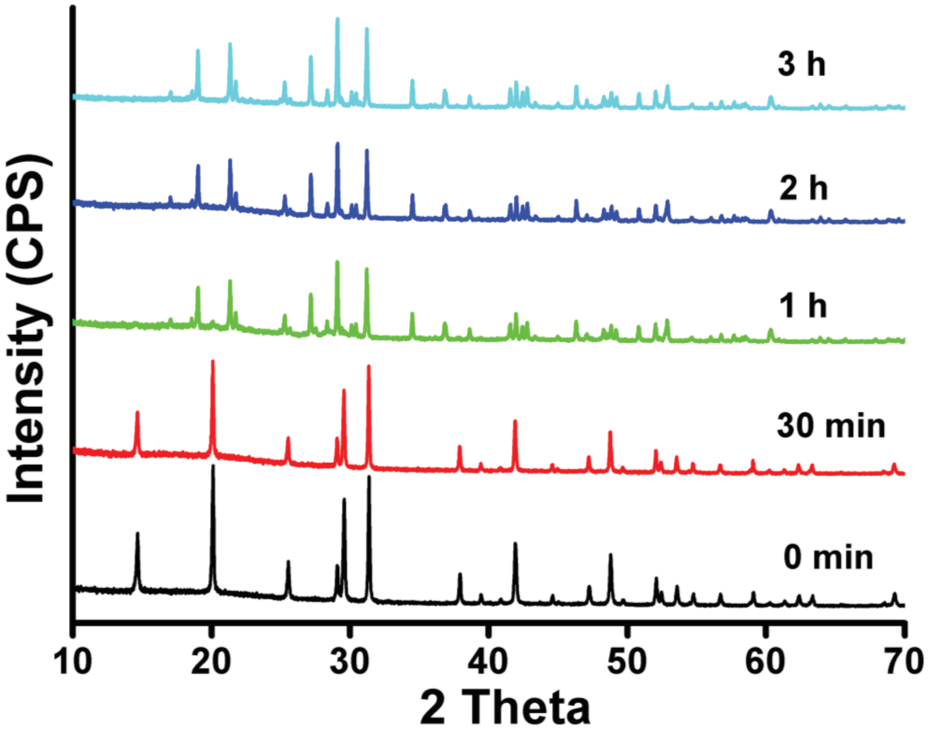

Figure 3.4. Time-dependent PXRD patterns during hydrothermal synthesis of monoclinic bismuth phosphate after 0 min, 30 min, 1 h, 2 h and 3 h, respectively.

Morphological evaluations of intermediate bismuth-containing products of $BiPO_4$ were monitored with SEM investigations (Figure 3.5). SEM images demonstrate that the formation of metastable hexagonal $BiPO_4$ proceeds with homogenous nano-scale morphologies in the first 30 min. Next, monoclinic $BiPO_4$ was formed with a particle size of ca. 0.5 – 3 µm after 1 h reaction time. Irregular morphology and particle size were maintained in the final product.

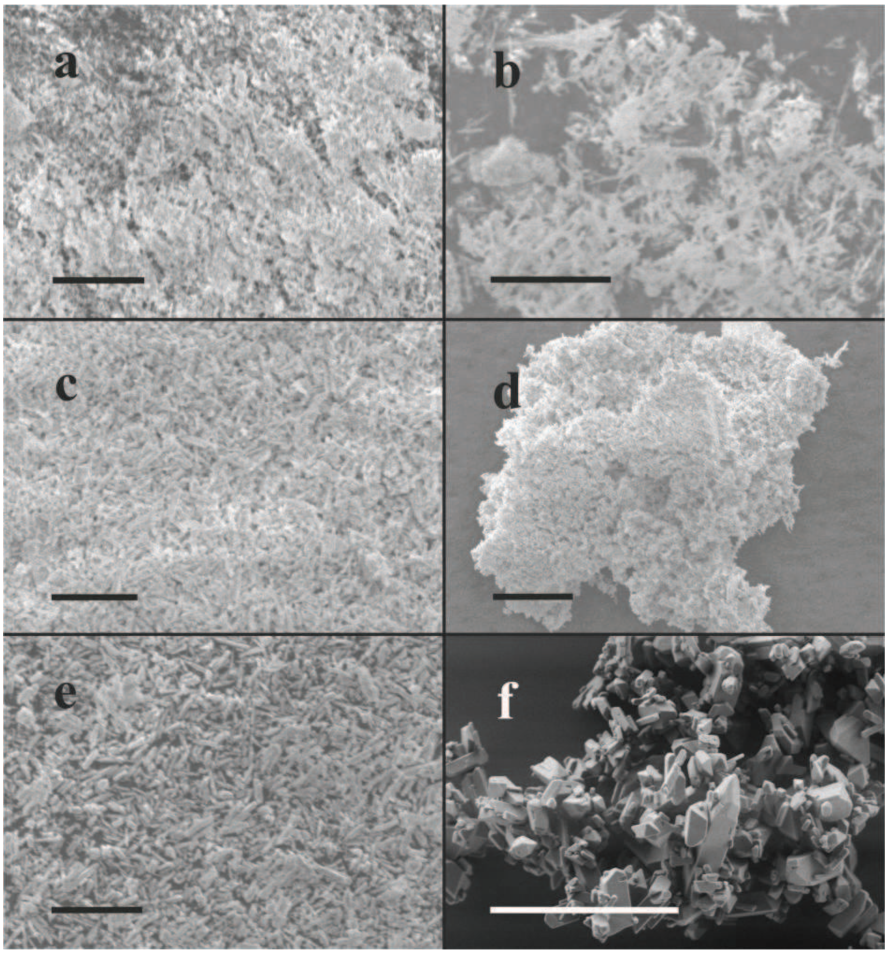

Figure 3.5. SEM images of intermediate hexagonal $BiPO_4$ after (a) 0 min; (b) 30 min; impure monoclinic $BiPO_4$ and unknown phase after (c) 1 h; (d) 1 h 15 min; final product monoclinic $BiPO_4$ after (e) 2 h and (f) 3 h (scale bar = 10 µm for (a – e), scale bar = 5 µm for (f)).

Phase purity of both compounds is maintained after heat treatment for 1 h at 500 °C, and the lattice constants change only slightly to $a = 10.1598(2)$ Å for cubic bismuth phosphate and to $a = 6.4782(3)$ Å, $b = 6.9418(3)$ Å, $c = 6.7563(3)$ Å, $\beta = 103.702(4)°$ for monoclinic bismuth phosphate, respectively. Elemental analyses of as-synthesized and calcined cubic sillenite-type samples revealed Bi:P ratios around 13.1:1, i.e. the obtained $Bi_{13.1}PO_{\delta}$ is at the lower limit of Bi:P ratios reported for Bi_xPO_{δ} ($13 \leq x \leq 16$; $\delta \sim 17$-20) compounds obtained from solid state methods.[48] Note that a precise determination of the oxygen content was not possible due to typical analytical problems with the present element combination.

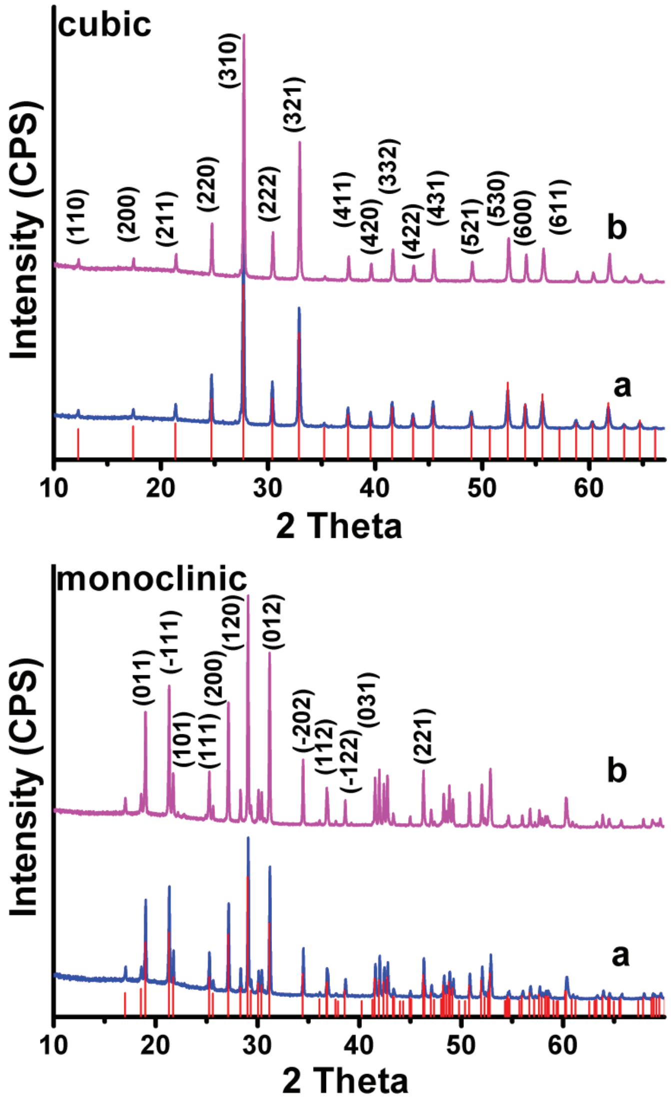

Figure 3.6. XRD patterns of cubic and monoclinic bismuth phosphate before (blue, bottom) and after (pink, top) thermal treatment for 1 h at 500 °C.

The structural motifs of both compounds are compared in Figure 3.7. Cubic bismuth phosphate (Figure 3.7 a) is a member of the $Bi_{12}MO_{20}$ (M = Bi, P, Fe, Zn, V...) sillenite family. Depending on the host atom incorporated into the channels of the structure, sillenites allow for manifold defect types, such as cation and oxygen vacancies or excess oxygen, respectively.[48] The presence of Bi(V) in cubic sillenite-type γ-Bi_2O_3 has been controversially discussed, but has never been experimentally verified. Instead, a structural model based on the interplay of oxygen deficiency and compensating lone pairs of Bi^{3+} was proposed.[35] Low-temperature monoclinic $BiPO_4$ (Figure 3.7 b) displays an entirely different monazite-type structure with layers of PO_4 tetrahedra linked by Bi atoms with interlayer contacts via longer Bi-O bonds.[55]

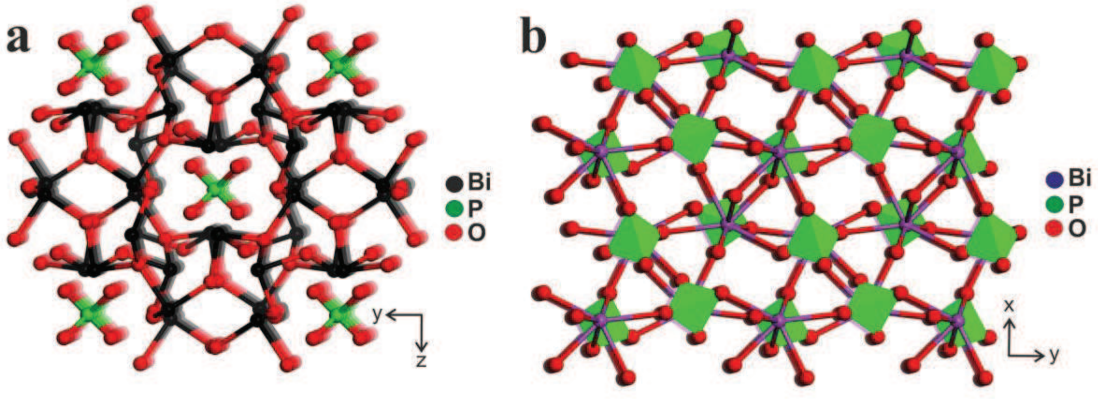

Figure 3.7. Structure motifs of (a) sillenite-type cubic bismuth phosphate (b) and monoclinic bismuth phosphate.

SEM images illustrate that the cubic bismuth phosphate structure is morphologically reflected in the formation of regular particles with dimensions between 3 and 9 µm (Figure 3.8 a), whereas monoclinic bismuth phosphate forms smaller particles with irregular shapes (0.5 – 3 µm) that are densely agglomerated (Figure 3.8 c and d). Both bismuth phosphate types maintain their phase and characteristic morphologies upon thermal treatment at 500 °C so that they are sufficiently stable for the following humidity sensing characterizations (cf. Figures 3.8 b and d). Surface areas for cubic and monoclinic bismuth phosphate were determined as 0.2 m^2/g and 1.8 m^2/g, respectively. HRTEM images of both bismuth phosphates are shown in Figure 3.9 and measurements are generally hindered by the typical decomposition of BiO_x-type compounds under the electron beam (cf. also characteristic spherical decomposition products in Figure 3.9 b).[62] SAED patterns of both compounds prove the presence of crystalline phases (cf. Figures 3.9 and 3.10).

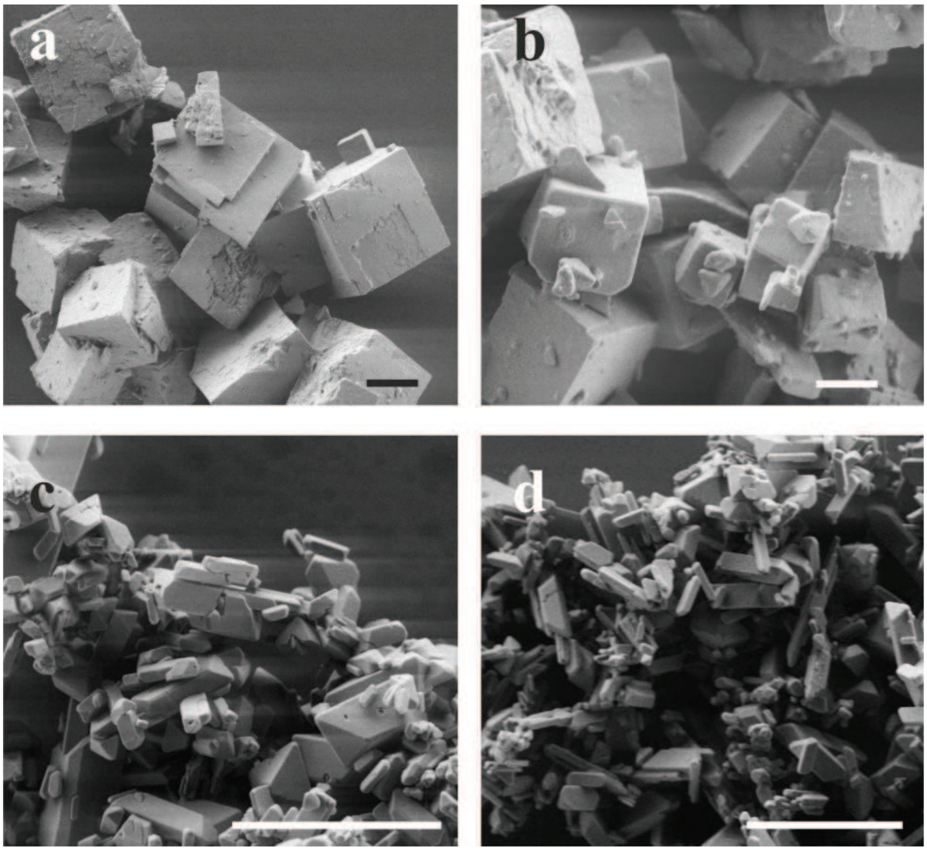

Figure. 3.8. Representative SEM images (scale bar = 3 μm) of cubic bismuth phosphate (a) before and (b) after heat treatment compared to (c) as-synthesized and (d) thermally treated monoclinic bismuth phosphate.

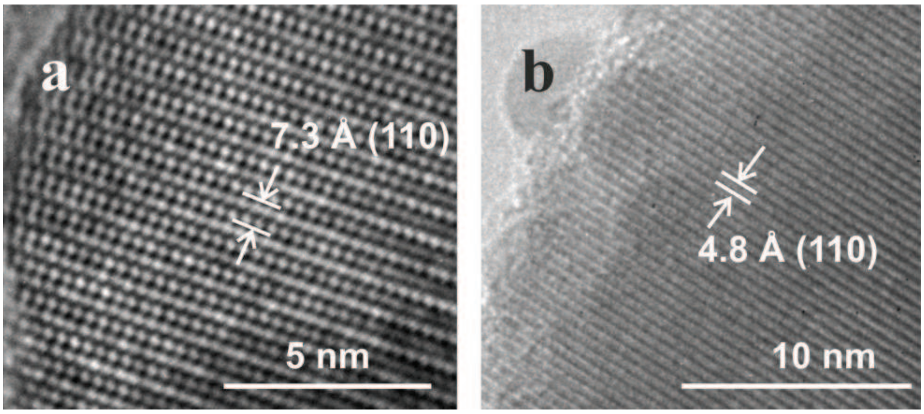

Figure 3.9. Representative HRTEM images of (a) sillenite-type cubic bismuth phosphate and (b) monoclinic bismuth phosphate.

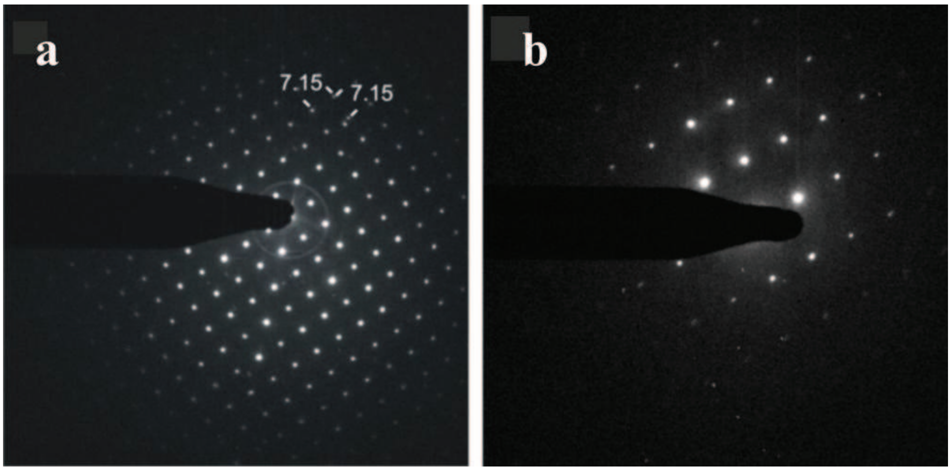

Figure 3.10. SAED patterns of (a) cubic bismuth phosphate (corresponding to Figure 3.9 a) and of (b) monoclinic bismuth phosphate (no crystal orientation of the monoclinic phase could be achieved due to rapid deterioration of the crystal under the electron beam).

The wettability of both samples was examined by water contact angle (WCA) measurements as illustrated in Figure 3.11. The results of surface wettability studies shows significant difference that cubic bismuth phosphate exhibits an average contact angle of 31.5°, which is much lower than that of monoclinic bismuth phosphate. This demonstrated that the surface of cubic bismuth phosphate is more hydrophilic than that of monoclinic bismuth phosphate and may be an indication for better water adsorption.

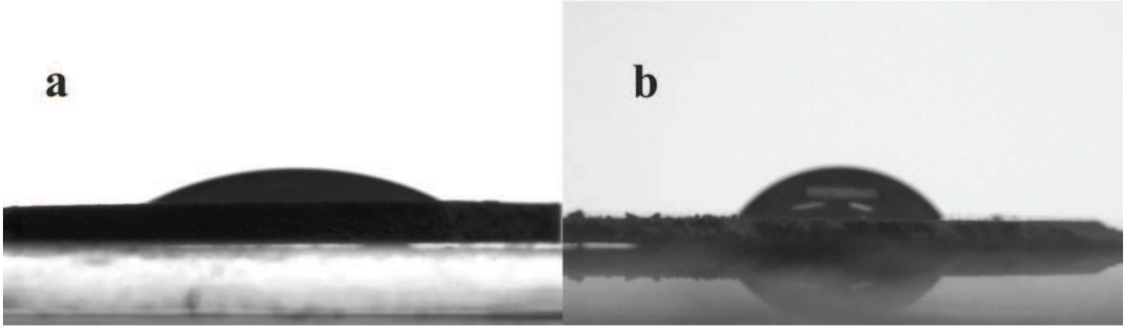

Figure 3.11. Wettability tests with (a) cubic (av. contact angle = 31.5°) and (b) monoclinic bismuth phosphate (av. contact angle = 48.9°).

3.3.2 Humidity sensing properties

Humidity sensing properties of the different bismuth phosphate forms were characterized with capacitance measurements as a key physical quantity to monitor relative humidity (RH) variations. Generally, capacitance decreases with increasing operational frequency. Measurements on cubic and monoclinic bismuth phosphate were performed at different signal frequencies of 100 Hz, 1 kHz, 10 kHz, 40 kHz and 100 kHz, respectively. Figure 3.12 shows that the capacitance of both bismuth phosphate types increases with decreasing frequencies. This can be explained with a delayed polarization of adsorbed water molecules in an externally applied field.

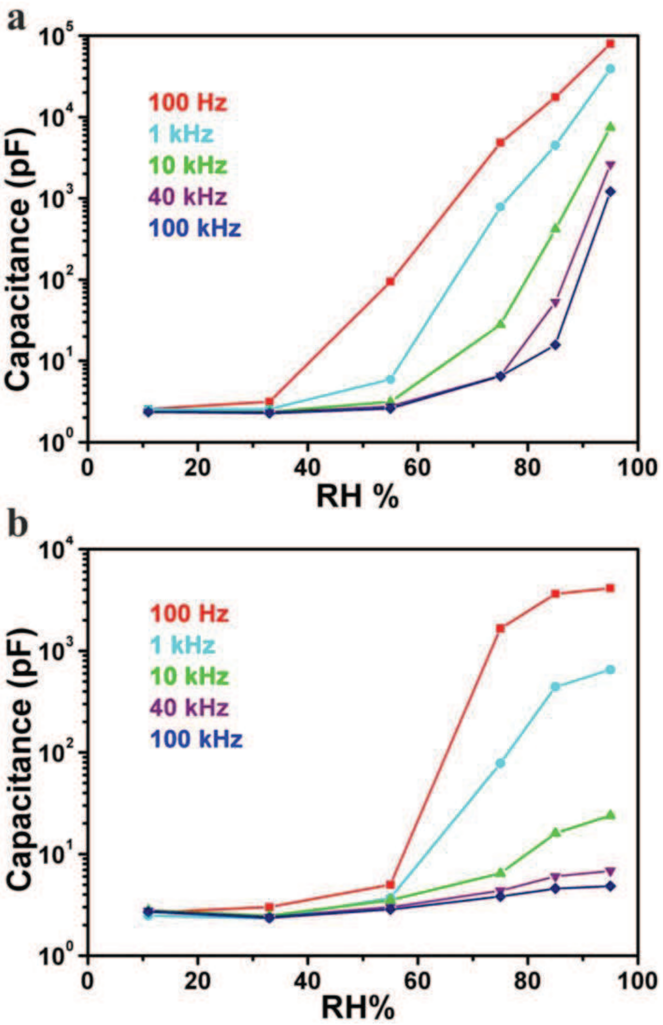

Figure 3.12. Capacitance vs. relative humidity at frequencies of 100 Hz, 1 kHz, 10 kHz, 40 kHz and 100 kHz for (a) cubic and (b) monoclinic bismuth phosphate.

Furthermore, both compounds display different humidity sensing performances as outlined in detail below. The capacitance of cubic bismuth phosphate remains almost constant from 11 % RH to 33 % RH which is probably due to a low degree of adsorption of water molecules (Figure 3.12 a). Between 55 % RH and 95 % RH, the capacitance values increase significantly over the entire frequency range with maximum values observed at 100 Hz. Two factors contribute to this trend: firstly, increasing humidity facilitates water adsorption on the sample surface and secondly, low frequencies lead to high permittivity and the according enhanced capacitance values.

Other than cubic bismuth phosphate, the monoclinic form displays almost identical and constant capacitance values up to 55 % RH for all frequencies (Figure 3.12 b). At higher humidity values, the expected increase in capacitance with decreasing frequencies is observed. The capacitance of both samples does not vary considerably at higher frequencies (40 and 100 kHz in Figure 3.12) which indicates a delay of water molecule polarization on the materials surface in line with our preceding studies on Bi_2MO_6 (M = W, Mo) humidity sensors.[33]

For more detailed sensing characterizations, operating frequency and AC voltage were thus kept constant at 1 kHz and 1 V, respectively. Next, the response behavior of both bismuth phosphate types (defined as $C_{RH\%}/C_{11\%}$) was studied over the entire relative humidity range (Figure 3.13). Cubic bismuth phosphate exhibits good response behavior with an increase of 4 orders of magnitude up to 95 % RH, namely from 1.1 to 12908, that can be expressed with a linear relationship (Figure 3.13 a). In contrast, the maximum response of monoclinic bismuth phosphate increases only over 3 orders of magnitude from 1.2 to 1097 in a non-linear fashion (Figure 3.13 b). Two response regions can be differentiated: a negligible response variation between 1.2 and 1.5 was observed between 33 % and 55 % RH, followed by a stepwise increase by one order of magnitude each for 75 %, 85 % and 95 % RH.

Furthermore, the adsorption and desorption characteristics of both samples were studied and the characteristic hysteresis curves are displayed in Figure 3.14. As discussed above, cubic bismuth phosphate displays higher capacitance values than the monoclinic form. Interestingly, the latter exhibits a sharper hysteresis curve with only slight deviations around 75 % RH. The adsorption/desorption behavior of cubic bismuth phosphate is less consistent in the range from 55 % to 75 % RH with better reproducibility in the lower and higher RH ranges. Desorption for both samples proceeds at higher capacitance values with respect to the according adsorption processes at the same humidity values, especially in the 55 % to 75 % RH region. This points to rapid water adsorption, followed by a slower desorption process.[33]

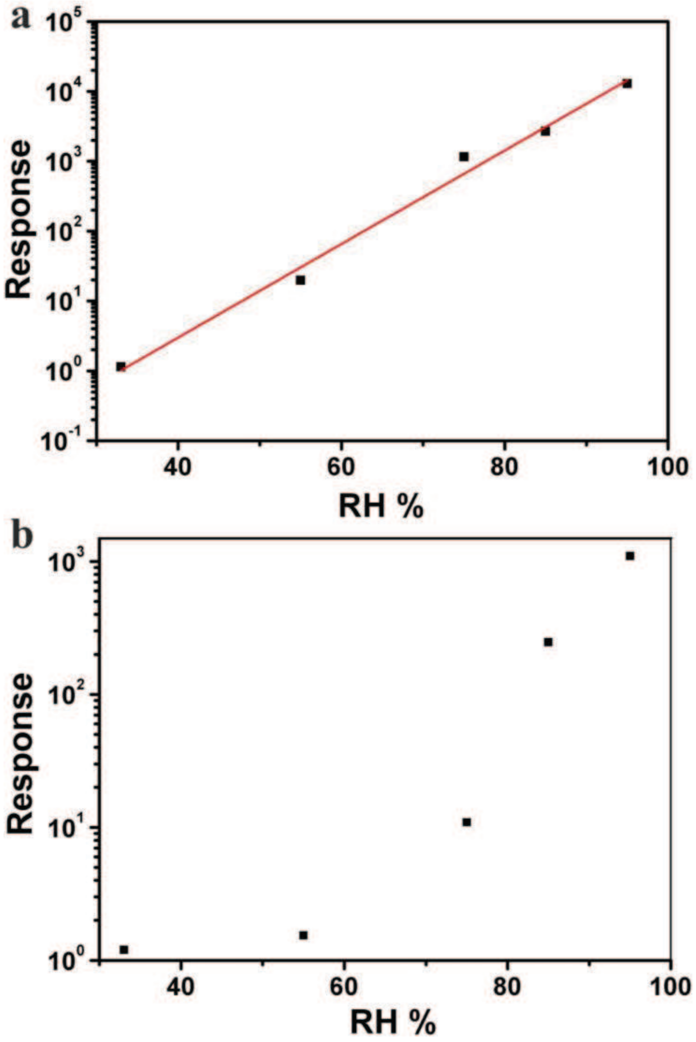

Figure 3.13. (a) Logarithmic response behavior vs. RH for cubic bismuth phosphate following the expression y = - 2.2 + 0.06695 x (correlation coefficient R = 0.99544); (b) non-linear relation of response vs. RH for monoclinic bismuth phosphate.

In order to verify stable and reproducible sensing behavior of both bismuth phosphate forms, capacitance was measured for several response and recovery cycles at selected steps as shown in Figure 3.14.

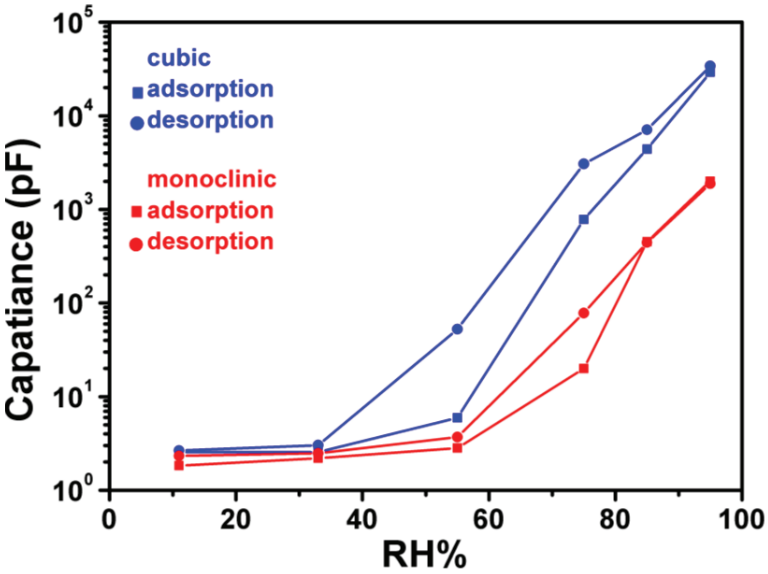

Figure 3.14. Adsorption and desorption curves for cubic and monoclinic bismuth phosphate.

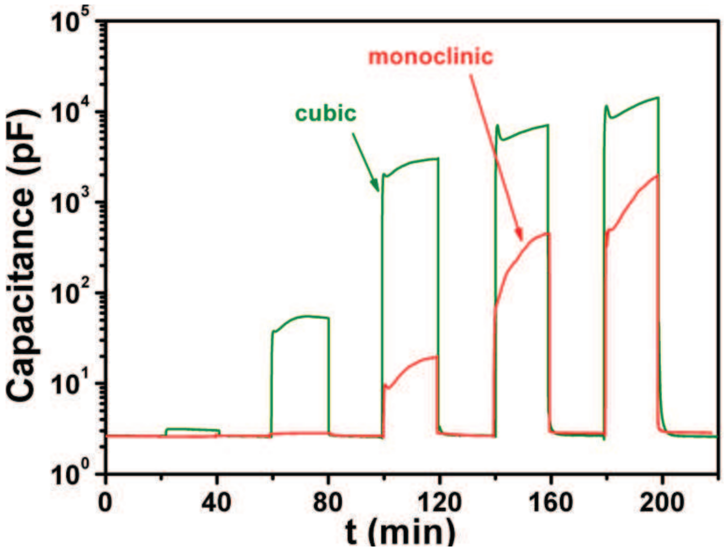

Figure 3.15. Characteristic response and recovery times at different humidity values for cubic (green) and monoclinic (red) bismuth phosphate.

Each cycle was measured over 20 min in a constant humidity environment and the observed stable response and recovery times indicate good reproducibility. In line with the above results, cubic bismuth phosphate generally displayed a better response behavior than the monoclinic form and reached maximum capacitance values more quickly, namely on a 20 % faster timescale, over the entire humidity range. Whereas the capacitance of monoclinic bismuth phosphate remained practically constant between 11 % and 55 % RH, followed by a constant capacitance increase at higher RH values, the cubic form already undergoes a rise of ca. 2 orders of magnitude up to 55 % RH. Both samples display a good and rapid recovery behavior at values of 75 % RH and above.

The response and recovery times are plotted vs. relative humidity for both bismuth phosphate types in Figure 3.16.

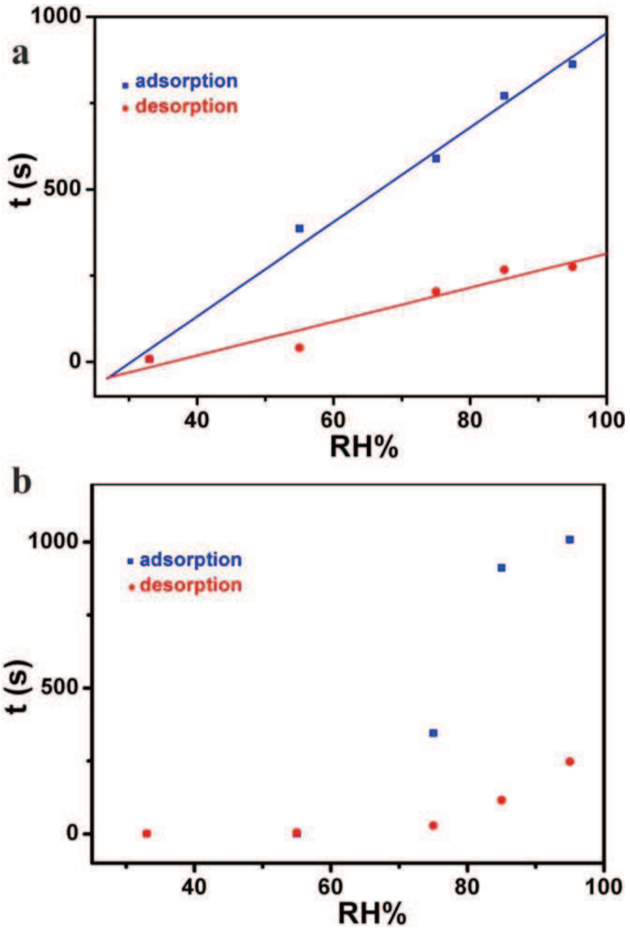

Figure 3.16. Response and recovery times vs. RH for (a) cubic bismuth phosphate and (b) monoclinic bismuth phosphate.

They are defined as the intervals required to achieve 90 % of the capacitance change for the adsorption and desorption processes, respectively. In line with the above capacitance characteristics (Figure 3.14), desorption curves for both samples proceed on a lower time scale than the respective adsorption curves, and cubic bismuth phosphate displays linear relationships for each process. This linear behavior indicates steady water adsorption and desorption processes over the entire RH range which are proportional to variations in capacitance and reacting time.

In comparison, monoclinic bismuth phosphate displays longer response and shorter recovery times, thereby pointing to surface hydrophilicity differences between the different bismuth phosphate types. Figure 3.17 demonstrates that both materials display good reproducibility over several cycles, and Figure 3.18 illustrates the long-term stability of cubic bismuth phosphate which renders it promising for technical applications.

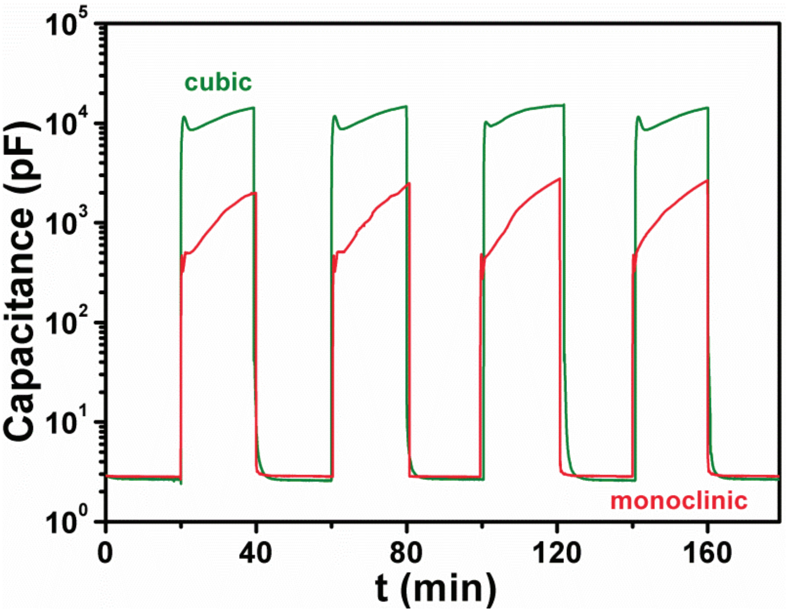

Figure 3.17. Stable response and recovery times for both sensor-types from 11 % to 95 % (green = cubic, red = monoclinic bismuth phosphate).

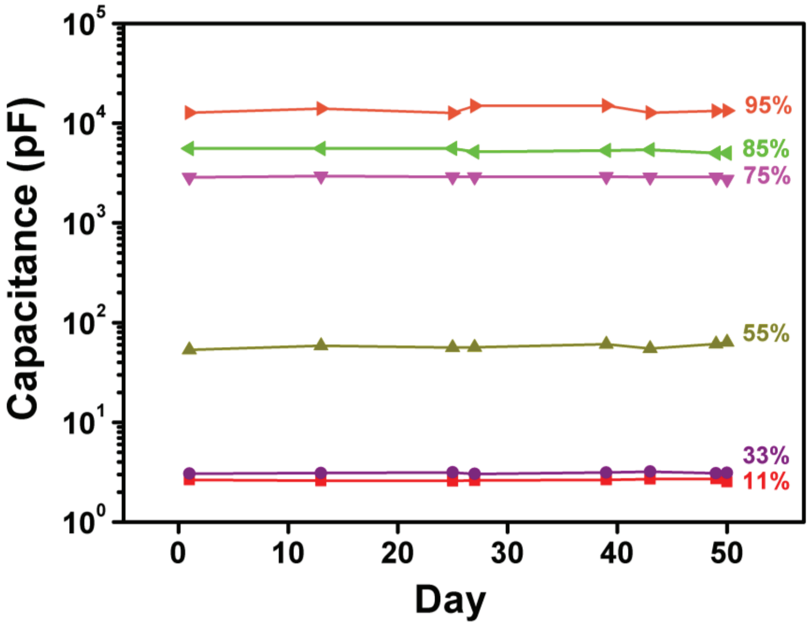

Figure 3.18. Long-term stability of cubic bismuth phosphate at various RH values over 50 days.

3.3.3 Bismuth phosphate structure types vs. their humidity sensing mechanisms

Humidity sensing mechanisms have been established in the course of previous studies and they can be divided into two main types:[63-65] "non-Debye" types at low humidity range and "ion-transport" mechanisms at high humidity range. Upon exposure to environments with low humidity, the sensor surface is only partially covered by water molecules so that proton migration proceeds via hopping between sites on the surface. At higher RH values, however, one or more water layers on the surface facilitate the transfer of H^+ or H_3O^+, thereby leading to a notable capacitance increase. From our previous work on *Aurivillius*-type Bi_2MO_6 (M = W, Mo) humidity sensors, we concluded that the transition between these two mechanisms occurs at a lower RH for the sensor with better sensing properties, i.e. Bi_2WO_6.[33,66]

As shown in Figure 3.12, an increase in capacitance can be clearly observed at 33 % RH for cubic bismuth phosphate (below 1 kHz) while it occurs at 55 % RH for the monoclinic compound (below 10 kHz). This points to better polarization (i.e. enhanced capacitance) at lower RH values for the cubic form. Wettability tests on pellets of both bismuth phosphate types furthermore showed that cubic bismuth phosphate displays a lower contact angle than monoclinic $BiPO_4$ (Figure 3.11). This agrees with the better sensing response of the cubic form - despite its 9-fold lower surface area compared to monoclinic $BiPO_4$ - and Figure 3.17 also points to better multilayer formation on cubic bismuth phosphate.

Whilst our preceding studies on Bi_2MO_6 (M = W, Mo) humidity sensors were focused on the differentiation between W- and Mo-effects on the sensing properties of the *Aurivillius*-type bismutates, the present investigation pursues a complementary strategy by comparing two different structural motifs of bismuth phosphate. This places more emphasis on the influence of crystal structure and bismuth content on the humidity sensing properties. The capacitance characteristics and adsorption/desorption hystereses of cubic sillenite-type bismuth phosphate and Bi_2WO_6 are comparable. Other than Bi_2WO_6, however, cubic sillenite-type bismuth phosphate displays a linear RH response time behavior (Figure 3.16) which points to a more regular adsorption process that may be caused by better surface polarization due to higher bismuth contents through P-incorporation into the sillenite-type bismuth oxide channels (Figure 3.7 a).

Generally, humidity sensing properties arise from a complex interplay of preparative/thermal history, surface area/properties, crystal structure and composition. In the present case, the effects of structure and P-content on the sensing performance of both bismuth phosphate structure types cannot be entirely differentiated. At first glance, the superior sensing behavior of the Bi-rich cubic $Bi_{13.1}PO_\delta$ phase appears counter-intuitive, because Bi is less electronegative than P with a notably lower tendency towards hydrogen bond formation and Bi_2O_3 exhibits a lower surface acidity than Bi_2WO_6.[67] Nevertheless, phosphorus-rich monoclinic $BiPO_4$ is less suitable for humidity sensing despite its higher surface area and P-content. According to previous works,[48] bismuth phosphate-based sillenites exhibit high permittivity at elevated temperatures. This points to enhanced polarizability of Bi^{3+} in the sillenite framework, which is likely to accelerate the response time to adsorbing water molecules on the surface (cf. also wettability tests in Figure 3.11). The less pronounced humidity sensing behavior reported for sillenite-type γ-Bi_2O_3 films may be due to annealing effects at higher temperature and does not permit a direct comparison to the present investigation.[44]

All in all, the results thus indicate that bismuth oxides can be tuned for humidity sensing through the introduction of moderate phosphorus amounts into the sillenite framework, whilst higher P:Bi ratios are not *per se* more productive. Our previous studies on bismuth oxysulfatenanorods revealed another fruitful sensing combination of Bi^{3+} with tetrahedrally shaped anions (SO_4^{2-}),[34] but detailed follow-up studies are now required to differentiate surface from structural effects. The next step will therefore be the additive controlled optimization[29,30] of our straightforward hydrothermal access to cubic bismuth phosphate in order to generate a variety of particle morphologies with higher surface areas.

3.4 Conclusions

In summary, cubic sillenite-type and monoclinic mozanite-type of bismuth phosphate were obtained via convenient hydrothermal syntheses. Their different structural and morphological motifs give rise to different humidity sensing characteristics. The sensing results demonstrated superior and linear humidity sensing properties of cubic sillenite-type bismuth phosphate over monoclinic $BiPO_4$. Despite the low surface area to volume ratio, the bismuth-richer sillenite modification displayed a promising humidity sensing character in terms of higher sensitivity and quicker response compared with monoclinic bismuth phosphate. The polarizable oxide framework of Bi^{3+} cations with adjacent oxygen atoms probably facilitates formation of hydrophilic OH^- groups, which leads to flexible adsorption of water molecules at high humidity levels. Moreover, the sensing performance of cubic bismuth phosphate for humidity values below 55 % RH is suitable for potential applications, whereas the monoclinic modification showed almost no sensitivity. Therefore, the crystal structure apparently exerts a strong influence on the humidity sensing properties, and the Bi:P ratio plays an important role as well.

All in all, the exploration of new potential application of sillenite-type bismuth phosphate opens up a pathway for developing novel humidity sensors. The results show new strategies to improve and tailor humidity sensing characteristics by using the structural tuning potential of sillenite-type compounds. Along these lines, the low surface area to volume ratio, morphology and particle size of sillenite-type bismuth phosphate are now to be enhanced for better water adsorption. Furthermore, the humidity sensing properties of oxides from the sillenite family can be modified through further doping or variation of their chemical compositions.

Reference

[1] W. S. Wang, A. V. Virkar, *Sens. Actuators B* **2004**, *98*, 282-290.

[2] B. M. Kulwicki, *J. Am. Ceram. Soc.* **1991**, *74*, 697-708.

[3] Z. Chen, C. Lu, *Sensor Lett.* **2005**, *3*, 274-295.

[4] E. Traversa, *Sens. Actuators B* **1995**, *23*, 135-156.

[5] B. Adhikari, S. Majumdar, *Prog. Polym. Sci.* **2004**, *29*, 699-766.

[6] Q. Kuang, C. Lao, Z. L. Wang, Z. Xie, L. Zheng, *J. Am. Chem. Soc.* **2007**, *129*, 6070-6071.

[7] N. Zhang, K. Yu, Z. Zhu, D. Jiang, *Sens. Actuators A* **2008**, *143*, 245-250.

[8] Z. Zhou, C. Zhan, Y. Wang, Y. Su, Z. Yang, Y. Zhang, *Mater. Lett.* **2011**, *65*, 832-835.

[9] X. H. Wang, Y. F. Ding, J. Zhang, Z. Q. Zhu, S. Z. You, S. Q. Chen, J. Z. Zhu, *Sens. Actuators B* **2006**, *115*, 421-427.

[10] H.-S. Hong, D.-T.Phan, G.-S. Chung, *Sens. Actuators B* **2012**, *171*, 1283-1287.

[11] Z. Bai, C. Xie, M. Hu, S. Zhang, D. Zeng, *Mater. Sci. Eng. B.* **2008**, *149*, 12-17.

[12] X. L. Liu, J. P. He, W. J. Dang, Y. J. Ji, G. W. Zhao, C. X. Zhang, *Acta Phys. Chim. Sinica* **2008**, *24*, 475-480.

[13] S. G. Ansari, Z. A. Ansari, M. R. Kadam, R. N. Karekar, R. C. Aiyer, *Sens. Actuators B* **1994**, *21*, 159-163.

[14] H. Yagi, M. Nakata, *J. Ceram. Soc. Jap.* **1992**, *100*, 152-156.

[15] S. B. Wang, C. H. Hsiao, S. J. Chang, K. T. Lam, K. H. Wen, S. J. Young, S. C. Hung, B. R. Huang, *IEEE Sensors J.* **2012**, *12*.

[16] H. T. Hsueh, T. J. Hsueh, S. J. Chang, F. Y. Hung, T. Y. Tsai, W. Y. Weng, C. L. Hsu, B. T. Dai, *Sens. Actuators B* **2011**, *156*, 906-911.

[17] J. Xu, K. Yu, J. Wu, D. Shang, L. Li, Y. e. Xu, Z. Zhu, *J. Phys. D* **2009**, *42*.

[18] C. L. Dai, M. C. Liu, F. S. Chen, C. C. Wu, M. W. Chang, *Sens. Actuators B* **2007**, *123*, 896-901.

[19] Y. F. Dong, L. Y. Li, W. F. Jiang, H. Y. Wang, X. J. Li, *Phys. E* **2009**, *41*, 711.

[20] M. K. Jain, M. C. Bhatnagar, G. L. Sharma, *Jpn. J. Appl. Phys.* **2000**, *39*, 345-350.

[21] M. Su, J. Wang, H. Du, P. Yao, Y. Zheng, X. Li, *Sens. Actuators B* **2012**, *161*, 1038-1045.

[22] K. P. Biju, M. K. Jain, *Sens. Actuators B* **2008**, *128*, 407-413.

[23] Z. Li, H. Zhang, W. Zheng, W. Wang, H. Huang, C. Wang, A. G. MacDiarmid, Y. Wei, *J. Am Chem. Soc.* **2008**, *130*, 5036-5037.

[24] L. Wang, D. Li, R. Wang, Y. He, Q. Qi, Y. Wang, T. Zhang, *Sens. Actuators B* **2008**, *133*, 622-627.

[25] W. Wang, Z. Li, L. Liu, H. Zhang, W. Zheng, Y. Wang, H. Huang, Z. Wang, C. Wang, *Sens. Actuators B* **2009**, *141*, 404-409.

[26] A. Laobuthee, S. Wongkasemjit, E. Traversa, R. M. Laine, *J. Eur. Ceram. Soc.* **2000**, *20*, 91-97.

[27] Z. Wang, L. Shi, F. Wu, S. Yuan, Y. Zhao, M. Zhang, *Sens. Actuators B* **2011**, *158*, 89-96.

[28] R. Sundaram, E. S. Raj, K. S. Nagaraja, *Sens. Actuators B* **2004**, *99*, 350-354.

[29] Y. Zhou, E. Antonova, W. Bensch, G. R. Patzke, *Nanoscale* **2010**, *2*, 2412-2417.

[30] Y. Zhou, K. Vuille, A. Heel, B. Probst, R. Kontic, G. R. Patzke, *Appl. Catal. A* **2010**, *375*, 140-148.

[31] D. Ressnig, R. Kontic, G. R. Patzke, *Mater. Chem. Phys.* **2012**, *135*, 457-466.

[32] R. Kontic, G. R. Patzke, *J. Solid State Chem.***2012**, *189*, 38-48.

[33] K. Zheng, Y. Zhou, L. Gu, X. Mo, G. R. Patzke, G. Chen, *Sens. Actuators B* **2010**, *148*, 240-246.

[34] Y. Zhou, J.-D. Grunwaldt, F. Krumeich, K. Zheng, G. Chen, J. Stoetzel, R. Frahm, G. R. Patzke, *Small* **2010**, *6*, 1173-1179.

[35] M. Valant, D. Suvorov, *Chem. Mater.* **2002**, *14*, 3471-3476.

[36] T. I. Mel'nikova, G. M. Kuz'micheva, V. B. Rybakov, N. B. Bolotina, A. B. Dubovskii, A. Cousson, *J. Struct. Chem.* **2011**, *52*, 510-516.

[37] R. J. Betsch, W. B. White, *Spectrochim. Acta* **1978**, *34*, 505-514.

[38] M. Valant, D. Suvorov, *J. Am. Ceram. Soc.* **2001**, *84*, 2900-2904.

[39] X. Lin, F. Huang, W. Wang, Y. Xia, Y. Wang, M. Liu, J. Shi, *Catal. Commun.* **2008**, *9*, 572-576.

[40] W. F. Yao, H. Wang, X. H. Xu, X. F. Cheng, J. Huang, S. X. Shang, X. N. Yang, M. Wang, *Appl. Catal. A* **2003**, *243*, 185-190.

[41] S. Xu, W. Shangguan, J. Yuan, J. Shi, M. Chen, *Mater. Sci. Eng. B* **2007**, *137*, 108-111.

[42] X. Lin, F. Huang, W. Wang, J. Shi, *Scripta Mater.* **2007**, *56*, 189-192.

[43] B. H. Kim, T. H. Lim, J. W. Roh, S. G. Lee, C. S. Ju, S. S. Park, S. S. Hong, G. D. Lee, *React. Kinet.Mech. Catal.* **2010**, *99*, 217-224.

[44] A. Z. Adamyan, Z. N. Adamian, V. M. Aroutiounian, *Sens. Actuators B* **2003**, *93*, 416.

[45] A. Cabot, A. Marsal, J. Arbiol, J. R. Morante, *Sens. Actuators B* **2004**, *99*, 74-89.

[46] K. Higaki, S. Kudo, H. Ohnishi, *Electrochem.Solid State Lett.* **1998**, *1*, 107-109.

[47] S. S. Sharma, K. Nomura, Y. Ujihira, *J. Appl. Phys.* **1992**, *71*, 2000-2005.

[48] S. L. Lee, C. K. Lee, D. C. Sinclair, *Solid State Ionics* **2005**, *176*, 393-400.

[49] V. P. Zhereb, Y. F. Kargin, L. A. Zhereb, V. A. Mironova, V. M. Skorikov, *Inorg. Mater.* **2003**, *39*, 859-862.

[50] J. P. Wignacourt, M. Drache, P. Conflant, J. C. Boivin,*J. Chem. Phys.* **1991**, 88, 1939.

[51] M. Ruwet, S. Ceckiewicz, B. Delmon, *Ind. Eng. Chem. Res.* **1987**, *26*, 1981-1983.

[52] J. M. D. Tascon, P. Grange, B. Delmon, *J. Catal.***1986**, *97*, 287-299.

[53] J. M. D. Tascon, P. Bertrand, M. Genet, B. Delmon, *J. Catal.***1986**, *97*, 300-311.

[54] J. B. Moffat, *Catal. Rev.-Sci. Eng.* **1978**, *18*, 199-258.

[55] B. Romero, S. Bruque, M. A. G. Aranda, J. E. Iglesias, *Inorg. Chem.* **1994**, *33*, 1869-1874.

[56] R. C. L. Mooney-Slater, *Z. Kristallogr.***1962**, 117, 371.

[57] M. Yang, N. K. Shrestha, R. Hahn, P. Schmuki, *Electrochem. Solid State Lett.* **2010**, *13*, C5.

[58] J. Geng, W. H. Hou, Y. N. Lv, J. J. Zhu, H. Y. Chen, *Inorg. Chem.* **2005**, *44*, 8503.

[59] M. Kaelin, D. Rudmann, A. N. Tiwari, *Solar Energy* **2004**, *77*, 749.

[60] Y. Li, M. J. Yang, *Sens. Actuators B* **2002**, *85*, 73.

[61] Y. Zhang, X. Zheng, T. Zhang, L. Gong, S. Dai, Y. Chen, *Sens. Actuators B* **2010**, *147*, 180.

[62] T. Yang, D. Xia, *J.Cryst.Growth* **2009**, *311*, 4505.

[63] Y. Li, M. J. Yang, Y.She, *Talanta* **2004**, *62*, 707.

[64] E. Traversa, A. Bearzotti, M. Miyayama, H. Yanagida, *Sens. Actuators B* **1995**, *25*, 714.

[65] C. D. Feng, S. L. Sun, H. Wang, C. U. Segre, J. R. Stetter, *Sens. Actuators B* **1997**, *40*, 217.

[66] Q. Wang, Y. Z. Pan, S. S. Huang, S. T. Ren, P. Li, J. J. Li, *Nanotechnol.* **2011**, *22*.

[67] T. Saison, N. Chemin, C. Chaneac, O. Durupthy, V. Ruaux, L. Mariey, F. Mauge, P. Beaunier, J. P. Jolivet, *J. Phys. Chem. C* **2011**, *115*, 5657.

Part II

Molybdenum-based Materials for Gas Sensing Applications

4. Nanostructured MoO_3/SnO_2 heterojunctions for hydrogen gas sensing

4.1 Introduction

One-dimensional nanostructured transition metal oxides (TMOs) have attracted increasing interest for sensing devices due to their variety of morphologies such as nanobelts,[1,2] nanorods,[3-5] nanowires[6,7] and nanofibers.[8] A wide variety of applications of one-dimensional nanostructured compounds has been described, including gas sensors,[9-11] photocatalysts[12,13] and solar cells.[14-16] 1D metal-oxide nanostructures have several advantages with respect to large surface-area-to-volume ratio, enhanced mobility of electrons and the interaction of target gas molecules on the surface.[17] The morphological properties and surface states play a crucial role in gas sensing properties.[18,19]

Molybdenum oxides consist of a network of MoO_6 octahedra or MoO_4 tetrahedra with shared oxygen atoms at the corners.[20] The family of molybdenum oxides has a variety of crystalline phases including orthorhombic MoO_3 (α-MoO_3),[21,22] metastable monoclinic MoO_3 (β-MoO_3)[23,24] and hexagonal MoO_3 (h-MoO_3).[25,26] Among them, α-MoO_3 is the most attractive functional material due to its unique physical/chemical properties and manifold potential applications, such as in the fields of photocatalysts[27-30] and gas sensing materials.[31-35] Different systems have been investigated with respect to enhancement of gas sensing properties, e.g. Ti-MoO_3,[36,37] Ta-MoO_3[38] and SnO_2/MoO_3.[39-42] Among these modified systems, SnO_2/MoO_3 nanocomposites have been previously studied with respect to Mo-doping effects on the gas sensing characteristics of SnO_2/MoO_3 binary systems with SnO_2 as the main component (cf. Table 4.1). To the best of our knowledge, SnO_2/MoO_3 systems with orthorhombic α-MoO_3 as the main phase have never been investigated as hydrogen sensors. This leaves room for the exploration of new types of SnO_2/MoO_3 combinations.

Table 4.1. Overview of morphology and gas sensing properties of sensors based on SnO_2/MoO_3 systems.

System	Morphology	Target gas	Ref.
SnO_2/α-MoO_3 mixture SnO_2/β- MoO_3 mixture	nanoparticles	NH_3, $C_nH_{2n+1}OH$ (n=1-4)	[24]
α-MoO_3 on SnO_2 thin films	nanostructures	NO_2	[25]
SnO_2/h-MoO_3	hallow nanostructures	ethanol	[26]
SnO_2/α-MoO_3	nano- and meso-porous	NO_2, H_2, ethanol	[27]
SnO_2/α-MoO_3	nanoparticles	CO, H_2	[28]
SnO_2/α-MoO_3	nanoparticles	$C_nH_{2n+1}OH$ (n=1-4)	[29]

The gas sensing properties of pure one-dimensional α-MoO_3 towards reducing gases, such as H_2S and ethanol were studied by other research groups.[43 - 45] Moreover, gas sensing characteristics of 1D-TMOs in combination with quantum dots were investigated with respect to to their potential applications. Although the sensing performance of quantum dots, such as SnO_2 and ZnO, towards diverse target gases has been studied,[46-49] their structural stability performance under operational conditions still remain critical issues for applications. However, the small size in range of 3 – 5 nm, which causes phase transformations at very low temperature, renders quantum dots less favorable candidates for sensing applications.[50] Therefore, stable heterostructures of 1D-TMOs in combination with quantum dots open up new and easily accessible routes and methods to enhance the sensing characteristics.[17,51,52] As reported by *Tvdry* et al.,[53] electron transfer rates can be enhanced on heterostructures between TMOs and QDs. This opens up new possibilities for sensor construction.

Alone these lines, we report here a novel combination of heterostructural one-dimensional TMO and quantum dots into a gas sensing composite material. The MoO_3 nanofibers and SnO_2 quantum dots were synthesized via convenient hydrothermal routes. In the following, the as-synthesized MoO_3 nanofibers were coated with SnO_2 quantum dots via wet chemical treatment. The MoO_3/SnO_2 nanocomposites exhibit promising improvement of hydrogen sensing performance and reduced operating temperature compared to pristine MoO_3 nanofibers.

4.2 Experimental section

4.2.1 Synthetic techniques

For the synthesis of MoO_3 fibers, 2 mmol commercial Mo powder was quantitatively dissolved in 2 mL 30% H_2O_2.[54] The resulting orange-colored solution was transferred to a Teflon-lined autoclave and maintained at 120 °C for 24 h. The product was centrifuged, washed with DI H_2O and dried at 80 °C in air. Next, SnO_2 quantum dots were prepared according to literature protocols[55] by dissolving 2 mmol $SnCl_4 \cdot 5H_2O$ in DI H_2O, followed by addition of 10 mmol lysine dissolved in DI H_2O. The mixture was stirred for 12 h at room temperature and transferred into a Teflon-lined autoclave. Hydrothermal treatment was maintained for 12 h at 240 °C. The quantum dots were centrifuged, washed with DI H_2O and ethanol, and dried at 80 °C in air. MoO_3 fibers and SnO_2 quantum dots were mixed in a 2:1 ratio (weight) and stirred in ethanol for 10 min. The final composite product was obtained after centrifugation and dried at 85 °C for 1 h to remove residual ethanol.

4.2.2 Sensor fabrication and gas sensing measurements

Gas sensing measurements were carried out by monitoring resistance changes of the coated MoO_3 belts during exposure to target gas in a home-made test chamber. An interdigital finger electrode was used as substrate for the fibers. The quartz substrate with a size of 2 mm x 2 mm was manufactured in clean room facilities (FIRST at ETHZ) with photolithography techniques. A bilayer of 10 nm titanium and 200 nm gold was deposited by evaporation on the electrode surface which was patterned with a finger distance of 25 µm.

Scheme 1. Fabrication of interdigital finger electrodes.

The MoO_3/SnO_2 composite was mixed with DI water to form a dispersion. This dispersion was subsequently placed on the electrode to form a thin sensing film with a thickness of about

10 µm. The electrode was transferred to a heating plate, which was controlled by an external temperature regulator in the test chamber and aged at 350 °C for 240 h under continuous introduction of dry synthetic air. The electrode was connected via cables with a sourcemeter (Keithley 2400), which was used for recording resistance changes with a recording rate of 1 data point/sec. Low concentrations of target gas in synthetic dry air were introduced through two flowmeters, which were controlled by a computerized gas calibration system. A constant flow speed of 500 sccm was applied for all gas sensing measurements.

4.3 Analytical characterization

All samples were characterized by powder X-ray diffraction (PXRD) on a STOE STADI P diffractometer in transmission mode (flat sample holders, Ge monochromator and Cu $K_{\alpha 1}$ radiation) operated at 40 kV and 40 mA. Scanning electrode microscopy (SEM) images were obtained with a Zeiss SUPRA 50 VP microscope operated at 2 keV with samples dispersed in ethanol and deposited on a silicon wafer, subsequently. Transmission electron microscopy (TEM) was performed on a Tecnai F 30 ST (FEG, 300 kV, SuperTwin lens). In the scanning TEM (STEM) mode, the electron beam was placed in a selected area and an elemental analysis by EDXS (EDAX detector) was performed.

The sensing temperature was set in the range from 200 to 300 °C and increased in steps of 25 °C. The optimal operating temperature was determined from tests against 200 ppm H_2. The gas response S is defined as $S=(R_{air}-R_{gas})/R_{gas}$, where the R_{air} and R_{gas} represented resistance in air and target gas, respectively.

4.4 Results and discussion

4.4.1 Structural and morphological analysis

The PXRD pattern as shown in Figure 4.1 can be indexed to the tetragonal crystal structure of SnO_2 (JCPDS No. 41-1445) and no further impurities were observed. The calculated lattice parameters (a = b = 4.731(5) Å and c = 3.179(4) Å) agree well with literature data. The broad diffraction peaks indicate the small particle size of the final product, which is also evident from SEM and TEM images (cf. Figs. 3 and 4). The PXRD pattern of MoO_3 nanostructured fibers with lattice constants of a=13.855(9) Å, b=3.675(2) Å and c=3.933(2) Å agrees well with reference data for orthorhombic molybdenum oxide (JCPDS No. 05-0508).

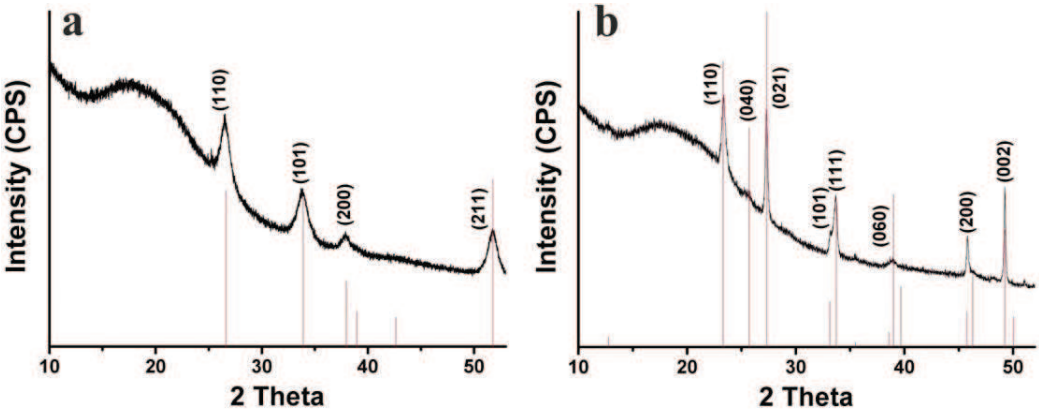

Figure 4.1. XRD patterns of (a) as-synthesized SnO_2 quantum dots and (b) MoO_3 fibers.

Furthermore, the PXRD pattern of the MoO_3/SnO_2 composites is compared to the pristine MoO_3 precursor in Figure 4.2. All characteristic peaks of orthorhombic molybdenum oxide are retained after the coating process, which indicates that the MoO_3 precursor remains structurally intact. In particular, the intensity of the strong (110), (021), (111), (200) and (002) MoO_3 reflections decreases in the heterostructure, thus indicating a slight loss of crystallinity after the coating process. The absence of characteristic reflections of SnO_2 quantum dots indicates a low degree of coating as shown in electron microscopy images of the composites (cf. below).

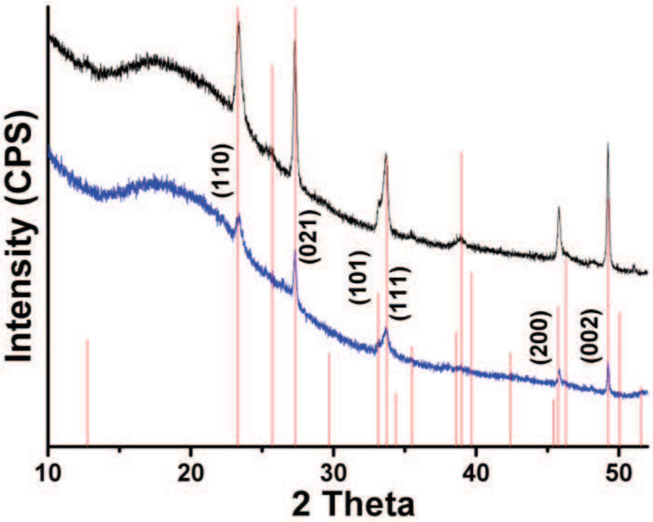

Figure 4.2. PXRD patterns of MoO_3 rods (black) compared to MoO_3/SnO_2 composites (blue).

The average crystallite size of SnO_2 quantum dots (6 nm) and their uniform diameter are evident from HRTEM images (Figure 4.3 a), and the results are in line with calculated particle sizes from the Scherrer equation according to *Wu* et al.[55] TEM images furthermore display the characteristic lattice fringes of SnO_2 with a constant lattice spacing of 0.321 nm, which corresponds to the (110) plane. This indicates the high crystallinity of the as-synthesized quantum dots.

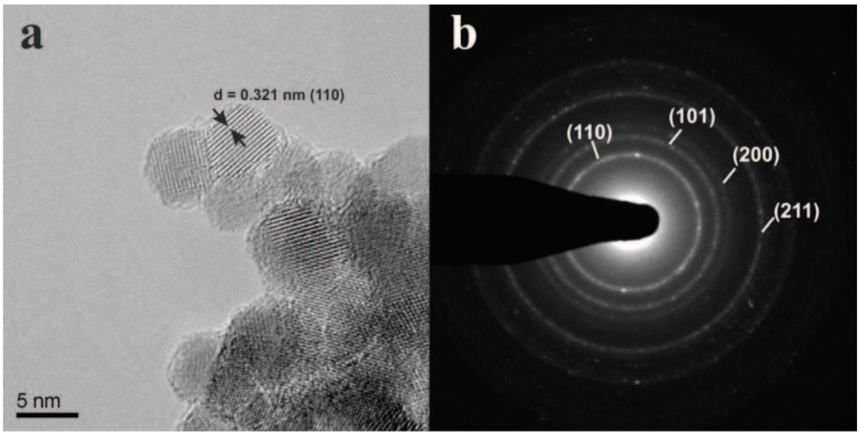

Figure 4.3. (a) Representative TEM image of SnO_2 quantum dots; (b) HRTEM image of SnO_2 quantum dots.

SEM images of as-synthesized MoO_3 fibers and SnO_2-QD coated MoO_3 fibers are compared in Figures 4.4 a and b. The MoO_3 substrates display uniform widths around 200 – 300 nm and lengths in the 7 – 10 µm range, and these dimensions are maintained after the coating process with SnO_2 quantum dots. The light spots (Figure 4.4 b) indicate the presence of oxide clusters on the MoO_3 fibers.

TEM images of pristine and coated MoO_3 samples are shown in Figures 4.4 c and d. Figure 4.4 d demonstrates that the MoO_3 fibers are partially coated with SnO_2 quantum dots on their prolate and oblate faces. Although agglomeration of the quantum dots on the oxide surface leads to an inhomogeneous distribution, the morphologies of both precursors do not change substantially. The inset of Figure 4.4 d shows a more detailed view of the MoO_3/SnO_2 heterojunction, and the presence of both Mo and Sn in the MoO_3/SnO_2 heteostructures was confirmed with EDX measurements (Figure 4.5).

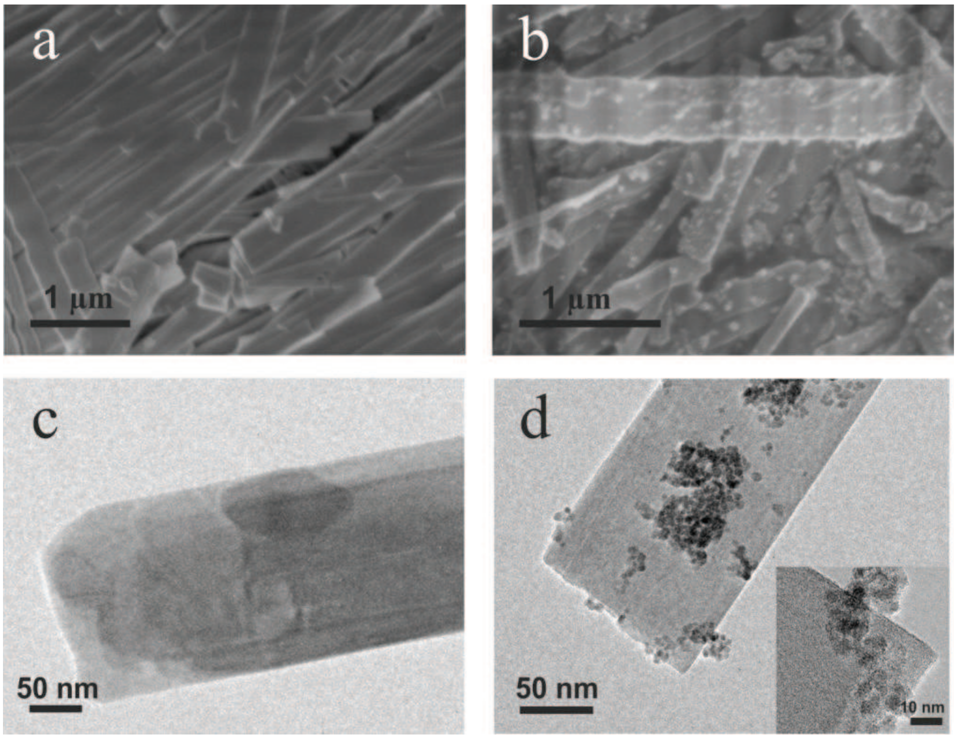

Figure 4.4. Top: representative SEM images of (a) MoO_3 fibers and (b) SnO_2-QD/MoO_3 composites. Bottom: TEM images of (c) pristine and (d) coated MoO_3 fibers.

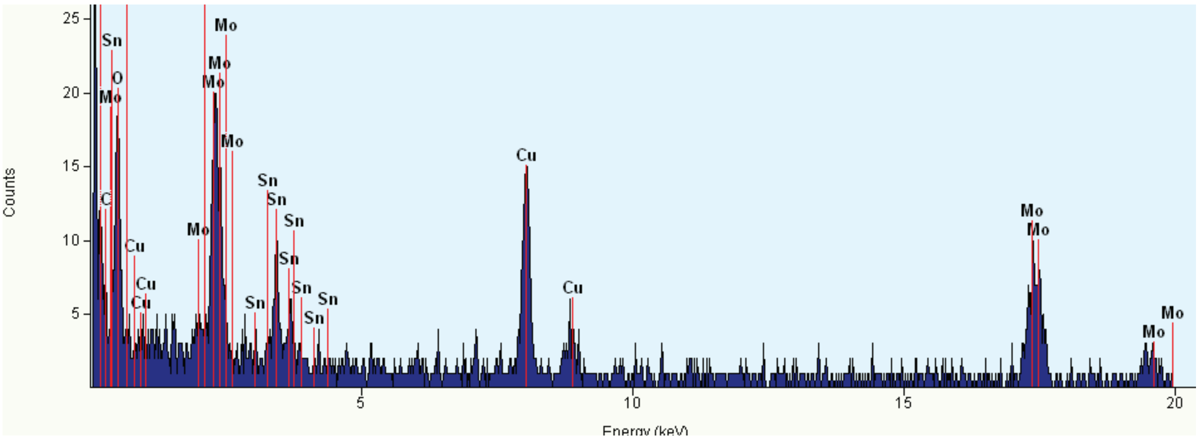

Figure 4.5. EDX spectrum of MoO_3/SnO_2 heterostructures (Cu signals are due to the TEM grids).

4.4.2 Gas sensing properties

The gas sensing response towards hydrogen of as-synthesized MoO_3 fibers and of their SnO_2 coated composites was investigated in the temperature range from 200 to 325 °C. The concentration of hydrogen was fixed at 200 ppm and the temperature was increased in steps of 25 °C. Both sensor materials showed typical n-type sensing behavior. As shown in Figure 4.6, the optimal working temperature of as-synthesized MoO_3 fibers was found to be 300 °C with a rather poor sensitivity value of 0.134. In contrast, the coated sample showed a considerably enhanced response value of 0.453 at a lower working temperature of 250 °C. This indicates that the coating process not only enhances the sensitivity of the gas response, but also decreases the operating temperature. This is in line with preceding reports on higher sensitivity and reduced working temperature of various sensor materials after coating with nanoparticles.[46,56]

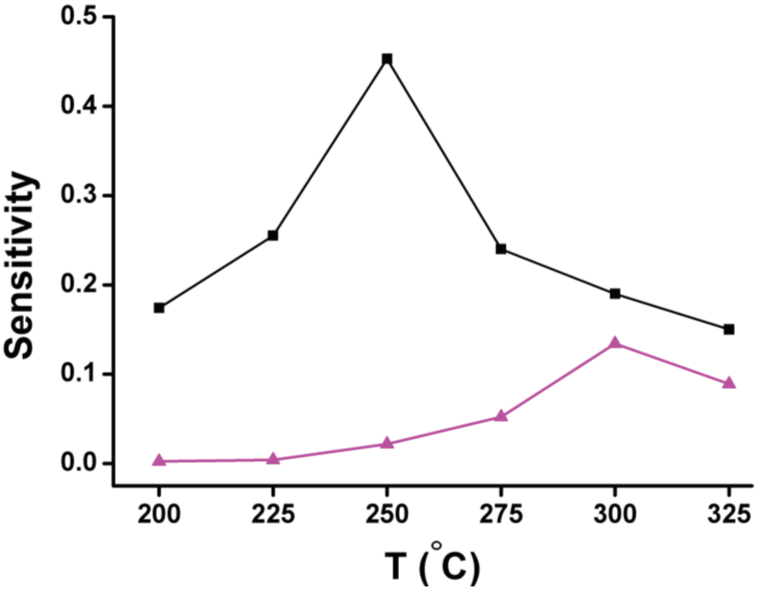

Figure 4.6. Gas response of MoO_3 rods (violet triangles) and their MoO_3/SnO_2 composites (black squares) towards 200 ppm H_2 over the temperature range from 200 °C to 325 °C.

Next, the response of MoO_3/SnO_2 composites towards different concentrations of hydrogen at the optimized working temperature of 250 °C was studied. Figure 4.7 shows the dynamic response curve towards increasing hydrogen concentrations of 50 ppm, 100 ppm, 150 ppm and 200 ppm. In addition to the dynamic response study on various concentrations of hydrogen, the reproducibility of the response and recovery process towards higher hydrogen concentrations of 150 and 200 ppm was investigated. The sensitivity values towards 150 ppm and 200 ppm hydrogen are reproducible and stable. Both cycles afford closely related response values of S = 0.37 and 0.45. It is well known, that recovery processes after exposure to high concentrations of target gases are often prolonged.[57] As can be seen from Figure 4.7, the heterostructure-based sensors display reliable and quick recovery characteristics. After 5 min of exposure to 200 ppm hydrogen, the recovery curve reached the baseline within 15 min.

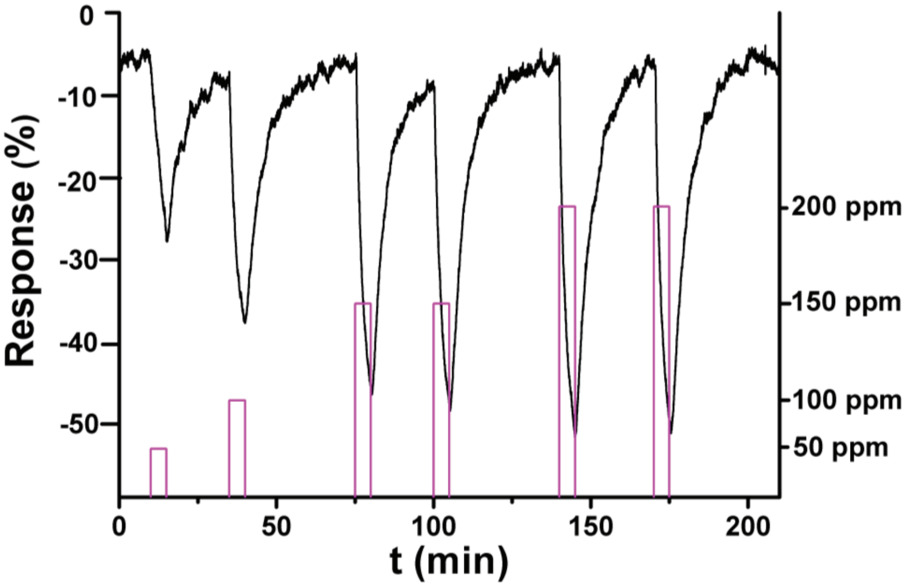

Figure 4.7. Dynamic resistance/response curves of SnO_2-coated MoO_3 towards 50 ppm, 100 ppm, 150 ppm and 200 ppm H_2 at the optimal operating temperature of 250 °C.

Response and test gas concentration are correlated in Figure 4.8, which illustrates the relationship between the sensitivity values (cf. Figure 4.7) and the respective H_2 concentrations. The observed linear relationship over a wide range of hydrogen concentrations points to promising calibration properties for technical applications of MoO_3/SnO_2 composites.

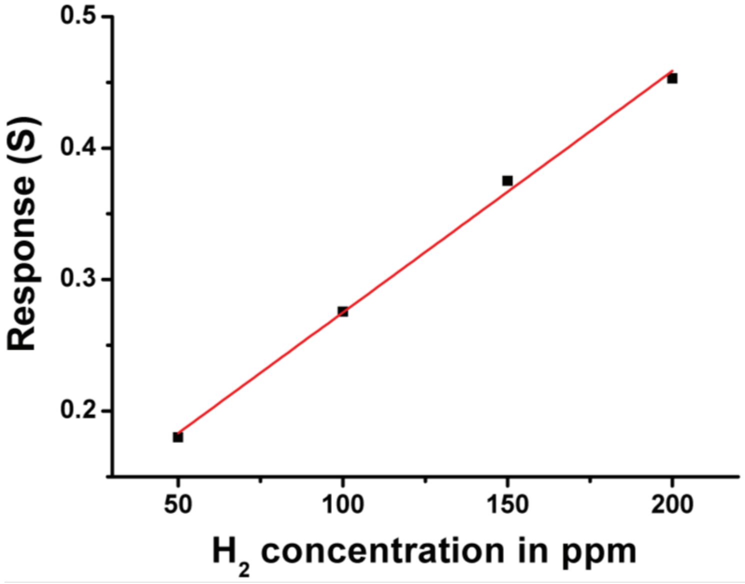

Figure 4.8. Linear relationship between gas sensing response of sample B and hydrogen in different concentrations (expressed as y = 1.09125 + 0.00184 x; correlation coefficient R = 0.99613).

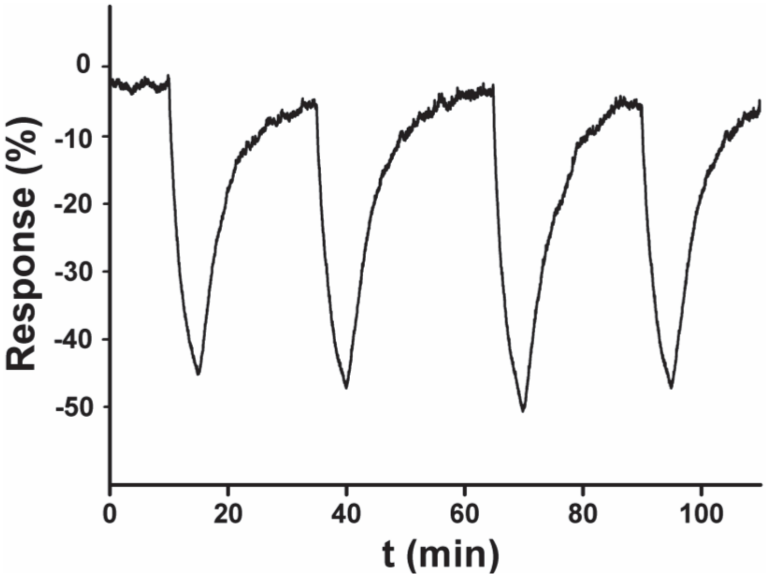

Figure 4.9. Reproducible and stable sensing tests of SnO_2-coated MoO_3 towards 200 ppm H_2 at the optimal operating temperature of 250 °C.

4.4.3 Mechanistic hypotheses

Mechanisms of chemical gas sensing offer models for the conductivity change during the interaction of the active target gas with the sensor surface.[58] During exposure to air, oxygen molecules are adsorbed on the surface of semiconductors where they form oxygen species, which are required for the subsequent sensing reactions. Depending on the working temperature, O_2^- is formed below 100 °C in an ionosoption process, while O^- and O^{2-} are formed at higher temperatures, respectively.[3] Upon exposure to a reducing target gas, oxygen adsorbates of an n-type semiconductor react with the target gas molecules and release electrons to the surface of the semiconductor. This electron transfer process is recorded as sensor signal. In the present investigation of gas sensing with MoO_3/SnO_2 heterostructures, their enhanced gas sensing performance and reduced working temperature are most likely due to the increased amount of oxygen species on SnO_2 quantum dots. Several research groups have reported on related phenomena among nanoscale composites.[59-61] All these results indicate that coating or doping of nanocomposites are highly efficient strategies to improve the gas sensing sensitivity while lowering the working temperature.

Generally, orthorhombic MoO_3 has been investigated for hydrogen sensing, and it shows a rather moderate response in different morphologies (cf. Table 4.2). In the present work, however, phase pure orthorhombic molybdenum oxide fibers exhibit promising hydrogen sensing activity compared with other hydrogen sensors based on α-MoO_3.

Table 4.2 Selected hydrogen sensors based on orthorhombic α-MoO_3.

Morphology	Minimal detected concentration (ppm)	T (°C)	Response (%)	Ref.
nanofibers	**50**	**300**	**18**	**This work**
lamellar	600	225	11	[62]
microstructured	10	350	2	[63]
thin films	100	300	1	[64]
nanoplatelets, nanowires, nanoflowers	600	170 - 250	< 10	[65]

We propose that the sensing properties are drastically enhanced after the coating process due to the formation of a depletion layer between the interface of SnO_2 quantum dots and MoO_3 nanostructured composites (Figure 4.9). Generally, a surface depletion layer with increasing amount of absorbed oxygen species leads to kinetics change of surface.[66] Both metal oxides are typical n-type semiconductors, but SnO_2 has a lower work function (4.5 eV)[67] than α-MoO_3 (5.3 eV),[68] which facilitates the generation of oxygen species on the surface at moderate temperatures. This can well account for the reduced operating temperature after the coating process. The difference of work functions results in the creation of a Schottky barrier, which can accelerate the mobility of electrons in depletion regions at the interface.[52] Moreover, the formed depletion layer is capable of producing a larger amount of oxygen species, which in turn enhances the gas sensing characteristics.[69] A possible mechanism is proposed as follows (cf. Figure 4.10) with the first step:

$$H_{2(ads)} + O^{-}_{(surface)} \rightarrow H_2O + e^{-} \qquad \text{Eq. (4.1)}$$

Hydrogen molecules react with oxygen species, which are formed through dissociative processes on the surface of SnO_2 quantum dots. The released electrons are transferred via the depletion region into the conduction band of MoO_3 nanostructured composites, resulting in an overall increase of conductivity. In summary, the interaction of H_2 with the SnO_2 surface is promoted due to the lower work function of the QDs, and the depletion layer between SnO_2 and MoO_3 accelerates the electron transport.

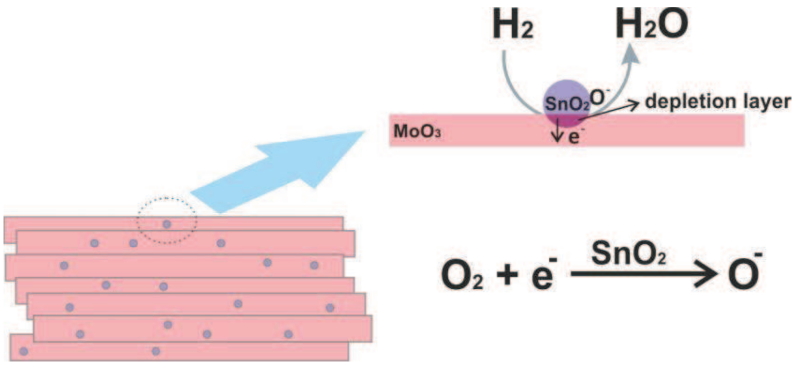

Figure 4.10. Schematic representation of the MoO_3/SnO_2 heterostructure sensor during exposure to hydrogen.

4.5 Conclusions

In summary, we have synthesized the MoO_3 fibers (ca. 200 nm wide, lengths up to 10 μm) and SnO_2 quantum dots (uniform size of 6 nm) via convenient hydrothermal routes. The combination of both n-type semiconducting oxides into belt-shaped MoO_3/SnO_2 nanocomposites was achieved via facile preparative routes. Phase purity of orthorhombic MoO_3 was confirmed by XRD and formation a MoO_3-SnO_2 heterojunction was characterized with SEM and TEM investigations. Compared with pristine MoO_3 nanofibers, the mixed nanocomposites exhibited a significant 3-fold increase in maximum sensitivity and reduced operating temperature in the gas sensing performance measurements towards hydrogen. The linear response/concentration correlation indicates a high reliability of the sensing properties and renders SnO_2-coated MoO_3 nanocompounds promising hydrogen sensors for future applications. The SnO_2 quantum dots with lower work function probably led to the improved surface interaction with hydrogen, and the formation of a depletion layer between MoO_3 belts and SnO_2 QDs accomplished the rapid electron transport at the interface. All in all, the facile combination of 1D transition metal oxides with oxide QDs is an elegant approach to optimize the performance of this low-cost and robust class of sensor materials.

References

---

[1] E. Comini, G. Faglia, G. Sberveglieri, L. Zanotti, *Mater. Manuf. Processes* **2006**, *21*, 229.

[2] E. Comini, G. Faglia, G. Sberveglieri, Z. W. Pan, Z. L. Wang, *Appl. Phys. Lett.* **2002**, *81*, 1869.

[3] S. L. Bai, K. W. Zhang, R. X. Luo, D. Q. Li, A. F. Chen, C. C. Liu, *J. Mater. Chem.* **2012**, *22*, 12643.

[4] A. M. Taurino, A. Forleo, L. Francioso, P. Siciliano, M. Stalder, R. Nesper, *Appl. Phys. Lett.* **2006**, *88*.

[5] H. Li, J. Du, J. Q. Xu, X. W. Dong, Q. Y. Pan, *Sens. Lett.* **2011**, *9*, 170.

[6] M. L. Zhong, D. C. Zeng, Z. W. Liu, H. Y. Yu, X. C. Zhong, W. Q. Qiu, *Acta Mater.* **2010**, *58*, 5926.

[7] D. Zhang, S. K. Lee, S. Chava, C. A. Berven, V. Katkanant, *Phys. B* **2011**, *406*, 3768.

[8] G. Wang, Y. Ji, X. Huang, X. Yang, P.-I. Gouma, M. Dudley, *J. Phys. Chem. B* **2006**, *110*, 23777.

[9] A. Kolmakov, M. Moskovits, *Annu. Rev. Mater. Res.* **2004**, *34*, 151.

[10] M. M. Arafat, B. Dinan, S. A. Akbar, A. S. M. A. Haseeb, *Sensors* **2012**, *12*, 7207.

[11] E. Comini, C. Baratto, G. Faglia, M. Ferroni, A. Vomiero, G. Sberveglieri, *Prog. Mater. Sci.* **2009**, *54*, 1.

[12] Z. R. Tang, Y. H. Zhang, Y. J. Xu, *RSC Advances* **2011**, *1*, 1772.

[13] X. L. Bai, N. Pan, X. P. Wang, H. Q. Wang, *Chin. J. Chem. Phys.* **2008**, *21*, 81.

[14] L. E. Greene, B. D. Yuhas, M. Law, D. Zitoun, P. Yang, *Inorg. Chem.* **2006**, *45*, 7535.

[15] A. M. Peiro, P. Ravirajan, K. Govender, D. S. Boyle, P. O'Brien, D. D. C. Bradley, J. Nelson, J. R. Durrant, *J. Mater. Chem.* **2006**, *16*, 2088.

[16] K. Zhu, T. B. Vinzant, N. R. Neale, A. J. Frank, *Nano Lett.* **2007**, *7*, 3739.

[17] W. Zeng, T. Liu, Z. Wang, *J. Mater. Chem.* **2012**, *22*, 3544.

[18] G. Korotcenkov, *Mater. Sci. Eng. R* **2008**, *61*, 1.

[19] C. H. Wang, X. F. Chu, M. W. Wu, *Sens. Actuators B* **2006**, *113*, 320.

[20] P. A. Spevack, N. S. McIntyre, *J. Phys. Chem.* **1993**, *97*, 11020.

[21] G. Andersson, A. Magneli, *Acta Chem. Scand.* **1950,** 4, 793-797.

[22] G. A. Nazri, C. Julien, *Solid State Ionics* **1992,** 53, 376-382.

[23] E. M. McCarron, *J. Chem. Soc. Chem. Commun.* **1986**, 336-338.

[24] M. Figlarz, *Prog. Solid State Chem.***1989,** 19, 1-46.

[25] E. M. McCarron, D. M. Thomas, J. C. Calabrese, *Inorg.Chem.***1987,** 26, 370-73.

[26] T. P. Feist, P. K. Davies, *Chem. Mater.***1991,** 3, 1011-1012.

[27] D. L. Chen, M. N. Liu, L. Yin, T. Li, Z. Yang, X. J. Li, B. B. Fan, H. L. Wang, R. Zhang, Z. X. Li, H. L. Xu, H. X. Lu, D. Y. Yang, J. Sun, L. Gao, *J. Mater. Chem.* **2011**, *21*, 9332.

[28] M. J. Hwang, S. W. Han, T. B. Nguyen, S. C. Hong, K. S. Ryu, *J. Nanosci. Nanotechnol.* **2012**, *12*, 5884.

[29] Y. M. He, T. L. Sheng, Y. Wu, J. S. Chen, R. B. A. Fu, S. M. Hu, X. T. Wu, *J. Hazard. Mater.* **2009**, *168*, 551.

[30] I. Shakir, J. H. Choi, M. Shahid, Z. Ali, D. J. Kang, *J. Mater. Chem.* **2012**, *22*, 20549.

[31] A. M. Azad, *Sens. Actuators B* **2006**, *120*, 25.

[32] A. K. Prasad, P. I. Gouma, D. J. Kubinski, J. H. Visser, R. E. Soltis, P. J. Schmitz, *Thin Solid Films* **2003**, *436*, 46.

[33] H. M. Martinez, J. Torres, M. E. Rodriguez-Garcia, L. D. L. Carreno, *Phys. B* **2012**, *407*, 3199.

[34] W. S. Kim, H. C. Kim, S. H. Hong, *J. Nanopart. Res.* **2010**, *12*, 1889.

[35] M. Ferroni, V. Guidi, G. Martinelli, P. Nelli, M. Sacerdoti, G. Sberveglieri, *Thin Solid Films* **1997**, *307*, 148.

[36] C. Imawan, F. Solzbacher, H. Steffes, E. Obermeier, *Sens. Actuators B* **2000**, *64*, 193.

[37] V. Guidi, D. Boscarino, L. Casarotto, E. Comini, M. Ferroni, G. Martinelli, G. Sberveglieri, *Sens. Actuators B* **2001**, *77*, 555.

[38] O. Merdrignac-Conanec, P. T. Moseley, *Electrochem. Commun.* **1999**, *1*, 51.
[39] J. Arbiol, J. R. Morante, P. Bouvier, T. Pagnier, E. A. Makeeva, M. N. Rumvantseva, A. M. Gaskov, *Sens. Actuators B* **2006**, *118*, 156.
[40] J. Kaur, V. D. Vankar, M. C. Bhatnagar, *Sens. Actuators B* **2008**, *133*, 650.
[41] A. A. Firooz, A. R. Mahjoub, A. A. Khodadadi, *J. Nanosci. Nanotechnol.* **2010**, *10*, 6155.
[42] A. A. Firooz, T. Hyodo, A. R. Mahjoub, A. A. Khodadadi, Y. Shimizu, *Sens. Actuators B* **2010**, *147*, 554.
[43] T. S. Wang, Q. S. Wang, C. L. Zhu, Q. Y. Ouyang, L. H. Qi, C. Y. Li, G. Xiao, P. Gao, Y. J. Chen, *Sens. Actuators B* **2012**, *171*, 256.
[44] Y. J. Chen, G. Xiao, T. S. Wang, F. Zhang, Y. Ma, P. Gao, C. L. Zhu, E. Zhang, Z. Xu, Q.H. Li, *Sens. Actuators B* **2011**, *156*, 867.
[45] L. L. Xing, S. Yuan, Z. H. Chen, Y. J. Chen, X. Y. Xue, *Nanotechnol.* **2011**, *22*.
[46] X. Xu, J. Zhuang, X. Wang, *J. Am. Chem. Soc.* **2008**, *130*, 12527.
[47] D. Q. Li, J. W. Hu, F. Y. Fan, S. L. Bai, R. X. Luo, A. F. Chen, C. C. Liu, *J. Alloys Compd.* **2012**, *539*, 205.
[48] A. Forleo, L. Francioso, S. Capone, P. Siciliano, P. Lommens, Z. Hens, *Sens. Actuators B* **2010**, *146*, 111.
[49] S. M. Sedghi, Y. Mortazavi, A. Khodadadi, *Sens. Actuators B* **2010**, *145*, 7.
[50] G. Korotcenkov, B. K. Cho, *Sens. Actuators B* **2011**, *156*, 527.
[51] H. Huang, H. Gong, C. L. Chow, J. Guo, T. J. White, M. S. Tse, O. K. Tan, *Adv. Funct. Mater.* **2011**, *21*, 2680.
[52] J. Zhai, L. Wang, D. Wang, H. Li, Y. Zhang, D. Q. He, T. Xie, *Appl. Mater. Interfaces* **2011**, *3*, 2253.
[53] K. Tvrdy, P. A. Frantsuzov, P. V. Kamat, *Proc. Natl. Acad. Sci. USA* **2011**, *108*, 29.
[54] X. K. Hu, Y. T. Qian, Z. T. Song, J. R. Huang, R. Cao, J. Q. Xiao, *Chem. Mater.* **2008**, *20*, 1527-1533.
[55] S. Wu, H. Cao, S. Yin, X. Liu, X. Zhang, *J. Phys. Chem. C* **2009**, *113*, 17893-17898.
[56] M. H. Cao, Y. D. Wang, T. Chen, M. Antonietti, M. Niederberger, *Chem. Mater.* **2008**, *20*, 5781-5786.
[57] A. Chowdhuri, V. Gupta, K. Sreenivas, R. Kumar, S. Mozumdar, P. K. Patanjali, *Appl. Phys. Lett.* **2004**, *84*, 1180-1182.
[58] H. Meixner, U. Lampe, *Sens. Actuators B* **1996**, *33*, 198-202.
[59] J. M. Wu, *Nanotechnol.* **2010**, *21*.
[60] C. Li, L. Li, Z. Du, H. Yu, Y. Xiang, Y. Li, Y. Cai, T. Wang, *Nanotechnol.* **2008**, *19*.
[61] D. Buso, M. Post, C. Cantalini, P. Mulvaney, A. Martucci, *Adv. Funct. Mater.* **2008**, *18*, 3843-3849.
[62] M. B. Rahmani, S. H. Keshmiri, J. Yu, A. Z. Sadek, L. Al-Mashat, A. Moafi, K. Latham, Y. X. Li, W. Wlodarski, K. Kalantar-zadeh, *Sens. Actuators B* **2010**, *145*, 13-19.

[63] S. S. Sunu, E. Prabhu, V. Jayaraman, K. I. Gnanasekar, T. K. Seshagiri, T. Gnanasekaran, *Sens. Actuators B* **2004**, *101*, 161-174.

[64] C. Imawan, H. Steffes, F. Solzbacher, E. Obermeier, *Sens. Actuators B* **2001**, *78*, 119-125.

[65] M. Shafiei, J. Yu, M. Breedon, N. Motta, Q. Wu, Z. Hu, L. Qian, K. Kalantar-Zadeh, W. Wlodarski, IEEE, *Hydrogen Gas Sensors Based On Thermally Evaporated Nanostructured MoO3 Schottky Diode: A Comparative Study*, IEEE, New York, **2011**.

[66] Y. J. Chen, G. Xiao, T. S. Wang, F. Zhang, Y. Ma, P. Gao, C. L. Zhu, E. Zhang, Z. Xu, Q. H. Li, *Sens. Actuators B* **2011**, *156*, 867-874.

[67] M. Kwoka, L. Ottaviano, J. Szuber, *Appl. Surf. Sci.* **2012**, *258*, 8425-8429.

[68] V. Shrotriya, G. Li, Y. Yao, C. W. Chu, Y. Yang, *Appl. Phys. Lett.* **2006**, *88*.

[69] N. Yamazoe, *Sens. Actuators B* **1991**, *5*, 7-19.

5. Synthetic and Structural Tuning of Hexagonal Molybdenum Oxide for Ammonia Sensing

5.1 Introduction

Molybdenum oxide is one of the most attractive semiconducting transition metal oxides in device technology due to its versatile structures, unique physical/electronic properties and flexible chemical redox activity.[1-3] A wide variety of potential applications of molybdenum oxide including (photo)catalysts,[4,5] sensors,[6-10] electro-/photochromic devices[11] and Li-ion batteries[12,13] renders it a promising advanced functional material. The family of molybdenum oxide contains three main structure types: thermally stable orthorhombic MoO_3 (α-MoO_3) built of MoO_6 octahedra sharing edges,[14,15] metastable monoclinic MoO_3 (β-MoO_3) with corner-sharing MoO_6 octahedra,[16,17] and hexagonal MoO_3 (h-MoO_3) with edge-sharing MoO_6 octahedra connected through the *cis*-position.[18,19] Among them, hexagonal molybdenum trioxide has been a controversial and rather elusive target of intense structural investigations for more than 100 years due to its unique tunnel motif.[20,21] This channel structure gives rise to a flexible intercalation chemistry with interesting electrochemical and catalytic properties.[22-24] Moreover, the channel formation is required to be stabilized by incorporating large cations with a certain mobility, such as NH_4, Ag and alkali cations[25-28] in the tunnel via a variety of synthetic routes.[29-31] Therefore, the open channels of h-MoO_3 can only be accessed in pure form with special "chimie douce" redox processes.[22] The incorporation of guest cations leads to ternary hexagonal molybdenum oxides with enhanced electronic, catalytic and surface properties.[32-35] Unlike orthorhombic α-MoO_3, which has long been considered as a promising candidate for sensing applications,[36-39] the sensing properties of hexagonal molybdate still remain to be fully explored.[40]

In our previous work, the NH_3 sensing properties of alkali-containing (alkali = Li, Na, K, Rb and NH_4) hexagonal W/Mo-oxides with related channel structures indicated promising sensing performance and application potential. Hexagonal Rb-containing W/Mo-oxide with enhanced thermal stability and a special hierarchical morphology exhibited higher ammonia sensing performance compared with other alkali containing analogues.[41] Generally, the presence of alkali cations is essential as stabilizing components against phase transformation and sintering effects[42] during many crystallization processes of transition metal oxides.[43,44] However, potassium cations, which have the critical size to support the hierarchically structured morphology,[45] play a transitory role in the series of hexagonal W/Mo-oxides with respect to the hydrothermal transformation into nanorods.[46] Moreover, the catalytic properties of molybdenum-based oxides, such as ethane oxidation and oxidative dehydrogenation of propane, can be improved by incorporating potassium cations.[47,48] Therefore, tuneable morphologies and surface properties of potassium-containing hexagonal molybdates are interesting for gas sensing applications. Optimization of oxide sensing materials is a complex interplay of a variety of factors, such as high surface-area-to-volume ratio, chemical/thermal stability, structural, electronic and morphological properties[49-51] as well as minimal power consumption/weight.

Starting from a convenient hydrothermal approach towards potassium-stabilized hexagonal molybdenum oxide rods, the particle size and surface-area-to-volume ratio are controlled and optimized for gas sensing applications, respectively. The multi-functional potassium additive gives rise to structure-directing and morphology-controlling oxide formation in combination with tuneable gas sensing properties. First, we discuss the straightforward transformation of elemental Mo as a precursor into h-K-MoO_3 rods and the influence of variable KCl quantities on the morphology control. In the following, the interplay of particle size, chemical composition and surface properties with respect to the sensor performance is discussed on the way to guidelines for oxide sensor development. Finally, the sensing results of h-K-MoO_3 based ammonia sensors are compared to previous studies on orthorhombic MoO_3.

5.2 Experimental section

5.2.1 Synthetic techniques

In a typical experiment, Mo powder (Fluka AG, >99.7 %, 1 mmol) was stirred in 2 mL 30% H_2O_2 at RT until quantitative dissolution was achieved. Afterwards, according molar quantities of KCl were added to the solution and dissolved in the reaction mixture, followed by transfer into a Teflon-lined stainless steel autoclave. Hydrothermal treatment was performed for 24 h at 180 °C. The final products were collected through centrifugation, washed with DI water and dried in air at 80 °C.

5.2.2 Sensor fabrication and gas sensing measurements

Interdigital finger electrodes were manufactured in cleanroom facilities (FIRST at ETH Zurich) by photolithography techniques. A 2 mm x 2 mm quartz substrate was cut and cleaned with acetone, isopropanol and DI water. The electrode pattern was fabricated on top of the substrate with a finger distance of 25 µm. A bilayer of 10 nm titanium and 200 nm gold was deposited by evaporation.

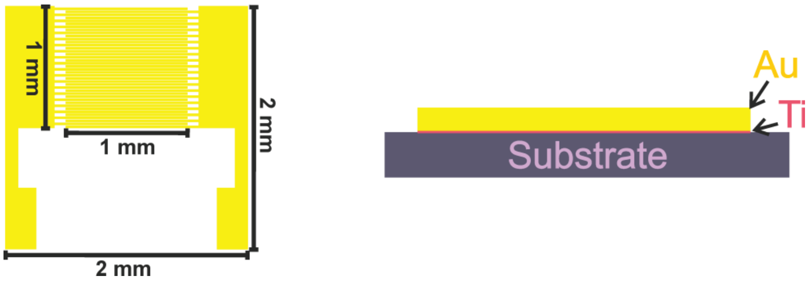

Scheme 1. Fabrication of interdigital finger electrodes.

h-K-MoO_3 rods were mixed with DI water in an ultrasonic bath to form dispersions, which were subsequently put on the electrodes to form a thin sensing film with a thickness of about 10 µm. Gas sensing properties were investigated in a specially constructed and sealed test chamber with gas inlet and outlet. Electrodes with samples were fixed on heating plates in the test chamber where measurement temperatures were controlled with an external temperature regulator. Time-dependent resistances were recorded with a sourcemeter (Keithley 2400) which was connected directly to the sample. Target gases were mixed with synthetic dry air as carrier gas, and the respective concentrations were adjusted with flowmeters (Bronkhorst) via a computerized gas calibration system. The total flow speed was kept constant at 500 sccm for all measurements. Prior to gas sensing experiments, each sample was aged at 300 °C for 240 h under continuous introduction of dry synthetic air. Sensing was investigated in the temperature range from 150 to 275 °C with increments of 25 °C. Operating temperatures for each sample were optimized through individual tests with 100 ppm NH_3. Gas response S is defined as $S = R_{air} / R_{gas}$, where R_{air} and R_{gas} represent resistance in air and target gas, respectively.

5.2.3 Analytical characterization

All samples were characterized with powder X-ray diffraction (PXRD) on a STOE STADI P diffractometer in transmission mode (flat sample holders, Ge monochromator and Cu $K_{\alpha 1}$ radiation) operated at 40 kV and 40 mA. Scanning electron microscopy (SEM) analyses were carried out on a Zeiss SUPRA 50 VP microscope (3 keV). Samples were dispersed in ethanol and subsequently deposited on a silicon wafer. Transmission electron microscope (TEM) investigations were performed on a field emission electron microscope (Tecnai F30, FEG, SuperTwin lens), operated at 300 kV. Brunauer-Emmett-Teller (BET) surface areas were determined on a Quantachrome Quadrasorb SI in N_2-adsorption mode. All samples were degassed at 150 °C for > 5 h *in vacuo* prior to nitrogen adsorption measurements. X-ray photoelectron spectroscopy (XPS) was performed in a Quantum 2000 from Physical Electronics. Powders were prepared from DI water suspension on glass slides, which were left to dry in an over at 200 °C. The XPS instrument was operated with monochromatized Al K_{α}, a pass energy of 29.35 eV with a step size of 0.125 eV, the operating pressure was about $2 \cdot 10^{-7}$ Pa. The resolution of the spectrometer at that pass energy is characterized by the full width at half maximum of the Ag $3d_{5/2}$ peak, which amounts to 0.86 eV. In order to minimize alterations of the spectra due to electrostatic charging, measurements were performed while the samples were exposed to low energy electrons of ca. 2.5 eV and Ar^+ ions of about 1 eV. This neutralization procedure allowed to record spectra with charging differences below 1 eV among all measured samples. To allow for comparison among the samples, the binding energy scale was referenced to the C 1s peak at 284.8 eV. Since carbon is alien to the samples, its origin has to be ascribed to adventitious carbon as a reference. Both the irregular surface of the investigated powders as well as the sensitivity of MoO_3 to sputter reduction damages precluded the use of sputter cleaning procedures. Evaluation of the spectra was performed using Physical Electronics' software package Multipak (v. 8.2). Fit procedures were performed on background-subtracted spectra (Shirley); the spectra of Mo and K were fitted with fixed intensity ratios (Mo: 0.67; K: 0.5) and constant energy separation ($Mo3d_{5/2}$-$Mo3d_{3/2}$) and K $2p_{3/2}$-$2p_{1/2}$). Additionally, elemental analyses were performed by Mikroanalytisches Labor Pascher, Remagen, Germany.

5.3 Results and discussion

5.3.1 Structural and morphological characterization

In order to select the most suitable alkali additive cation for the h-MoO_3 host structure and to investigate its influence on the gas sensing characteristics systematically, h-MoO_3 samples were screened with NaCl, KCl, RbCl and CsCl as additives in a certain molar ratio (alkali/Mo = 1.5:1). Preliminary gas sensing tests were carried out at 225 °C towards 100 ppm NH_3, and h-K-MoO_3 exhibited the highest sensitivity among the series. Therefore, we explored the favorable morphology directing and stabilizing potential of K^+ as host cation in the hexagonal framework for sensor development (further details cf. introduction). PXRD patterns of as-synthesized h-K-MoO_3 samples with increasing potassium contents (samples A – E) are summarized in Figure 5.1. All patterns can be indexed to the phase pure hexagonal (h-MoO_3) structure and agree well with literature data (PDF 48-0399). Increasing amounts of KCl additive did not affect the phase purity of the obtained products.

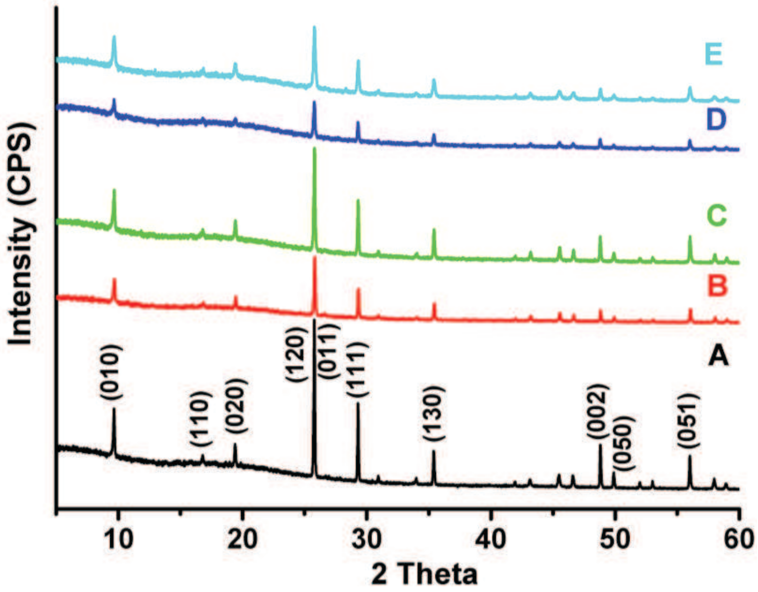

Figure 5.1. XRD patterns of as-synthesized molybdenum oxides (cf. Table 5.1 for sample compositions).

Table 5.1 provides a survey of lattice constants and sample compositions with increasing potassium content. Potassium incorporation into the hexagonal molybdate channels is facilitated through notable KCl excess in the precursor mixture. The first detailed crystallographic characterization of $KMo_5O_{15}OH{\cdot}2H_2O$ (h-K-MoO_3) was performed by Krebs et al. in 1975.[52] In the present study, the K/Mo ratio (0.19) of sample C is most closely related to the above literature value of 0.2, whilst samples A and B display a lower extent of potassium incorporation.

Table 5.1. Molar K/Mo ratios, lattice constants and rod diameters of h-K-MoO$_3$ samples A – E.

	A	**B**	**C**	**D**	**E**
Mo (mg)	96	96	96	96	96
KCl (mg)	74.5	112	149	223.5	372.5
K:Mo (precursor)	1:1	1.5:1	2:1	3:1	5:1
K:Mo (samples)	0.17:1	0.18:1	0.19:1	0.20:1	0.21:1
a (Å)	10.5195(3)	10.5266(3)	10.5345(2)	10.5450(4)	10.5402(4)
c (Å)	3.72489(7)	3.72633(8)	3.72747(8)	3.73012(16)	3.7293(3)
V (Å^3)	356.975(14)	357.592(16)	358.238 (13)	359.21(3)	358.81(5)
average diameter	12 µm	350 nm	230 nm	150 nm	65 nm

The molar K/Mo ratios in h-K-MoO$_3$ samples are clearly related to the initial molar K/Mo ratios in the precursors (Figure 5.2). Samples A to D with lower potassium contents display an almost linear increase, whereas in sample E the reported saturation level of K$^+$ incorporation into the host framework (K/Mo = 0.2) has indeed been approached.

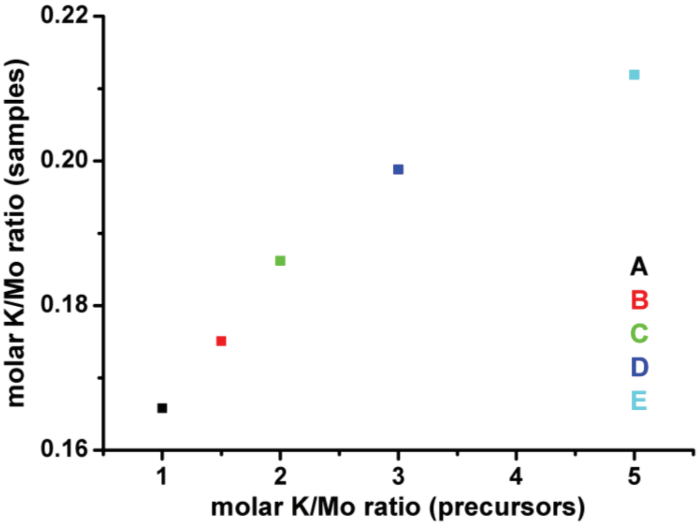

Figure 5.2. Precursor K/Mo molar ratios vs. K/Mo molar ratios in the as-synthesized samples (values derived from elemental analyses).

Morphological characteristics of h-K-MoO_3 rods were investigated with scanning electron microscopy (SEM) and high resolution transmission electron microscopy (HRTEM). SEM images (Figure 5.3) illustrate the characteristic hexagonal morphology of all samples. The rod size decreases from sample A (Figure 5.3 a) to sample E while the extent of potassium incorporation increases (Figure 5.3 i and Table 5.2). Sample A is consisting of microscale particles in the 7 – 20 µm range (cf. Figure 5.3 a), while samples B and C are in the submicron regime with diameters around 350 and 250 nm, respectively (cf. Figure 5.3 c and e). The potassium-richest samples D and E among the series consist of thinner rods with diameters of 150 nm and 50 – 70 nm, respectively (cf. Figure 5.3 g and i). Furthermore, sample E with the highest potassium content in the series exhibits the narrowest particle size distribution, i.e. the highest degree of uniformity (FWHM 15 nm) (cf. Figure 5.4 e). This trend is in line with previous reports on notable size and morphology directing effects of alkali cations.[46] Furthermore, increasing alkali concentrations have been reported to reduce the solubility of the oxide precursor.[53] This effect might also account for the significant decrease of particle size in the presence of large initial KCl excesses. The size-controlling effect of K^+ on molybdate formation[54] is particularly evident from the average diameters of the h-K-MoO_3 nanorods (cf. Figure 5.4 f). Samples B – E are in the same size range and their diameters practically display a linear dependence on the K/Mo contents, thereby pointing out the efficiency of additives in fine-tuning of morphological dimensions.[55-58]

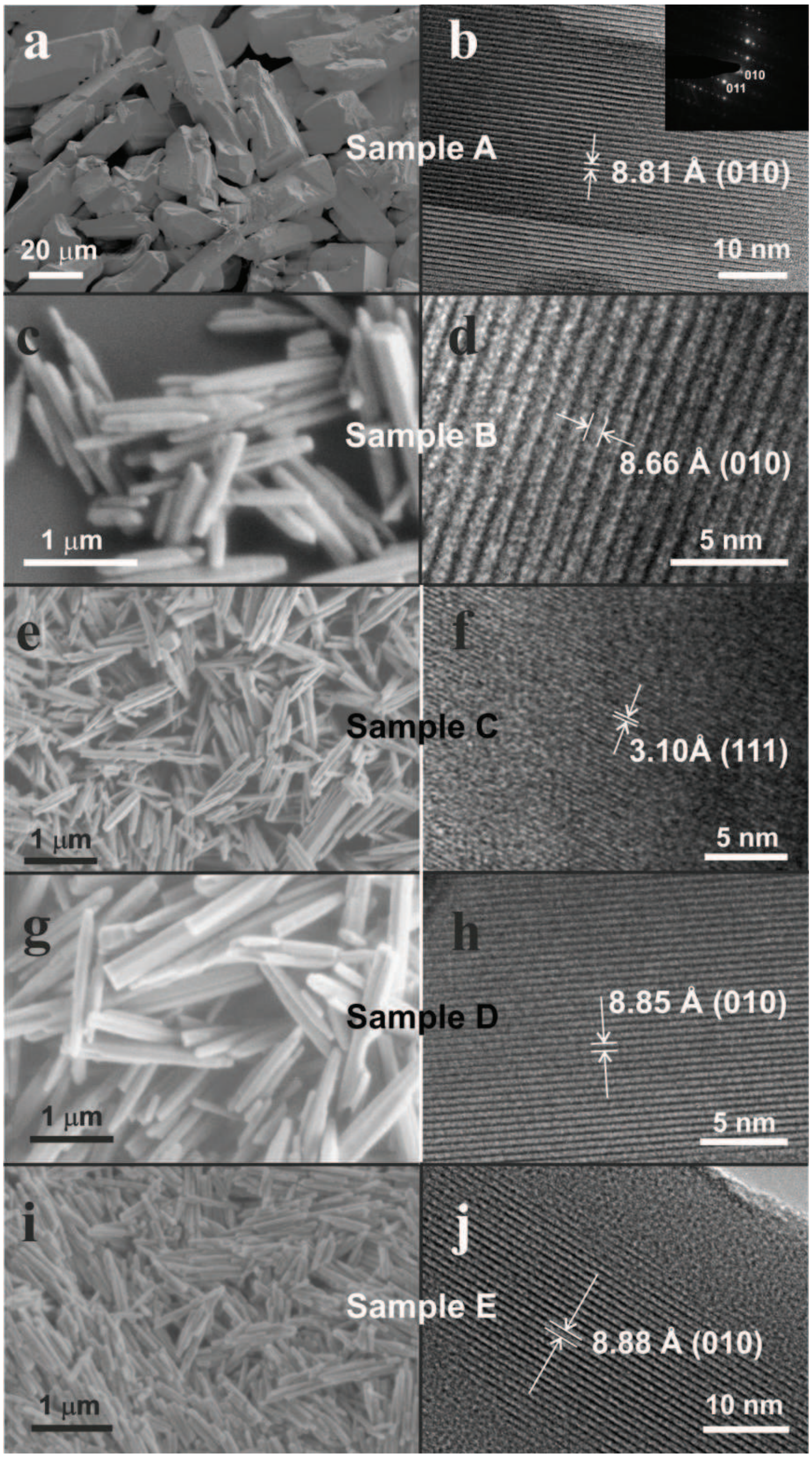

Figure 5.3. SEM and HRTEM images of h-K-MoO$_3$ rods (samples A – E).

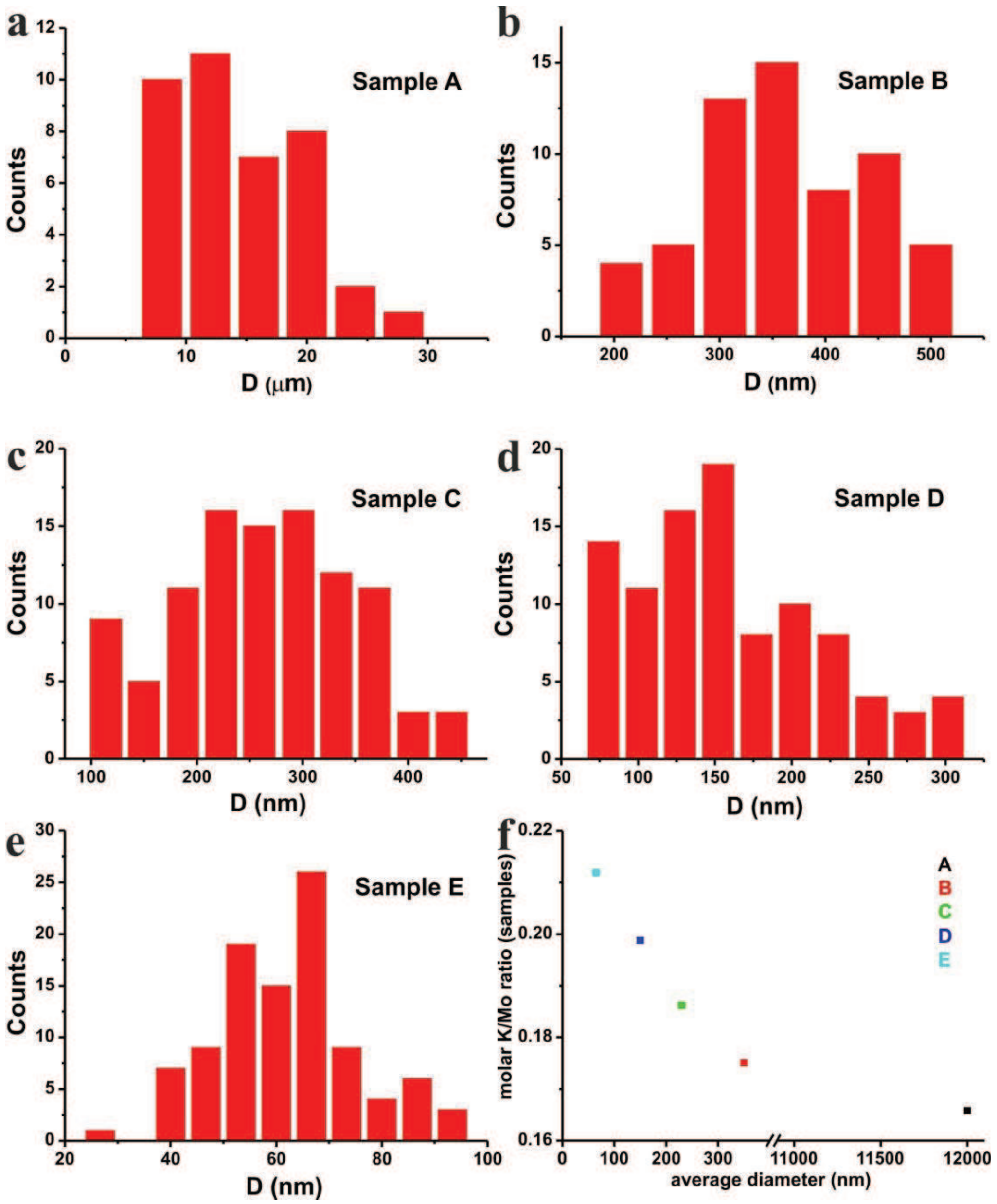

Figure 5.4. (a) – (e) Particle size distribution of h-K-MoO3 (samples A – E); (f) K/Mo ratios of h-K-MoO_3 nanorods vs. average diameters.

Furthermore, samples A – E were investigated with XPS spectroscopy, and their Mo $3d_{3/2}$ and Mo $3d_{5/2}$ peaks are shown in Figure 5.5 a – c. The Mo 3d XPS spectrum of sample A differs considerably from the closely related spectra of samples B – E. Therefore, fits for sample A (Figure 5.5 b) are compared to sample E as a representative example (Figure 5.5 c). The asymmetric shape of the Mo 3d peaks (Figure 5.5 a) cannot be represented by a single chemical species, which indicates that the Mo $3d_{5/2}$ peak consists of an overlay of Mo^{6+} and

Mo^{5+} (characteristic values around 232.3 eV and 231.1 eV, respectively) as well as the Mo $3d_{3/2}$ peak (ca. 235.5 and 234.2 eV).[59] The full width at half maximum of 1.25 eV allows for a clear distinction between chemically different states (Figure 5.5 a). For sample A with large microscale particles, the energy difference between the fitted Mo^{6+} and Mo^{5+} peaks amounts to 1.2 eV (Figure 5.5 b), which is in accordance with most reports.[60,61] As the size of h-K-MoO_3 nanorods shrinks, the Mo^{6+}/Mo^{5+} peak energy separation increases and reaches 1.42 eV for the sample E with the smallest particle diameters (Figure 5.5 c). The increasing energy difference between the Mo^{6+} and Mo^{5+} peaks from sample A to sample E points to a more pronounced charge difference between fully oxidized Mo^{6+} centers and the partially reduced Mo^{5+} atoms (cf. Figure 5.6). Another striking difference is the ratio of Mo^{5+} to that of Mo^{6+}, which is uniform among samples B through E (ca. 0.1), but is decisively different for sample A (ca. 0.7). Since the values for sample A differ drastically from those of the samples B – E, this phenomenon is most probably related to the parallel decrease in particle size. The high Mo^{5+}/Mo^{6+} ratio of sample A (large particle size) is accompanied by very high fractions of OH contributions (OH/bulk oxide ca. 0.9), while the smaller samples B – E contain only minute amounts of OH (OH/bulk oxide ca. 0.03), as determined from the O 1s spectra shown in Figures 5.5e and f. In the case of other oxide sensors, such as nanostructured ZnO, the density of surface oxygen defects has been observed to increase with decreasing sample diameter. The smaller particle size of samples B – E could thus be a possible explanation for their increasing extent of Mo reduction towards $Mo^{(5-\delta)+}$ compared to sample A.[62]

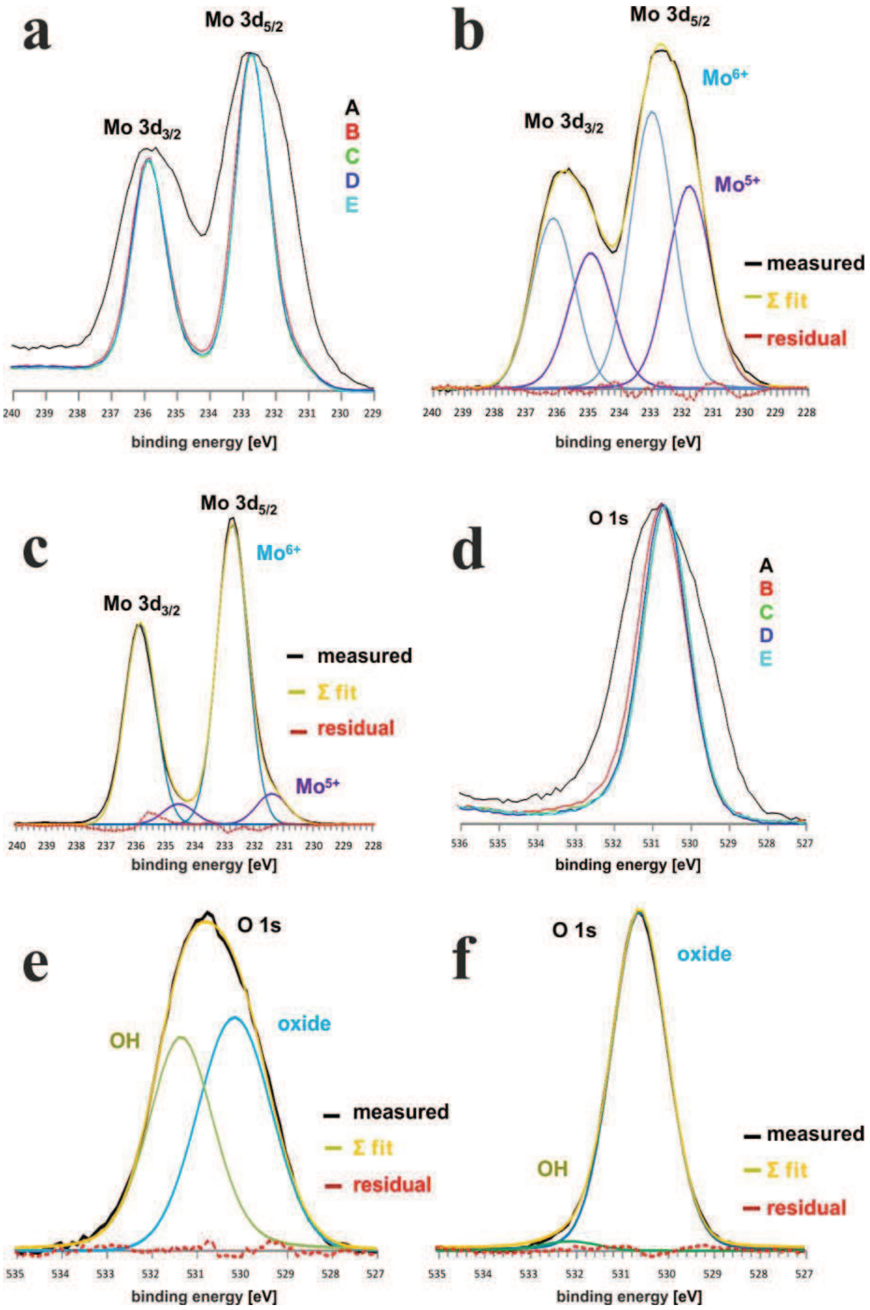

Figure 5.5. (a) Intensity-normalized Mo 3d XPS spectra for as-synthesized h-K-MoO_3 nanorods; (b) peak fitting of Mo 3d for sample A; (c) peak fitting of Mo 3d for sample E (representative example); (d) intensity-normalized O 1s XPS spectra for as-synthesized h-K-MoO_3 nanorods; (e) peak fitting of O 1s for sample A; (c) peak fitting of O 1s for sample E.

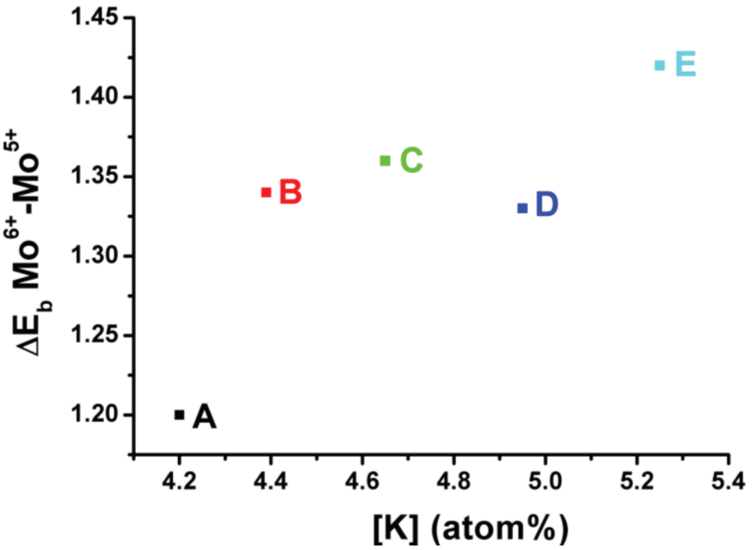

Figure 5.6. Peak energy differences between Mo^{6+} and reduced Mo centers for samples A – E.

5.3.2 Gas sensing properties

Molybdenum oxide is a typical n-type semiconductor so that the resistance of h-K-MoO_3 sensors decreases upon reaction with ammonia. Generally, the operating temperature for a given sensor depends on the test gas. Sensitivity is defined as $S = R_{air} / R_{gas}$, where R_{air} and R_{gas} represent sensor resistances towards air and target gas, respectively. Optimal operating temperatures for all samples were evaluated through recording the gas response towards 100 ppm NH_3 in dry synthetic air at 150, 175, 200, 225, 250 and 275 °C. Responses of all sensors towards 100 ppm NH_3 over the above temperature range are compared in Figure 5.7. As outlined above, they are defined as the ratio between R_{air} / R_{NH_3} , with R_{air} and R_{NH_3} representing the resistance of the sensor in dry air or during exposure to 100 ppm NH_3, respectively. Samples A and B display optimal operating temperatures around 225 °C in the given ammonia sensing setup. Sensors made from samples C – E show an increasing response up to 200 °C which rapidly decreases upon further elevated temperatures. Therefore, operating temperatures were fixed at 225 °C for samples A – B and at 200 °C for samples C – E. As a consequence, higher potassium contents in the hexagonal molybdate framework and smaller rod diameters together with increasing BET surface areas lead to lower operating temperatures. This trend demonstrates the strong influence of KCl additive amounts on both morphology and ammonia sensing behavior. Table 5.2 sums up these characteristics together with gas responses at the respective optimized operating temperatures. These values confirm the above trend: samples A and B with lower potassium contents and larger particle sizes reach maximal response values of 2.2 and 13.0 at 225 °C, respectively. The response of the potassium-enriched samples C – E with smaller particle sizes significantly increases to 39.1, 41.4 and 148 at 200 °C, respectively. This steep increase clearly illustrates the correlation between chemical composition, morphology and sensing properties.

Table 5.2. Surface areas, maximal gas responses and operating temperatures of h-K-MoO_3 sensors.

	A	B	C	D	E
Mo/K ratio (molar)	1:0.17	1:0.18	1:0.19	1:0.20	1:0.21
BET surface area (m^2/g)	3.11	4.38	5.64	6.77	14.99
Maximal response / S_{max}	2.22	13.02	39.11	41.43	148
Operating temperature (°C)	225	225	200	200	200

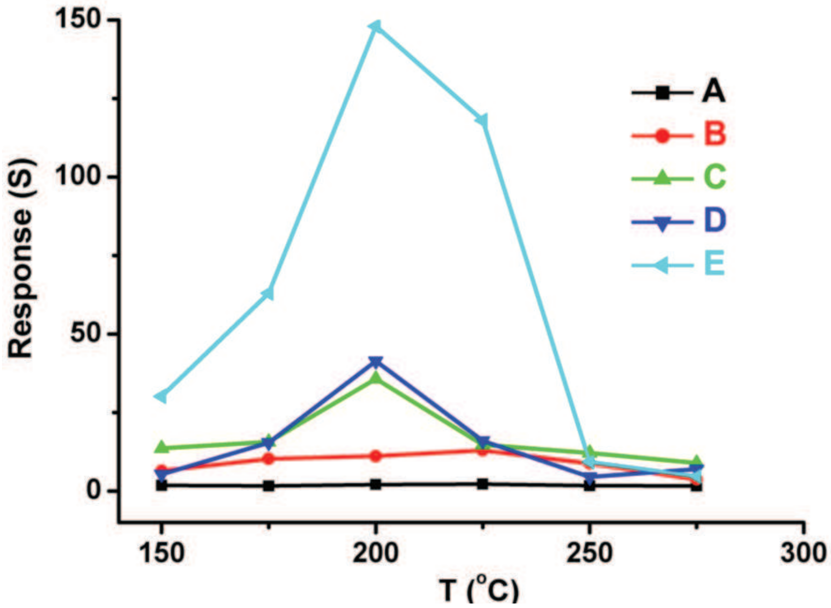

Figure 5.7. Response of h-K-MoO_3 sensors towards 100 ppm NH_3 over the temperature range from 150°C to 275 °C.

Detailed investigations of ammonia sensing properties were conducted for samples B – E and sample A was excluded due to its low response (cf. Figure 5.7). Dynamic resistance/response curves display the characteristic n-type sensing behavior, namely a sharp resistance decrease upon introduction of NH_3 into the test chamber, followed by return to the baseline value upon stopped ammonia flow. h-K-MoO_3 based sensors display stable response signals and complete recovery after removal of NH_3. A representative dynamic response curve at 225 °C for sample B towards ammonia from 2 ppm, 5 ppm, 10 ppm, 20 ppm, 50 ppm to 100 ppm is shown in Figure 5.8 a. Due to fast gas response the minimum resistance was reached within seconds of ammonia exposure. The dynamic response curve of sample C shows that this trend continues at a lower operating temperature of 200 °C (Figure 5.8 b). Interestingly, sample C responds more strongly towards NH_3 than sample B, and the respective response values are compared in Table 5.4.

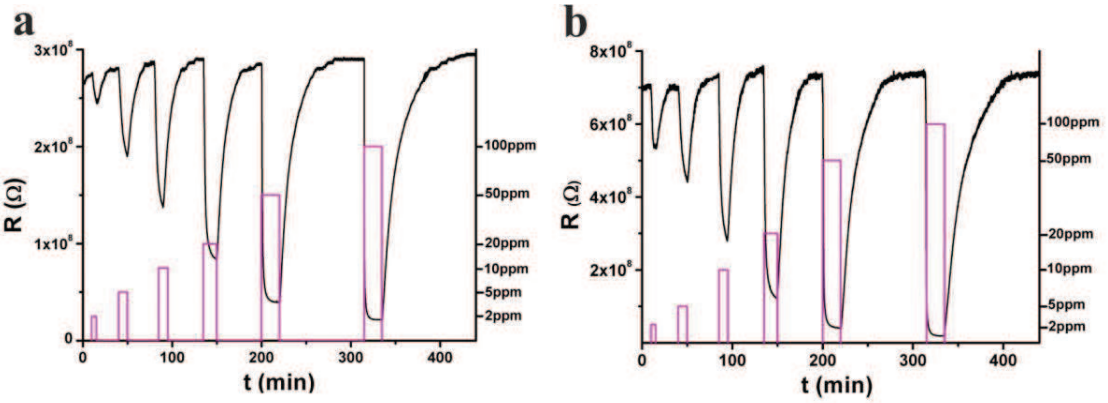

Figure 5.8. Dynamic resistance response curves of (a) sample B at 225 °C and (b) sample C at 200 °C towards 2 ppm, 5 ppm, 10 ppm, 20 ppm, 50 ppm and 100 ppm NH_3.

Table 5.3. Sensitivity values of samples B (225 °C) and sample C (200 °C) towards different NH_3 concentrations.

	2 ppm	5 ppm	10 ppm	20 ppm	50 ppm	100 ppm
Sample B	1.13	1.48	2.09	3.35	6.92	13.02
Sample C	1.31	1.59	2.61	6.20	18.11	39.11

Furthermore, the relationship between response values and ammonia concentrations was studied for the 2 – 100 ppm range, and the values for samples B and C are compared in Table 5.3. Most importantly for future applications, both samples exhibit a linear relationship between response and NH_3 concentration as shown in Figure 5.9.

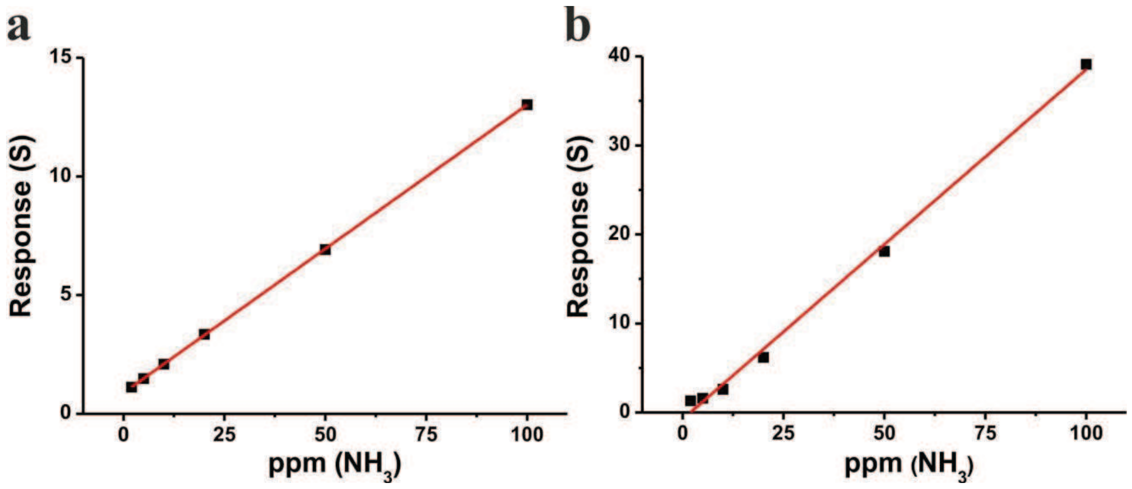

Figure 5.9. Linear relationships between gas response of B (left) and C (right) vs. NH_3 concentration (linear expression for B: $y = 0.12128x + 0.88732$, correlation coefficient $R = 0.99997$; linear expression for C: $y = 0.39276x - 0.7542$, $R = 0.99569$).

The selectivity of the h-K-MoO_3 sensors towards NH_3 was investigated through tests against other reducing gases, namely hydrogen (100 ppm), isopropanol (500 ppm), ethanol (500 ppm), methanol (1000 ppm), acetone (1000 ppm) and carbon monoxide (100 ppm). Tests were conducted at 225 °C for sample B and at 200 °C for sample C. Both sensors excelled through a high response towards ammonia in comparison with negligible activity in the presence of other reducing test gases. The response change of sample B towards all other gases was below 1.09, compared to an ammonia response of 13.0. Likewise, ammonia response of sample C reached values up to 39.1, while hydrogen induced a response change of 4.38 and all other test gases led to responses below 1.75. This clearly outlines the remarkably high selectivity of h-K-MoO_3 based sensors towards ammonia as a promising prerequisite for technical applications.

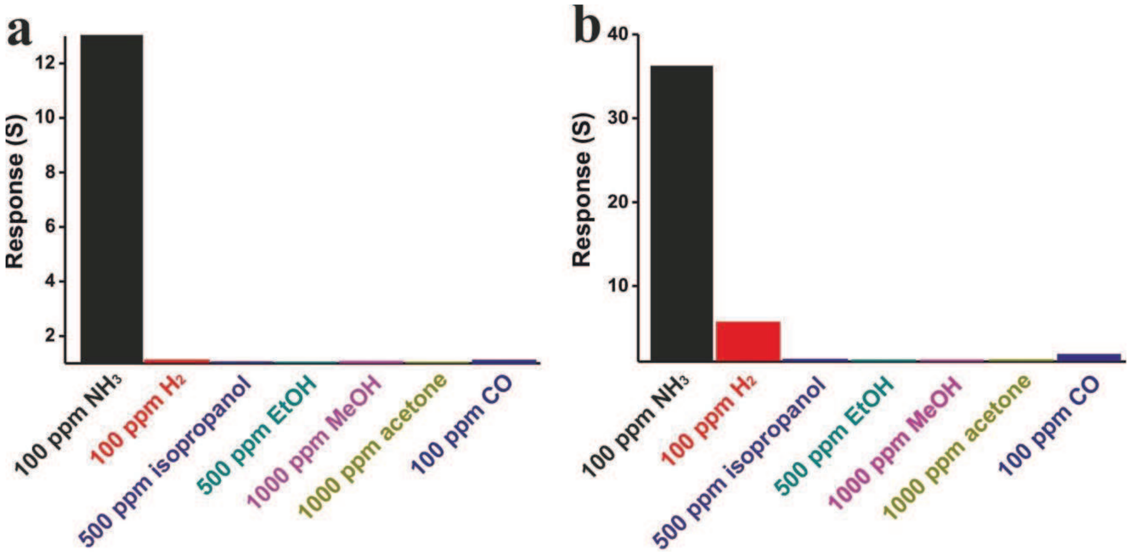

Figure 5.10. Selectivity of (a) sample B (operating temperature 225 °C) and (b) sample C (operating temperature 200 °C) towards 100 ppm NH_3 compared to other reducing gases in high concentrations.

Samples B and C show minute scale response times over the entire NH_3 concentration range (2 ppm NH_3: 3.9 min (B), 4.4 min (C) and 100 ppm NH_3: 1.0 min (B), 1.9 min (C)). As expected, their recovery times increase significantly with the NH_3 concentration from the 5-7 min range (2 ppm) to 40-49 min (100 ppm). Gas response and recovery curves of sample D and E differ considerably from B and C (cf. Figure 5.11). Both sensors made from type D and E materials display extremely high sensitivities towards 100 ppm NH_3 (S(D) = 41.43 and S(E) = 148) at an operating temperature of 200 °C. However, resistance of neither sensor could be recovered after 70 min of sputtering synthetic air into the chamber, and the sensors need more time to recover to their base line signals after exposure to ammonia. Even recovery of samples D and E at elevated temperatures (around 300 °C) did not give a clear baseline, and this temperature range is not acceptable for practical operation because of the drastically reduced sensitivity. A plausible explanation for this behavior is irreversible chemisorption of NH_3 on the surface of sample D and E which will be discussed more detailed in the following section.

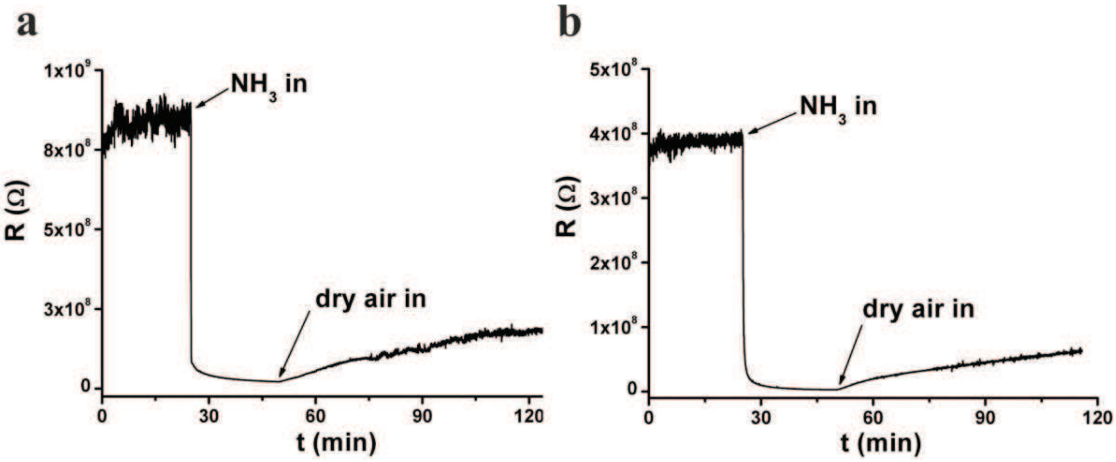

Figure 5.11. Dynamic response curves of (a) sample D and (b) sample E at the optimized operating temperature of 200 °C. Due to high initial sensitivities at low temperatures ($S_D = 41.4$ and $S_E = 148$), sensor recovery is incomplete.

5.3.3 Gas sensing mechanisms

In general, sensing mechanisms of metal oxide resistive chemical sensors involve chemisorbed surface oxide ions where oxygen molecules are absorbed on the oxide sensor surface, thereby giving rise to different species such as O^- , O^{2-} and O_2^- . The reduction/oxidation of these oxide ions thus modulate the carrier concentration in the surface.[63,64] However, previous research revealed that ammonia sensing in α-MoO_3 exhibits different mechanisms where lattice oxygen instead of chemisorbed oxygen dominates the sensing process.[36] Distorted MoO_6 octahedra in the orthorhombic MoO_3 modification easily form shear structures upon removal of oxygen, and in this scenario, ammonia gas would reduce MoO_3 by formation of crystallographic shear planes in the oxide.[65] The resulting products such as Mo_2N exhibit considerably higher electric conductivity than MoO_3. This explanation cannot be applied on h-K-MoO_3 due to its different hexagonal motif. XRD results show that no structural transformation of h-K-MoO_3 after exposure to ammonia gas at working temperature occurs, which indicates no significant transformation into other phases, such as Mo_2N (cf. Figure 5.12).

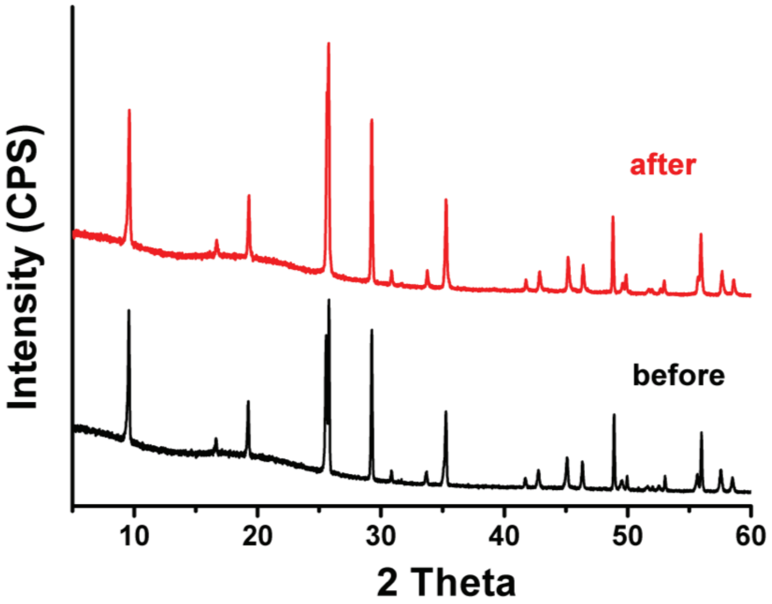

Figure 5.12. PXRD patterns of sample C as ammonia sensor before and after ammonia exposure.

In addition, although the fraction of Mo^{5+} species on the surface is reduced with increasing amount of K^+ additive (cf. Figure 5.5), the corresponding ammonia sensing response is enhanced. This phenomenon is opposite to the observed behavior of α-MoO_3[36] and it indicates that structural transformations have no or only slight effects on the sensing mechanism in our case. On the other hand, the decreasing particle size of the as-synthesized h-K-MoO_3 samples is expected to promote the exposure of surfaces with favorable chemisorption energy for oxygen species. Therefore, we believe that the sensing mechanism in the investigated h-K-MoO_3 compounds can be mainly explained in terms of conventional theory based on chemisorbed surface oxide ions as prevailing factor. Based on studies on other oxide systems, we propose the following hypothesis for the sensing mechanism:[66,67]

$$NH_{3,gas} \rightarrow NH_{3,ads}$$

$$2NH_{3,ads} + 4O^-_{surface} \rightarrow N_2O + 3H_2O + 4e^-$$

$$2NH_{3,ads} + 5O^-_{surface} \rightarrow NO + 3H_2O + 5e^-$$

$NH_{3,gas}$, $NH_{3,ads}$ and $O^-_{surface}$ represent NH_3 in gaseous and chemisorbed form and oxygen ions on the surface, respectively. Electron release on the surface leads to an overall conductance increase as observed in our experiments.

Interestingly, conventional orthorhombic MoO_3 samples have not shown favorable ammonia sensing properties compared with h-K-MoO_3 sensing data of the present study. As summarized in Table 5.4, MoO_3 nanorods, pellets of MoO_3 powder and MoO_3 based thin films exhibited rather poor response towards ammonia gas at operating temperatures of 400 °C and above, and no further information on selectivity was provided.[8,66-69] *Prasad* et al. reported on high sensing selectivity of sputtered MoO_3 films towards low ammonia concentrations, but the issue of their instable resistance values remains to be solved.[39] Sol-gel and ion beam deposited MoO_3 thin films were also identified as ammonia sensors,[68] but the NH_3 detection limit for these materials was 8 ppm, i.e. much higher than the minimum concentration reported in this study. *Hussein* et al. pointed out high sensitivity properties of evaporated MoO_3 thin films towards ammonia gas compared with CO under the same conditions, but no detailed selectivity properties were determined.[69] Furthermore, α- and β-MoO_3 thin films showed poor response toward ammonia in high concentrations,[70] whereas sputtered MoO_3 multilayer thin films exhibited high response to 100 ppm NH_3 and good selectivity to other reducing gases. However, their sensitivity was still lower than that of the h-K-MoO_3 sensors presented here.

It seems that the hexagonal structural motif is favorable over orthorhombic molybdenum oxide for ammonia sensing. In fact, the removal of lattice oxygen in orthorhombic MoO_3 is not surface sensitive compared with chemisorbed oxygen. Moreover, the lattice rearrangement requires high energy which is the reason for much higher working temperatures (300 – 400 °C) than observed for h-MoO_3 (~200 °C) as summed up in Table 5.4. Similar results can also be found in analogous WO_3 compounds with related hexagonal tunnel structures which have been identified as candidates for ammonia sensors.[71]

Table 5.4. Survey of MoO_3-based ammonia sensors.

Sensing material	T (°C)	$S_{100\ ppm\ ammonia}$	Selectivity	Ref.
h-MoO_3	**200**	**39**	**good**	**This work**
α-MoO_3 nanorods	420	6	n/a	[8]
Pellets of α-MoO_3 powders	400	3	poor	[36]
α-MoO_3 based thin film	450	15	n/a	[72]
Sputtered α-MoO_3 films	438	10	good	[39]
α- MoO_3 thin films (sol-gel)	450	4	n/a	[68]
Evaporated α-MoO_3 thin films	400	40	n/a	[69]
α- and β-MoO_3 thin films	250	< 2 (1000 ppm NH_3)	n/a	[70]
Sputtered α-MoO_3 multilayers	300	9	moderate	[10]

Generally, predictive design of gas sensor materials is challenging and the complex interplay of various materials parameters remains difficult to control and to optimize. Electronegativity (EN) has been identified as a crucial chemical criterion for optimizing response and selectivity of sensing materials,[73] and MoO_3 has a higher EN than most of the widely studied sensor oxides, such as SnO_2, TiO_2 or ZnO.[74] This is in line with the excellent response of hexagonal MoO_3 towards NH_3, which has been observed in the course of our study. Hereby, the introduction of K^+ addition has been initially employed to stabilize the structural motif, and its size-controlling effect is furthermore essential to tune the sensor properties. As pointed out above, structural modifications induced by K^+ addition is not likely to influence the sensing mechanism. Therefore, the significant increase of gas response observed for h-K-MoO_3 samples B – E with increasing potassium content is most likely due to grain size effects. Along these lines, the maximum *initial* gas response of h-K-MoO_3 sample E among the series can be explained in terms of its smallest particle size. Among the series, sample A with microscale particle dimensions exhibits lowest gas response although it has by far the highest amounts of reduced Mo^{5+} species on the surface, which has been linked to favorable ammonia sensing properties.[41]

However, numerous other criteria, such as chemical composition, structure, morphology, grain size and surface to volume ratio need to be considered as main factors for gas sensing performance. As widely accepted, the grain size effect often emerges as the most important parameter due to their key role for the transducer function.[75] *Mitsudo* first pointed out the neck effects, in which electrons are mobile between particles through a channel located inside of the space-charge layer.[76] This model indicates that the gas sensing properties depend strongly on the nanoscale particle size.[77] In nanostructured materials, this neck effect can be more influential than the electron transport processes when the particle size is smaller or close to the electron diffusion length.[77] Under such conditions, the entire bulk electron transport can be tuned by surface processes such as gas sensing. In one dimensional structures, the space-charge layer forms on the surface along the axial direction. Therefore, the diameter of nanorod sensors plays a crucial role as mentioned above. In fact, *Fan* et al. reported on distinct oxygen sensing properties of ZnO nanowires vs. bulk materials which underscore this phenomenon.[78] In our case, we can clearly observe an enhanced gas sensing performance with decrease of nanorod diameters (cf. Table 5.1). In particular, for sample D and E, the lower diameter of sample E (65 nm) enhances gas response by a factor around 3 compared to sample D.

In addition to the gas response, decreasing particle diameters and nanowire morphologies also reduced the operating temperature for maximal sensing performance as reported by other research groups.[79-81] All in all, the 1D nanoscaling of our materials does not only provide a large surface area for the adsorption of oxygen species and target gases, but also facilitates their interaction.

Nevertheless, the continuous downsizing of the nanorods below a critical limit negatively affects the sensor stability. The difficulty of recovery from gas response in samples D and E with smallest particle sizes indicates irreversible chemisorptions of surface oxygen. At the moment, it is not entirely clear why the removal of NH_3 from samples D and E is so difficult, because their XRD and XPS data do not point to obvious surface chemistry differences to samples B and C. Particle size optimization obviously requires a compromise between maximum initial response towards NH_3 and reasonable recovery time and temperature afterwards. While low activation energies for chemisorption are favorable for the first sensing response, the activation energy for desorption has to be reasonably low as well to permit full recovery at the operational temperature.[82] Although smaller oxide nanoparticles excel through a higher reactive surface, they may sometimes be easily contaminated.[83] This may be the case for samples D and E, i.e. they seem to fall below a critical particle size that is required for full sensor recovery in combination with low operational temperature/high sensitivity.

5.4 Conclusions

In summary, hexagonal molybdenum oxide (h-K-MoO_3) nanorods in combination with potassium as structural stabilizer and size-tuning agent were successfully synthesized via a convenient hydrothermal procedure. Starting from the dissolution of Mo metal powder in H_2O_2, various molar quantities of KCl were added to the precursor mixture, followed by autoclave treatment at 180 °C for 24 h. Low extent of potassium cation incorporation into the hexagonal channels leads to large diameter of as-synthesized h-K-MoO_3, whereas excess amount of KCl gives rise to decreased rod diameters in the range around 65 nm. Potassium cations play multiple roles as stabilizer with a certain mobility in the hexagonal channel and as size-controlling agent to affect the morphology and particle size. The latter influence of potassium is significantly correlated to the gas sensing behavior of the resulting h-K-MoO_3 sensors.

Detailed ammonia sensing measurements and selectivity tests against a variety of reducing gases (ammonia, hydrogen, methanol, ethanol, acetone, isopropanol and carbon monoxide) demonstrate that h-K-MoO_3 based sensors are preferable for low NH_3 concentration ranges. As-synthesized h-K-MoO_3 nanorods with medium K^+ contents and diameters in the 200 – 350 nm range exhibit promising NH_3 sensing performance with respect to reasonable response/recovery time, outstanding selectivity and low operating temperature. Although h-K-MoO_3 sensors with highest amount of incorporated potassium and smallest particle size display remarkable initial sensitivity towards NH_3, their difficult recovery process render them inefficient for technical applications.

All in all, grain size effects, optimum response/recovery characteristics, good selectivity and reasonable operating temperature are most important criteria for the gas sensing performance. The complex interplay of sensing mechanisms and influence of K^+ cations on the sensing performance will be further investigated.

References

[1] X. Chu, S. Liang, W. Sun, W. Zhang, T. Chen, Q. Zhang, *Sens. Actuators B* **2010**, *148*, 399.

[2] M. B. Rahmani, S. H. Keshmiri, J. Yu, A. Z. Sadek, L. Al-Mashat, A. Moafi, K. Latham, Y. X. Li, W. Wlodarski, K. Kalantar-Zadeh, *Sens. Actuators B* **2010**, *145*, 13.

[3] P. Gouma, K. Kalyanasundaram, X. Yun, M. Stanacevic, L. S. Wang, *IEEE Sens. J.* **2010**, 10, 49-53.

[4] I. Shakir, M. Shahid, D. J. Kang, *Chem. Commun.* **2010**, 46, 4324-4326.

[5] H. Q. Zhang, Y. Wang, E. R. Fachini, C. R. Cabrera, *Electrochem. Solid State Lett.* **1999**, *2*, 437-439.

[6] A. M. Azad, *Sens. Actuators B* **2006**, 120, 25-34.

[7] E. Comini, L. Yubao, Y. Brando, G. Sberveglieri, *Chem. Phys. Lett.* **2005**, 407, 368-371.

[8] A. M. Taurino, A. Forleo, L. Francioso, P. Siciliano, M. Stalder, R. Nesper, *Appl. Phys. Lett.* **2006**, 88, 152111

[9] W. S. Kim, H. C. Kim, S. H. Hong, *J. Nanopart. Res.* **2010**, 12, 1889-1896.

[10] C. Imawan, H. Steffes, F. Solzbacher, E. Obermeier, *Sens. Actuators B* **2001**, 78, 119-125.

[11] C. E. Tracy, D. K. Benson, *J. Vac. Sci. Technol. A* **1986**, *4*, 2377-2383.

[12] V. S. Saji, C. W. Lee, *ChemSusChem* **2012**, 5, 1146-1161.

[13] S. H. Lee, Y. H. Kim, R. Deshpande, P. A. Parilla, E. Whitney, D. T. Gillaspie, K. M. Jones, A. H. Mahan, S. B. Zhang, A. C. Dillon, *Adv. Mater.* **2008**, *20*, 3627-3632.

[14] G. Andersson, A. Magneli, *Acta Chem. Scand.* **1950**, 4, 793-797.

[15] G. A. Nazri, C. Julien, *Solid State Ionics* **1992**, 53, 376-382.

[16] E. M. McCarron, *J. Chem. Soc. Chem. Commun.* **1986**, 336-338.

[17] M. Figlarz, *Prog. Solid State Chem.* **1989**, 19, 1-46.

[18] E. M. McCarron, D. M. Thomas, J. C. Calabrese, *Inorg.Chem.* **1987**, 26, 370-373.

[19] T. P. Feist, P. K. Davies, *Chem. Mater.* **1991**, 3, 1011-1012.

[20] J. Song, X. Ni, L. Gao, H. Zheng, *Mater. Chem. Phys.* **2007**, 102, 245-248.

[21] L. Zheng, Y. Xu, D. Jin, Y. Xie, *Chem. Mater.* **2009**, 21, 5681-5690.

[22] H. J. Lunk, H. Hartl, M. A. Hartl, M. J. G. Fait, I. G. Shenderovich, M. Feist, T. A. Frisk, L. L. Daemen, D. Mauder, R. Eckelt, A. A. Gurinov, *Inorg. Chem*. **2010**, 49, 9400-9408.

[23] T. He, J. N. Yao, *J. Photochem .Photobiol.* **2003**, 4, 125-143.

[24] S. Komaba, N. Kumagai, R. Kumagai, H. Yashiro, *Solid State Ionics* **2002**, 152, 319-326.

[25] S. Balaji, Y. Djaoued, A. S. Albert, R. Z. Ferguson, R. Bruening, *Chem. Mater.* **2009**, 21, 1381-1389.

[26] J. F. Colin, V. Pralong, M. Hervieu, V. Caignaert, B. Raveau, *Chem. Mater.***2008**, 20, 1534-1540.

[27] N. A. Caiger, S. Crouchbaker, P. G. Dickens, G. S. James, *J. Solid State Chem.* **1987**, *67*, 369-373.

[28] N. Sotani, *Bull. Chem. Soc. Jpn.* **1975**, *48*, 1820-1825.

[29] N. Kumagai, K. Tanno, *Electrochim. Acta* **1987**, 32, 1521-1526.

[30] J. D. Guo, P. Zavalij, M. S. Whittingham, *Eur. J. Solid State Inorg. Chem.* **1994**, 31, 833-842.

[31] K. Eda, K. Chin, N. Sotani, M. S. Whittingham, *J. Solid State Chem.* **2005**, 178, 158-165.

[32] K. D. Chen, S. B. Xie, A. T. Bell, E. Iglesia, *J. Catal.* **2000**, 195, 244-252.

[33] G. A. Vorobeva, B. V. Rozentuller, Y. V. Maksimov, M. Y. Kutyrev, L. Y. Margolis, *J. Catal.* **1981**, 71, 405-410.

[34] D. Moszynski, R. Jedrzejewski, J. Ziebro, W. Arabczyk, *Appl. Surf. Sci.* **2010**, 256, 5581-5584.

[35] S. N. Koc, G. Gurdag, E. Loffler, M. Orbay, M. Muhler, M., *Mater. Chem. Phys.* **2004**, 86, 315-319.

[36] S. S. Sunu, E. Prabhu, V. Jayaraman, K. I. Gnanasekar, T. K. Seshagiri, T. Gnanasekaran, *Sens. Actuators B* **2004**, 101, 161-174.

[37] C. Imawan, F. Solzbacher, H. Steffes, E. Obermeier, *Sens. Actuators B* **2000**, 64, 193-197.

[38] O. Merdrignac-Conanec, P. T. Moseley, *Electrochem. Commun.***1999**, 1, 51-54.

[39] A. K. Prasad, P. I. Gouma, D. J. Kubinski, J. H. Visser, R. E. Soltis, P. Schmitz, *Thin Solid Films* **2003**, 436, 46-51.

[40] A. A. Firooz, A. R. Mahjoub, A. A. Khodadadi, *J. Nanosci. Nanotech* .**2010**, 10, 6155-6160.

[41] Y. Zhou, K. B. Zheng, J.-D. Grunwaldt, T. Fox, L. L. Gu, X. L. Mo, G. R. Chen, G. R. Patzke, *J. Phys. Chem. C* **2011**, 115, 1134-1142.

[42] R. B. Watson, U. S. Ozkan, *J. Catal.* **2000**, 191, 12-29.

[43] Z. Zhao, J. Liu, A. Duan, C. Xu, T. Kobayashi, I. E. Wachs, *Topics in Catal.* **2006**, 38, 309-325.

[44] J. Liu, Z. Zhao, C. M. Xu, A. J. Duan, G. Y. Jiang, *J. Phys. Chem. C* **2008**, 112, 5930-5941.

[45] Y. Zhou, N. Pienack, W. Bensch, G. R. Patzke, *Small* **2009**, 5, 1978-1983.

[46] A. Michailovski, R. Kiebach, W. Bensch, J.-D. Grunwaldt, A. Baiker, S. Komarneni, G. R. Patzke, *Chem. Mater.* **2007**, 19, 185-197.

[47] J. Liu, L. Yu, Z. Zhao, Y. Chen, P. Zhu, C. Wang, Y. Luo, C. Xu, A. Duan, G. Jiang, *J. Catal.* **2012**, 285, 134-144.

[48] M. C. Abello, M. F. Gomez, L. E. Cadus, *Catal. Lett.* **1998**, 53, 185-192.

[49] M. M. Arafat, B. Dinan, S. A. Akbar, A. S. M. A. Haseeb, *Sensors* **2012**, 12, 7207-7258.

[50] E. Comini, G. Faglia, G. Sberveglieri, Z. W. Pan, Z. L. Wang, *Appl. Phys. Lett.* **2002**, 81, (10), 1869-1871.

[51] G. Korotcenkov, *Mater. Sci. Eng. R* **2008**, 61, (1-6), 1-39.

[52] B. Krebs, I. Paulat-Boschen, *Acta Cryst.* **1976**, B32, 1697–1704.

[53] A. L. Chen, D. Xu, X. Y. Chen, W. Y. Zhang, X. H. Liu, *Trans. Nonferrous Met. Soc. China* **2012**, 22, 1513-1516.

[54] A. Michailovski, F. Krumeich, G. R. Patzke, *Helv. Chim. Acta* **2004**, *87*, 1029.

[55] G. R. Patzke, Y. Zhou, R. Kontic, F. Conrad, *Angew. Chem. Int. Ed.* 2011, **50**, 826-859.

[56] G. R. Patzke, A. Michailovski, F. Krumeich, R. Nesper, J.-D. Grunwaldt, A. Baiker, *Chem. Mater.* **2004**, 16, 1126-1134.

[57] A. Michailovski, G. R. Patzke, *Z. Anorg.Allg. Chem.* **2007**, 633, 54-62.

[58] A. Michailovski, J. B. Willems, N. Stock, G. R. Patzke, *Helv. Chim. Acta* **2005**, 88, 2479-2501.

[59] X. Deng, S. Y. Quek, M. M. Biener, J. Biener, D. H. Kang, R. Schalek, E. Kaxiras, C. M. Friend, *Surf. Sci.* **2008**, 602, 1166-1174.

[60] T. S. Sian, G. B. Reddy, *Sol. Energ. Mat. Sol. C.* **2004**, 82, (3), 375-386.

[61] L. Zhou, J. Zhu, M. Yu, X. Huang, Z. Li, Y. Wang, C. Yu, *J. Phys. Chem. C* **2010**, 114, 20947-20954.

[62] L. Liao, H. B. Lu, J. C. Li, H. He, D. F. Wang, D. J. Fu, C. Liu, W. F. Zhang, *J. Phys. Chem. C* **2007**, 111, 1900-1903.

[63] S. Bai, K. Zhang, R. Luo, D. Li, A. Chen, C. C. Liu, *J. Mater. Chem.* **2012**, 22, 12643-12650.

[64] E. Comini, *Anal. Chim. Acta* **2006**, 568, 28-40.

[65] L. Volpe, M. Boudart, *J. Solid State Chem.* **1985**, 59, (3), 332-347.

[66] Y. Shimizu, T. Okamoto, Y. Takao, M. Egashira, *J. Mol. Catal. A Chem.* **2000**, 155, 183-191.

[67] I. Jimenez, A. M. Vila, A. C. Calveras, J. R. Morante, *IEEE Sens. J.* **2005**, 5, 385-391.

[68] A. K. Prasad, D. J. Kubinski, P. I. Gouma, *Sens. Actuators B* **2003**, 93, (1-3), 25- 30.

[69] O. M. Hussain, K. S. Rao, *Mater. Chem. Phys.* **2003**, 80, (3), 638-646.

[70] W. C. Chang, X. Qi, J. C. Kuo, S. C. Lee, S. K. Ng, D. Chen, *CrystEngComm.* **2011**, 13, (16), 5125-5132.

[71] L. Wang, J. Pfeifer, C. Balazsi, P. I. Gouma, *Mater. Manuf. Processes* **2007,** 22, (5-6), 773-776.

[72] A. K. Prasad, P. I. Gouma, *J. Mater. Sci.* **2003**, 38, (21), 4347-4352.

[73] K. I. Shimizu, I. Chinzei, H. Nishiyama, S. Kakimoto, S. Sugaya, W.Matsutani, A. Satsuma, *Sens. Actuators B*, **2009**, 141, 410-416.

[74] J. Portier, P. Poizot, J. M. Tarascon, G. Campet, M. A. Subramanian, *Solid State Sci.* **2003**, 5, 695-699.

[75] N. Yamazoe, *Sens. Actuators B* **1991**, 5, (1-4), 7-19.

[76] Mitsudo H., *Ceramics*, **1980**, 15, 339-345.

[77] G. Korotcenkov, S. D. Han, B. K. Cho, V. Brinzari, *Crit. Rev. Solid State Mater. Sci.* **2009,** 34, 1-17.

[78] Z. Y. Fan, D. W. Wang, P. C. Chang, W. Y. Tseng, J. G. Lu, *Appl. Phys. Lett.* **2004**, 85, (24), 5923-5925.

[79] N. M. Shaalan, T. Yamazaki, T. Kikuta, *Sens. Actuators B* **2011**, 153, 11-16.
[80] G. Korotcenkov, V. Brinzari, J. Schwank, A. Cerneavschi, *Mater. Sci. Eng. C* **2002**, 19, 73-77.
[81] R. Botter, T. Aste, D. Beruto, *Sens. Actuators B* **1994**, 22, 27-35.
[82] G. Korotcenkov, *Mater. Sci. Eng. B*. **2007**, 139, 1-23.
[83] H. Wang, F. Shadman, *AlChE J.* **2012**, DOI: 10.1002/aic.13936.

Summary

The promising applications of nanostructured semiconducting transition metal oxides, for example as gas or humidity sensors, offer the possibility to solve global environmental problems. Therefore, further development of synthetic strategies and design of advanced functional target oxide materials are required to accomplish this ambitious goal. In particular, the sensing performance of target compounds, which is strongly correlated to their preparative history, morphology, chemical composition and surface properties, needs to be understood and improved in an informed way for industrial and daily life applications.

In the present thesis, an overview of application-oriented bismuth- and molybdenum-based materials with respect to synthetic routes, structure motifs, morphology and particle size is provided in combination with application-oriented investigations of their gas and humidity sensing properties. The results demonstrate their promising potential as gas/humidity sensors and open up a wide scope for further developments, e.g. by tuning the chemical compositions, constructing heterostructures or incorporation of additives.

$Bi_2O_2CO_3$ nanosheets with a layered structure motif were obtained at room temperature via a novel and facile approach using atmospheric CO_2 as carbon source (Chapter 2). This energy- and cost-saving synthetic route opens up an environmentally friendly pathway for the preparation of functional nanostructured materials. Moreover, various humidity sensing characteristics such as hysteresis features, time-dependent impedance and capacitance measurements over a broad range of humidity values (11 – 95 % RH) as well as reproducibility over several cycles are discussed. This study first points out the promising humidity sensing application potential of $Bi_2O_2CO_3$ nanosheets.

Microstructured sillenite- and monazite-types of bismuth phosphate were selectively synthesized under hydrothermal reaction conditions (Chapter 3). The pH- and time-dependent crystallization processes and the resulting morphological properties of bismuth-containing materials were intensively studied. Optimization of synthetic parameters, chemical structure, morphology, thermal stability, hydrophilicity and humidity sensing characteristics of the final products are discussed in detail. Cubic bismuth phosphate with a sillenite-type Bi/O-tunnel structure was characterized as a promising humidity sensor over a wide range of humidity values (11 – 95% RH) with respect to good reproducibility and long-term sensing stability.

Synthesis of anisotropic α-MoO_3/SnO_2 heterostructures was achieved through convenient hydrothermal treatments (Chapter 4). The combination of α-MoO_3 belts and SnO_2 quantum dots opens up a new strategy for enhancing the gas sensing response and reducing the optimal operating temperature. The low work function of SnO_2 and the formation of a depletion layer between both oxides facilitate the generation of surface oxygen species, which leads to an improvement of hydrogen sensing performance.

Furthermore, structurally tuneable hexagonal MoO_3 nanorods stabilized with K^+ cations in their channels (h-K-MoO_3) were hydrothermally synthesized using molybdenum oxide and KCl as easily accessible commercial precursors (Chapter 5). In this study, the multiple role of KCl as structural stabilizer and size-controlling agent was used for tuning the particle size and the resulting gas sensing characteristics, respectively. Starting from the investigation of surface properties of h-K-MoO_3 nanorods, such as morphology, surface-area-to-volume ratio, and surface oxidation states (via X-ray photoelectron spectroscopy), these properties were correlated with the resulting ammonia sensing performance/selectivity. Detailed gas sensing experiments demonstrated that h-K-MoO_3 nanorods with particle sizes between 200 – 350 nm exhibit the most suitable ammonia sensing characters with respect to good response/recovery behavior and high selectivity. Optimization of the particle size, which can be tuned by varying amounts of ionic additives, is essential to adjust response/recovery time and operating temperature of the h-K-MoO_3 nanorod sensors.

In summary, the present thesis starts from the facile syntheses of nanostructured materials and studies their physical/chemical surface properties with a variety of analytical methods. The obtained bismuth-based materials and molybdenum-containing oxides were identified as promising humidity and hydrogen/ammonia sensing materials, which can be applied to solve future environmental issues.

Zusammenfassung

Die vielversprechenden Anwendungsmöglichkeiten nanostrukturierter halbleitender Übergangsmetalloxide, z. B. als Gassensoren oder Feuchtigkeitssensoren, bieten neue Möglichkeiten zur Lösung globaler Umweltprobleme. Dies erfordert die weitere Entwicklung der synthetischen Strategien für hoch entwickelte funktionelle Oxide, um dieses anspruchsvolle Ziel zu erreichen. Insbesondere soll das Sensorverhalten der Zielverbindungen, welches stark mit präparativem Werdegang, Morphologie, chemischen Zusammensetzungen und Oberflächeneigenschaften verknüpft ist, verstanden und für die Applikationen in Industrie und Alltagsleben gezielt verbessert werden.

In der vorliegenden Arbeit werden anwendungsrelevante Bismut- und Molybdän-basierte Materialien in Bezug auf Synthesestrategie, strukturelle Motive, Morphologie und Partikelgrösse untersucht und die daraus resultierenden anwendungsorientierten Gas- und Feuchtigkeitssensoreigenschaften untersucht. Die Resultate zeigen ihr vielversprechendes Potential als Gas-/Feuchtigkeitssensoren auf und eröffnen einen grossen Spielraum für zielgerichtete Weiterentwicklung, z. B. durch Anpassung der chemischen Zusammensetzungen, Herstellung entsprechender Heterostrukturen oder Steuerung von Partikelgrösse und Morphologie durch Additive.

$Bi_2O_2CO_3$ Nanoplättchen mit einem schichtartigen Strukturmotiv wurden bei Raumtemperatur durch eine neuartige und einfache Methode unter Atmosphärendruck mit CO_2 als Kohlenstoffquelle synthetisiert (Kapitel 2). Diese ökonomische und unkomplizierte Syntheseroute eröffnet einen umweltfreundlichen Weg für die Präparation hoch entwickelter funktioneller Materialien. Darüber hinaus wurden verschiedene Eigenschaften der Feuchtigkeitssensoren, z. B. Hysterese-Funktion, zeitabhängige Impedanz- und Kapazitätsmessungen in einem breiten Feuchtigkeitsbereich (11 – 95% RH), sowie die Reproduzierbarkeit über mehrere Zyklen, diskutiert. Diese Untersuchung weist als erste Studie auf das vielversprechende Applikationspotential der $Bi_2O_2CO_3$ Nanoplättchen als Feuchtigkeitssensoren hin. Mikrostrukturelle Bismutphosphate vom Sillenit- und Mozanit-Typ wurden selektiv unter hydrothermalen Reaktionsbedingungen synthetisiert (Kapitel 3). Die pH- und zeitabhängigen Kristallbildungsprozesse und die resultierenden morphologischen Eigenschaften dieser bismuthaltigen Materialien wurden intensiv untersucht.

Optimierung der Reaktionsparameter, chemische Strukturen, Morphologie, thermische Stabilität, Hydrophilie und Feuchtigkeitssensoreigenschaften der Endprodukte wurden im Detail diskutiert. Kubisches Bismutphosphat (Sillenit-Typ) mit einer Bi/O-Tunnelstruktur wurde als ein vielversprechender Feuchtigkeitssensor für einen breiten Feuchtigkeitsbereich (11 – 95% RH) mit guter Reproduzierbarkeit und langfristiger Sensorstabilität charakterisiert.

Die Synthese anisotroper α-MoO_3/SnO_2 Heterostrukturen wurde mit flexiblen Hydrothermalverfahren ausgeführt (Kapitel 4). Durch die Kombination von α-MoO_3 Fasern und SnO_2 quantum dots (QDs) wurde eine neue Strategie entwickelt, um gassensorische Reaktionsprozesse zu optimieren und die optimale Betriebstemperatur zu reduzieren. Die niedrige Elektronenaustrittsarbeit von SnO_2 und die Bildung der Raumladungszone zwischen den beiden Oxiden erleichtern die Erzeugung von Oberflächensauerstoffspezies, welche zu einer verbesserten Wasserstoffdetektion führt.

Des Weiteren wurden hexagonale MoO_3 Nanostäbchen hydrothermal synthetisiert und durch Kalium-Kationen in den Kanälen der hexagonalen Molybdänoxidstruktur stabilisiert (h-K-MoO_3), wobei Molybdänoxid und KCl als einfach zugängliche kommerzielle Ausgangsstoffe benutzt wurden (Kapitel 5). In dieser Studie wurde die vielfältige Rolle von KCl als Additiv zur Stabilisierung der Struktur und zur Kontrolle der Teilchengrösse angewendet, um die resultierenden Gassensoreigenschaften zu optimieren. Zunächst wurden die Oberflächeneigenschaften von h-K-MoO_3 Nanostäbchen, sowie Morphologie, Oberfläche-Volumen-Verhältnis und Oberflächenoxidationsstufen (durch Röntgenphotoelektronenspektroskopie) untersucht. Diese Eigenschaften waren mit der resultierenden Ammoniak-Sensorik und Selektivität deutlich korreliert. Detaillierte Messungen der Gassensoreigenschaften zeigten auf, dass die h-K-MoO_3 Nanostäbchen mit Partikelgrössen zwischen 200 – 350 nm aufgrund ihrer guten Reaktions-/Erholungsprozesse und hohen Selektivität die besten Sensoreigenschaften haben. Der Optimierungsprozess der Partikelgrösse, welche durch die Menge der zugegebenen ionischen Additive bestimmbar ist, ist notwendig für die Anpassung der Reaktions-/Erholungszeit und der Betriebstemperatur von h-K-MoO_3 Nanostäbchen als Ammoniak-Sensoren.

Zusammenfassend wird in der vorliegenden Arbeit von einfachen Synthesen nanostrukturierter Materialien und Untersuchungen ihrer physikalischen/chemischen

Oberflächeneigenschaften mit einer Vielzahl von analytischen Methoden ausgegangen. Die hergestellten bismut- und molybdänhaltigen Materialien wurden als vielversprechende Feuchtigkeits- und Wasserstoff/Ammoniak Sensoren identifiziert, welche zu kostengünstigen Lösungen für zukünftige Umweltprobleme sowie für Industrie und Haushalt entwickelt werden können.

Curriculum Vitae

Min Sheng (aka Min Müller)

PERSONAL INFORMATION

Female, born on 9th Aug. 1981 in Shanghai, Chinese citizenship, married

CONTACT DATA

Institute of Inorganic Chemistry
University of Zurich, Switzerland
Phone: +41 (0)44 635 46 97
e-mail: min.sheng@aci.uzh.ch

EDUCATION

Oct. 2009 – present

Institute of Inorganic Chemistry, University of Zurich, Zurich Switzerland

- PhD candidate and project member of the Swiss national research project MaNEP (Materials with Novel Electric Properties) under supervision of Prof. Dr. Greta Patzke
- Topic: Functional Bismuth- and Molybdenum-based Nanomaterials and their Humidity and Gas Sensing Properties

Oct. 2007 – Jun. 2008

Chemical Oceanography, IFM-Geomar Institute, Kiel Germany

- Diploma thesis under supervision of Prof. Dr. Arne Körtzinger and Prof. Dr. Douglas W. R. Wallace
- Topic: Field testing of a new UV-spectrophotometric nitrate sensor in the Kiel Fjord

Oct. 2002 – Sep. 2007

Diploma in Chemistry at University of Kiel, Kiel Germany

- Main focus: Inorganic chemistry / Physical chemistry / Marine chemistry

Sep. 2001 – Jul. 2002

German as foreign language at Language Center, University of Kiel, Kiel Germany

Sep. 1996 – Jun. 1999

Matura at Peijin Highschool, Shanghai China

PRESENTATIONS

- *SPS-MaNEP Meeting*, Zurich Switzerland, **21st Jun. 2012**
  Humidity Sensing Properties of Different Bismuth Phosphate Types (poster presentation)
- *Solid State Chemistry Conference*, Lanzarote Spain, **24th – 27th Feb. 2012**
  Humidity Sensing Properties of Bismuth-Phosphate Modifications (oral presentation)
- *SCS Fall Meeting*, Zurich Switzerland, **9th Sep. 2011**
  Development of Novel Sensors Based on Mo- and Bi-Materials (poster presentation)
- *Eurosensors*, 24th, Linz Austria, **5th – 8th Sep. 2010**
  Development of Novel Sensors Based on Oxide Nanowires (poster presentation)

WORKSHOPS

- Paul Scherrer Institute, Villigen Switzerland, **24th – 30th May 2010**
  Powder Diffraction Summer School 2010

ACADEMIC HONORS AND AWARDS

- *Sino Swiss Science and Technology Cooperation Program*, **Sep. 2010 – Aug. 2011**
  Student Exchange Grand (Project No.:EG16-032010) with Fudan University in Shanghai, China

SKILLS AND QUALIFICATIONS

Laboratory Techniques	Clean room technology (Lift-off microtechnology), Deposition techniques, AFM, Surface Step Profiler, Wafer Bonder, Hydrothermal synthesis, XRD, SEM, EDX, IR, UV-Vis, BET, DTA-TG
Computer Skills	Windows, Mac OS, Microsoft-Office, Origin, Corel Draw, SPSS
Language Skills	Chinese (native), English (very good), German (very good)